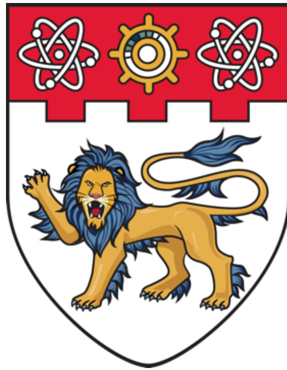

NANYANG TECHNOLOGICAL UNIVERSITY
SINGAPORE

SPIN-ORBIT TORQUE: SPIN ACCUMULATION TECHNIQUES AND INTERFACIAL INVESTIGATION OF TOPOLOGICAL INSULATOR

POH HAN YIN

SCHOOL OF PHYSICAL AND MATHEMATICAL SCIENCES

2023

SPIN-ORBIT TORQUE: SPIN ACCUMULATION TECHNIQUES AND INTERFACIAL INVESTIGATION OF TOPOLOGICAL INSULATOR

POH HAN YIN

SCHOOL OF PHYSICAL AND MATHEMATICAL SCIENCES

A thesis submitted to the Nanyang Technological University in partial fulfilment of the requirement for the degree of Doctor of Philosophy

2023

Statement of Originality

I hereby certify that the work embodied in this thesis is the result of original research done by me except where otherwise stated in this thesis. The thesis work has not been submitted for a degree or professional qualification to any other university or institution. I declare that this thesis is written by myself and is free of plagiarism and of sufficient grammatical clarity to be examined. I confirm that the investigations were conducted in accord with the ethics policies and integrity standards of Nanyang Technological University and that the research data are presented honestly and without prejudice.

NTU NTU NTU NTU NTU NTU NTU NTU

31 JULY 2023

. . . .
Date

. . . .
Poh Han Yin

Supervisor Declaration Statement

I have reviewed the content and presentation style of this thesis and declare it of sufficient grammatical clarity to be examined. To the best of my knowledge, the thesis is free of plagiarism and the research and writing are those of the candidate's except as acknowledged in the Author Attribution Statement. I confirm that the investigations were conducted in accord with the ethics policies and integrity standards of Nanyang Technological University and that the research data are presented honestly and without prejudice.

31 JULY 2023

. . . .
Date

. . . .
Lew Wen Siang

Authorship Attribution Statement:

This thesis contains material from 3 paper(s) published in the following peer-reviewed journals in which I am listed as an author.

Chapter 3 is published as H.Y. Poh, C.C. Ang, T.L. Jin F. Tan, G. Lim, and W.S Lew. Continuous film characterisation of Spin Orbit Torque using Four Probe Measurement. *Applied Physics Letters*, **121**, 012405 (2022); DOI.org/10.1063/5.0092471

The contributions of the co-authors are as follows:

- I designed the experiment and prepared the manuscript draft.
- Dr. Weiliang Gan provided the initial direction for this work.
- I designed the experimental setup with the assistance of Dr. Gerard Lim.
- I performed the sample fabrication, electrical measurement, collection and analyzing the data.
- Dr. Tianli Jin assisted in the sample fabrication.
- The manuscript was revised by Dr. Calvin Ang and Dr. Gerard Lim, Dr. Funan Tan and Dr. Tianli Jin.
- Prof Lew Wen Siang supervised in the study.
- All authors contribute to the discussion and preparation of the manuscript.

Chapter 4 is published as H.Y. Poh, C. C. I. Ang, W. L. Gan, G. J. Lim, and W. S Lew. Direct spin accumulation quantification in ferromagnetic heterostructures using DC bias harmonic Hall measurement. *Physical Review B*, **104**, 224416 (2021). DOI.org/10.1103/PhysRevB.00.004400

The contributions of the co-authors are as follows:

- I co-designed the study with Dr. Weiliang Gan.
- I performed the sample fabrication, electrical measurement, and collection of data.
- Dr. Weiliang Gan and I analyzed the DC-bias harmonic results.
- The manuscript was revised by Dr. Calvin Ang and Dr. Gerard Lim.
- Prof Lew Wen Siang supervised in the study.

- All authors contribute to the discussion and preparation of the manuscript.

Chapter 5 is published as H.Y. Poh, C. C. I. Ang, G. J. Lim, T. L. Jin, S. H. Lee, E. K. Koh, F. Poh, and W. S. Lew, Crystallinity control of topological insulator BiSb(012) via interfacial engineering for spin orbit torque enhancement. *Physical Review Applied*, **19**, 034012 (2023); DOI: 10.1103/PhysRevApplied.19.034012

The contributions of the co-authors are as follows:

- I designed the experiment and prepared the manuscript draft.
- I performed the sample fabrication, electrical measurement, and collection and analyzing of data.
- Mr. Eng Kang Koh assisted in the analyzing the crystal structure from the XRD results.
- Dr. Calvin Ang assisted in analyzing the HR-TEM results.
- The manuscript was revised by Dr. Calvin Ang, Mr. Eng Kang Koh, Dr. Gerard Lim, Dr. Tianli Jin.
- Prof Lew Wen Siang supervised in the study.
- All authors contribute to the discussion and preparation of the manuscript.

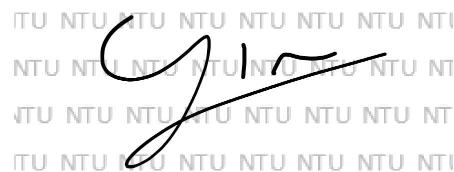

31 JULY 2023

. . . .
Date

. . . .
POH HAN YIN

ABSTRACT

Spin-orbit torque (SOT) represents a promising direction in the field of spintronics, allowing the manipulation of magnetization *via* electric current. Originating from strong spin-orbit coupling in materials such as heavy metals or topological insulators, it allows the generation of large SOT. However, a comprehensive understanding of the SOT mechanism such as spin accumulation dynamics in these materials remains elusive. Spin accumulation has been a subject of continued pursuit to understand SOT switching mechanisms for spintronics device applications. Effective methods to precisely characterize spin accumulation in a ferromagnet are yet to be demonstrated.

Enhancement in SOT efficiency is highly desired as it allows low-power magnetization switching. As such, recent SOT studies focus on exploring novel materials and structures to improve efficiency. The topological insulator has recently drawn much attention as it demonstrates high charge-spin conversion efficiency due to its spin-momentum locking at the Dirac surface states. However, integrating the topological insulator into a magnetic heterostructure remains a challenge as the topological surface state is highly sensitive to perturbations.

In this thesis, a technique to quantify spin accumulations directly in a heavy metal/ferromagnet heterostructure *via* DC-biased harmonic Hall measurement was presented. This technique relies on the induced anomalous resistance, which is generated by the spin Hall effect, and alters its sign based on the alignment of accumulated spins to local magnetization. Spin transport in topological insulators, particularly $Bi_{0.85}Sb_{0.15}$, was explored to enhance the SOT efficiency. Here, I investigate the use of different insertion layers between the TI and FM, to promote the crystallinity of the TI. The improvement of crystallinity will affect the topological surface state (TSS), which results in the enhancement of spin-orbit torque. Lastly, the influence of magnetic moment on SOT generated by the TSS from TI in a TI/FM heterostructure was studied. The experimental and analytical results reveal that the out-of-plane magnet moments disrupts the TSS of the TI, which induces a bandgap. The increment in magnetic moment induces a larger bandgap, which decreases SOT generated from the TI.

ACKNOWLEDGEMENTS

I would like to express my deepest gratitude and appreciation to all those who provided me the support and encouragement throughout this four-year long PhD journey. Firstly, I would like to thank my supervisor, Prof Lew Wen Siang, for supervising me and providing numerous advice on career development. I would also like to show my appreciation to him for recognizing my ability and granting me many opportunities to attend international conference.

Next, I would like to thanks to my mentor, Dr. Gan Weiliang, for teaching and shaping me during the first two years of my PhD. His wisdom, kindness, and mentorship extended beyond the confines of the laboratory and played a critical role in my personal growth and development during the course of this PhD program.

Dr. Calvin Ang and Dr. Gerard Lim have provided me many insightful comments and always a go-to people for any technical assistance. Their insightful guidance in scientific writing has significantly improved the quality of my work and has taught me the art of conveying complex ideas succinctly and effectively. Despite their busy schedule, they always found time to provide help when I needed it most. Without their invaluable help and support, this journey would not have been the same.

I would also like to thank my peers, Eng Kang, Calvin, Jia Rui and Funan. Despite having different area of expertise, they dedicate time and effort to provide me with constructive comments. They also have been sources of both hilarious distractions and steadfast support. Our shared moments of fun, the occasional bouts of nonsense, and all the laughter we have shared, have made PhD journey much more bearable.

I would like to thank all my collaborators, Prof Chang Guo Qing, Prof Ang Yee Sin, Prof Ricky Ang, Dr. Hou Tao and Wei Jie Chan at NTU and SUTD. I would like to thank you for making my research experience fulfilling.

I am grateful for the unwavering support and collective wisdom of my entire research group. There are my postdocs, Dr. Tianli Jin, Dr. Gerard Lim, Dr. Putu Andhita Danajaya, Dr Funan Tan, Dr. Calvin Ang. My juniors, Calvin Lee, Lee Shu Hui, Koh Eng Kang, Hou Kunqi, Chee Mun Yin, Liu Lingli, Wu Shuo, Wong Yun Ming, Ang Jia Min, Thong Jia Rui, Cheng Kangjian, and Bryan Cheng. Also the visiting students, Li Shaomin, Shen Kaimin, Zhou Panke. Nevertheless, those who have contributed to this journey but have since embarked on other professional ventures.

This journey has been challenging and I want to express my heartfelt gratitude to my family for their unwavering support. My parents with their unconditional love and support have been a constant source of strength for me.

Thank you, Xinyan, for all your love.

.

Table of Contents

Abstract **7**

Acknowledgement **8**

Chapter 1 Introduction **17**

1.1 Background **17**

1.2 Advancement in Spintronics **19**

1.3 Motivation **22**

1.4 Thesis Outline **24**

Reference **26**

Chapter 2 Background in Spin Transport and Topological Insulator **31**

2.1 Spintronics: Spin-Orbit Coupling to Spin-Orbit Torque **31**

2.1.1 Spin-Orbit Coupling 31

2.1.2 Spin Hall Effect 33

2.1.3 Rashba-Edelstein Effect 36

2.1.4 Magnetization Dynamics 38

2.2 Topological Insulator in Spintronics **40**

2.2.1 Quantum Hall Effect 40

2.2.2 Quantum Spin Hall Effect 43

2.2.3 Quantum Anomalous Hall effect 44

2.2.4 3D Topological Insulator 45

2.2.5 Spin-Orbit Torque in Topological Insulator 47

2.2.6 Advancement in Topological Insulator for Spintronics 48

References **50**

Chapter 3 Experimental Techniques **58**

3.1 Device Fabrication **58**

3.1.2 Magnetron Sputtering Deposition 59

3.1.3 Electron Beam Lithography 61

3.1.4 Ion Beam Etching 63

3.2 Device Characterization Technique 64

3.2.1 Vibrating Sample Magnetometer 64

3.2.2 X-Ray Diffraction 66

3.3 Harmonic Hall Technique..67

3.3.1 Harmonics Hall Technique Setup 67

3.3.2 Derivation of Harmonic Hall Voltage 68

3.4 Four Probe Technique for Spin-Orbit Torque Characterization....................................73

3.4.1 Experimental Details 73

3.4.2 Modeling for Current Distribution 74

3.4.3 Spin-Orbit Torque Characterization using Four Probe Technique....................77

References 82

Chapter 4 Direct Spin Accumulation Quantification in Ferromagnetic Heterostructures using DC bias Harmonic Hall Measurement..87

4.1 Introduction 87

4.2 Experimental Model 88

4.3 Experimental Details 91

4.4 Characterization of Spin-Orbit Torque Field in Ta/Co/Pt and Ti/Co/Pt 92

4.5 Quantification of Spin Accumulation..93

4.6 Conclusion 96

References 98

Chapter 5 Crystallinity Control of Topological Insulator BiSb(012) *via* Interfacial Engineering for Spin-Orbit Torque Enhancement..101

5.1 Introduction 101

5.2 Experimental Details 103

5.3 Parasitic Thermal Measurement 105

5.4 Results and Discussion..107

5.5 Conclusion **112**

Reference **113**

Chapter 6 Influence of Magnetic Moments on the Topological Surface State in Topological Insulator/Ferromagnet Interface **118**

6.1 Introduction **118**

6.2 Theoretical Modelling **119**

6.3 Experimental Details **122**

6.4 Quantification of spin-orbit torque under varying out-of-plane magnet moment . **123**

6.5 Conclusion **126**

Reference **127**

Chapter 7 Conclusion and Future Work **130**

7.1 Summary of thesis **130**

7.2 Future Work **131**

7.2.1 Fermi Level Tuning in Topological Insulator with Voltage Control Magnetic Anisotropy Heterostructure 131

7.2.2 Magnetic Topological Insulator 132

Reference **134**

List of Publication **135**

List of Conference **137**

List of Figures

Fig. 1.1: Memory Hierarchy structure depicting different type of memory tiers 6

Fig. 1.2: Schematic of giant magnetoresistance (GMR) concept. (Left) Low resistance state when parallel (Right) High resistance state when anti-parallel. 7

Fig. 1.3: Schematic of spin-transfer torque (STT) mechanism..8

Fig. 1.4: Schematic of SOT-MRAM structure...9

Fig. 2.1: Schematic of spin Hall effect (SHE), where the current is injected into the heavy metal (HM) layer, and due to strong spin-orbit coupling (SOC), the electrons are scattered depending on their spins orientation. 20

Fig. 2.2: Schematic of extrinsic scattering (Left) Skew scattering (Right) Side-jump scattering 22

Fig. 2.3: Energy dispersion of 2DEG, $E \propto k^2$ (a) with space-inversion symmetry, and (b) broken space-inversion symmetry. Figure is adapted from [32]. 24

Fig. 2.4: Fermi surface of the (a) Fermi surface of split band at equilibrium (b) Fermi surface of split band under applied electric field along x-direction 25

Fig. 2.5: Illustration of magnetization dynamics govern by the Landau-Lifshitz Gilbert (LLG) equations. The black arrow, M, is the magnetization of ferromagnet, the blue arrow represents the effective field, H_{eff}. The red and green arrow represents damping-like torque and field-like torque, respectively, where they are mutually orthogonal to each other...26

Fig. 2.6 Typical quantum Hall effect results, measured at 30mK in InGaAs-based heterostructure, adopted from [38]. 28

Fig. 2.7: Schematic of chiral conductive edge..30

Fig. 2.8: Schematic of quantum spin Hall effect (QSHE) 30

Fig. 2.9: Observation of Quantum Anomalous Hall effect at 30mK in Cr-doped $(Bi\text{-}Sb)_2Te_3$ thin films. (Left) ρ_{xy} with varying magnetic field at different gate voltage. (Right) ρ_{xx} with varying magnetic field at different gate voltage. 32

Fig. 2.10: ARPES measurements of surface electronics band dispersion on Bi_2Se_3(111) around the Γ- point. Adapted from [48]. 33

Fig. 2.11: (Left) Surface state dispersion (Middle) Weak TI where the Fermi contour enclosing even Γ points (Right) Strong TI where the Fermi contour enclose an odd number of Γ points 33

Fig. 3.1: (Top) Image of two customized-made AJA ATC-Orion 9 UHV sputtering system (Bottom) Two x 8 different targets in the main chamber 46
Fig. 3.2: Image of a Electron Beam Lithograph Setup (Raith eLine EBL) 47
Fig. 3.3: SEM image of a 1 μm device...48
Fig. 3.4: Image of a ion-bean etching setup...49
Fig. 3.5: (Left) Image of VSM (Right) Illustration of the VSM setup 50
Fig. 3.6: Illustration of X-ray beam reflecting off the sample 51
Fig. 3.7: (Top) Image of Harmonic Hall measurement setup Setup (Bottom) Zoom-in view between the pole gap and the wire-bonded device on a customized chip carrier 53
Fig. 3.8: Schematic setup for four-probe harmonic Hall measurement where the current probe distance and voltage probe distance are 4 mm and 8 mm, respectively. 59
Fig. 3.9: Current distribution due to shunting effects across the different voltage probe distances, d = 2, 4, 6, and 8 mm at a current probe distance of 8 mm..60
Fig. 3.10: (a) Current distribution in a 20 µm by 5 µm Hall cross device. (b) Current distribution in a continuous thin film at a current probe distance of 8 mm. (c) Current distribution profile of Hall cross device and continuous film. 62
Fig. 3.11: (a) First harmonic voltage, V_{ω} and (b) second harmonic voltage, $V_{2\omega}$ in a four-probe harmonic measurement across different ranges of current densities, Jc for Pt/Co/Ti continuous film. (c) and (d) Four-probe results for damping-like field, HDL as a function of Jc for Pt(5)/Co(1.4)/ Ti(2) and Ti(2)/Pt(5)/Co(1.4)/Ta(5), respectively. (e) and (f) Damping-like field, HDL as a function of Jc for Pt(5)/Co(1.4)/Ti(2) and Ti(2)/Pt(5)/Co(1.4)/Ta(5) for Hall cross devices. 64
Fig. 3.12: Ratio between anomalous Hall resistance, R_{AHE} (Hall cross device and continuous film) and R_{sat}, where R_{sat} is the magnitude of anomalous Hall resistance of Hall device. (b) Comparison between Hall cross-device and continuous film for current density profile (1st row), m and Δm profile (2nd row), and AHE / SOT profile (3rd row). 65
Fig. 4.1: (a) Schematic of DC bias harmonic Hall setup in the longitudinal configuration. (b) Schematic of the spin accumulation in the FM/HM structure with in-plane anisotropy. Spins are accumulated in the $+y$ direction in the FM layer when the injected electron is in the $+x$ direction. Local magnetization, m follows the direction of the external field, Hy. The amplitude of first Harmonics resistance, R_{ω} increases (decreases) when spin accumulations, s, are parallel (antiparallel) to the local magnetization of the FM layer as described in (4.2). 72

Fig. 4.2: Vibrating sample magnetometer results for Ta(2)/Co(2)/Pt(5) structure. The black and red plot represent the in-plane and out-of-plane sweeping, respectively........................74
Fig. 4.3: The harmonic Hall measurement results for Ta(4)/Co(2)Pt(5) structure (a) First harmonic Hall resistance describing (4.2) (b) Second harmonic Hall resistance with various current density 74
Fig. 4.4: (a) $R2\omega$ as a function of $\cos\phi$, for average current density ranging from $1 - 1.5 \times 1010A/m2$. Graph of $AX + B(2X^4 - X^2)$ is fitted to the data. (b) HD as a function of electric field for various Ta thicknesses ranging from 2 nm to 10 nm. (c) ζDLE as a function of Ta (black) and Ti (red) thickness. 75
Fig. 4.5: (a) R_ω for $+Hy$ (solid square) and $-Hy$ (open circle). Offsets have been applied to the R_ω for better clarity. R_ω for $-Hy$ is flipped for a clearer comparison. Spin accumulation is parallel (antiparallel) to $+Hy$ ($-Hy$), leading to a higher amplitude in the R_ω at the current density of $j_{DC} = 5.0 \times 10^{10}$ A/m^2. (b) Amplitude of ΔR_P with respect to the electric field. The slope of ΔR_P over electric field is $0.11\ m\Omega$ per $\mathrm{kV/m}$................77
Fig. 4.6: Spin accumulation of Ta (black square) and Ti (black triangle), and DL efficiency of Ta (blue square) and Ti (black triangle) with various HM thicknesses ranging from 2 nm to 10 nm. 78
Fig. 5.1: The electronic band structure of a topological insulator and sample structure. (a) The Dirac-like cone of the dispersion at the surface of a topological insulator and real-space interpretation of the surface state of a topological insulator. (b) Schematic structure of Ti/Co/[Ti, Cu, Pt]/BiSb/Ti, where the elements in the square bracket are the different insertion layers 84
Fig. 5.2: Damping-like term characterization by harmonic Hall technique (a) $R_{2\omega}$ as a function of $\cos\phi$, for average current density ranging from 2 to 3×10^{10} A/m^2. (b) Damping-like field as a function of current density in BiSb for different insertion layer. 86
Fig. 5.3: X-ray diffraction results and crystalline size calculations (a) XRD $\theta - 2\theta$ spectra for BiSb heterostructure with different insertion layers grown on SiO2 substrate at $2\theta = 20 - 60°$. The peak for Si has been remove for better clarity. (b) Crystalline size calculated using Scherrer equation for different insertion layers 88
Fig. 5.4: High-resolution transmission electron microscopy (HR-TEM) of Ti/Co/Pt/BiSb/Ti structure. (a) Cross-sectional TEM images of Ti/Co/Pt/BiSb/Ti (b) Electronics diffraction pattern using Fast-Fourier Transform. 89

Fig. 5.5: XRD and spin Hall angle results for varying BiSb thickness (a) Relation of spin Hall angle and crystalline size as a function of BiSb thickness. (b) XRD $\theta - 2\theta$ spectra for BiSb heterostructure with various BiSb thickness at $2\theta = 20 - 30°$. 90
Fig. 5.6: (Top panel) Experimental data for $R2\omega$ as a function of the azimuthal angle, ϕ at different applied external field. (Middle panel) Cosine fit for the experimental data. (Bottom panel) Field-like contribution after subtracting the cosine fitting from experimental data. 92
Fig. 5.7: $R_{2\omega}$ as a function of the inverse of the static fields and demagnetization field. 93
Fig. 6.1: Phenomenological band modelling of BiSb. (a), Spin texture band of BiSb (111) surface without magnetic anisotropy which present a the shape of a Dirac cone. (b), The relation between strength of magnetic anisotropy M (emu/m^2) and the thickness d (nm) of Co. (c-d) Gapped surface states of BiSb (111) under a perpendicular magnetic anisotropy, with strengths of 0.05 (c) and 0.1(d). The size of the surface-states band gap Δ increases linearly with the strength of perpendicular magnetic anisotropy.................................101
Fig. 6.2: (a) Schematic of the heterostructure with varying Co thickness (b) VSM results showing the structure with perpendicular magnetic anisotropy properties 103
Fig. 6.3: Damping-like term characterization by harmonic Hall technique (a) Damping-like field as a function of average current density ranging from 2 to 3×10^{10} A/m^2. (b) Relation of SOT efficiency as a function of Co thickness...104
Fig. 6.4: XRD θ-2θ spectra for Ti/Pt/Co/BiSb/Ti structure where BiSb(012) is the dominating phase. 105
Fig. 7.1: Overview of the proposed work 112

Chapter 1

Introduction

1.1 Background

Thin film magnetism plays an integral role in contemporary data storage and processing technologies. Research in thin film magnetization has continually advanced since the pioneering work in the field [1,2]. The thickness of thin film typically ranges from several micrometers to a few atoms, providing an ideal platform for manipulating and controlling magnetic properties [3,4]. These thin films exhibit unique magnetic properties that differ from their bulk counterparts, largely due to the changes in atomic arrangement, symmetry, and dimensionality [5–7]. The magnetization of the thin films, referring to the magnetic moment per unit volume, arises from ordered atomic magnetic moments within the material, with each moment behaving like a tiny magnet. The alignment of these moments follows specific patterns determined by the material's intrinsic characteristics and external factors.

Magnetization in thin films can be manipulated through a few methods. One primary method is applying an external magnetic field, which can align the magnetic moments along the field direction. Other methods include varying the temperature, and changing the chemical composition or structure of the film [8–11]. Understanding and controlling magnetization in thin films is crucial for developing next-generation magnetic and spintronic devices. For instance, switching the magnetization direction using minimal energy input is a key requirement for efficient magnetic data storage and low-power spintronic devices. This energy efficiency is crucial as the rise of big data and the advancement of artificial intelligence necessitate the development of memory systems with superior energy efficiency and faster processing speeds [12–14]. The relentless evolution of electronic devices is largely driven by continuous improvements in the memory systems they rely on. Factors such as enhanced memory density, reduced latency, and decreased cost per bit have been the industry's pursuits, guiding the development of the contemporary memory storage hierarchy illustrated in Fig. 1.1. This hierarchy contrasts different memory technologies used in the present-day and their respective roles in systems. At the top of the pyramid in Fig. 1.1, CPU and cache have the fastest access to memory. Their superior speed is largely facilitated by the integration of high-speed random-access memory (RAM). There are typically two types of RAMs: dynamic

random-access memory (DRAM) and static random-access memory (SRAM). Assisted by their multiplexing and demultiplexing circuitry, these memory types are capable of high-speed operations and are commonly employed to retain large quantities of data for brief durations. However, one drawback is that this RAM is generally volatile, requiring persistent power to maintain the stored information. This necessity arises as the electric charge held in capacitors progressively diminishes over time [15].

As such, there has been a surge in research interest in developing new technologies that would yield non-volatile memories with enhanced energy efficiency. Some examples of such technologies include, phase-change memory (PCM), resistive random-access memory (RRAM), and magnetoresistive random-access memory (MRAM). The latter example embodies a prominent application in the vast research domain known as spintronics, illustrating the potential and standing out as a promising contender poised to drive the next wave of memory technologies. Spintronics harnesses the spin of electrons for the manipulation of magnetic moments, a property that can be exploited for both the storage and processing of information.

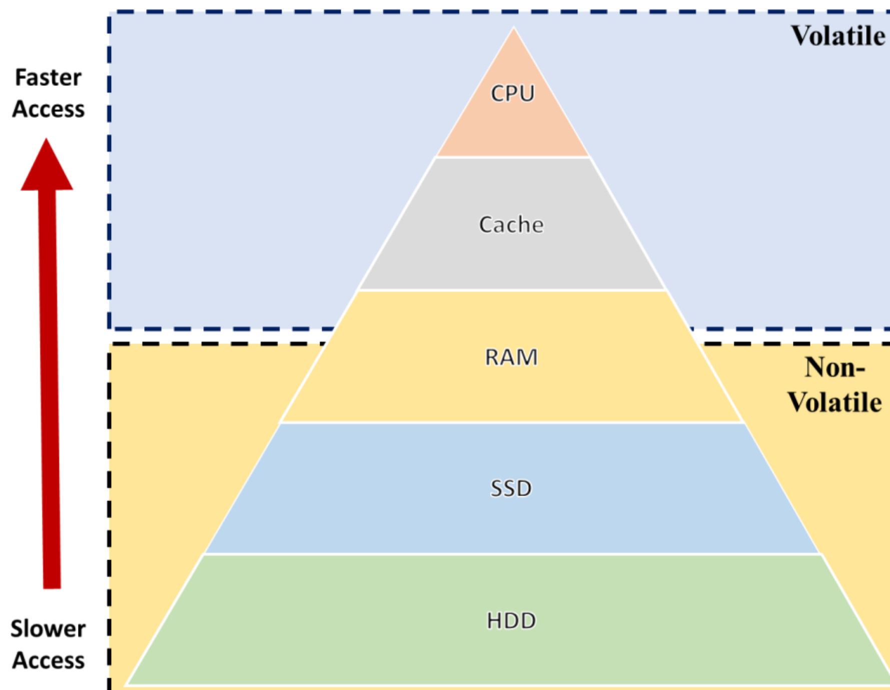

Fig. 1.1: Memory Hierarchy structure depicting different types of memory tiers

1.2 Advancement in Spintronics

The field of spintronics received a significant boost in 1989 with the discovery of Giant Magnetoresistance (GMR) in magnetic multilayer by Albert Fert and Peter Grünberg [16,17]. GMR changes electrical resistance depending on the relative orientation of magnetization in a spin valve structure. As illustrated in Fig. 1.2, when the magnetizations in the spin valve are aligned parallel, the system exhibits low resistance, while an antiparallel alignment results in high resistance. A typical spin valve consists of a tri-layer structure, where a nonmagnetic metal is sandwiched between two ferromagnetic layers. The magnetization of the reference layer is fixed via exchange coupling with an antiferromagnet, while the magnetization of the free layer can switch freely [18]. Utilizing this concept, GMR has been found in numerous applications in magnetic sensors and computer hard-disk drive read-heads [19,20]. This discovery was rapidly followed by the introduction of Tunnel Magnetoresistance (TMR), which occurs when the non-magnetic layer in a GMR structure is replaced with an insulating layer [21]. This TMR displayed a remarkable improvement in magnetoresistance compared to GMR, leading to its implementation as a recording unit in Magnetoresistive Random Access Memory (MRAM). Spintronics continued to progress with the discovery and subsequent investigation of spin-transfer torque (STT).

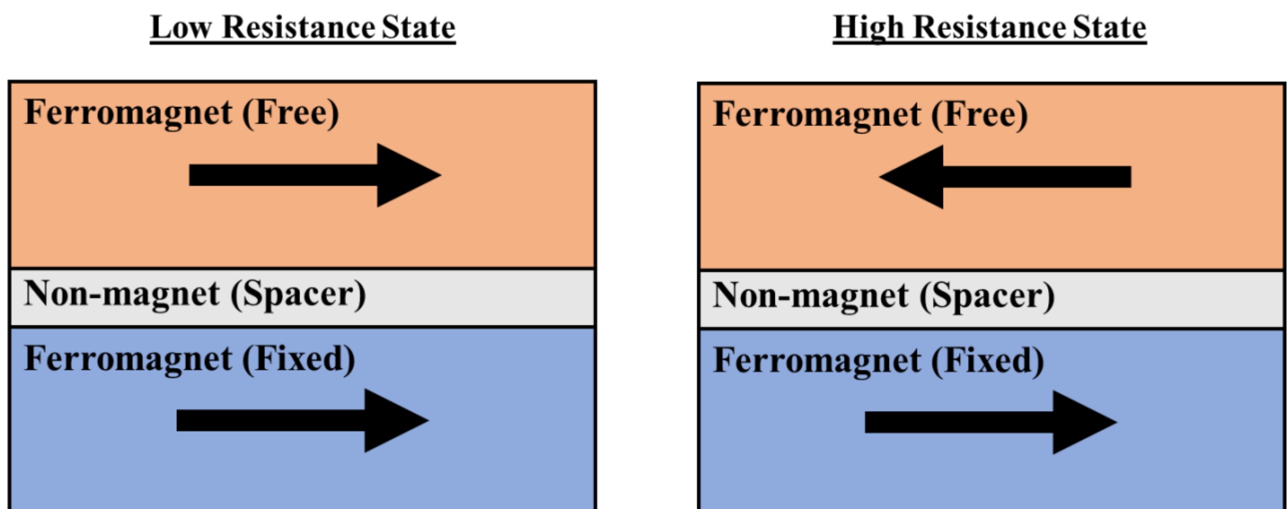

Fig. 1.2: Schematic of giant magnetoresistance (GMR) concept. (Left) Low resistance state when parallel (Right) High resistance state when anti-parallel.

Spin-transfer torque (STT) MRAM, introduced more recently, has emerged as a promising contender for memory storage due to its low power consumption, high density, and

non-volatility [21,22]. The underlying physical phenomenon is based on the spin interaction of the 3*d*-4*s* electrons in the ferromagnetic layer and the conservation of angular momentum. As shown in Fig. 1.3, when an unpolarized electron passes through the fixed layer of a magnetic tunnel junction (MTJ), the 4s electrons become polarized in alignment with the local magnetization in the fixed layer. This polarized electron then exerts a torque on the free layer, flipping its magnetization orientation from antiparallel to parallel. On the other hand, to flip the magnetization from parallel to antiparallel, current will be injected from the free layer. The reflected spin from the fixed layer enables the magnetization to switch from parallel to antiparallel in the free layer. When the magnetization of the free layer is parallel to the fixed layer, they will be in a low-resistance state, likewise, when free and fixed layers are antiparallel to each other, they will be in a high-resistance state. This mechanism of transferring the angular momentum of the spins is known as spin-transfer torque.

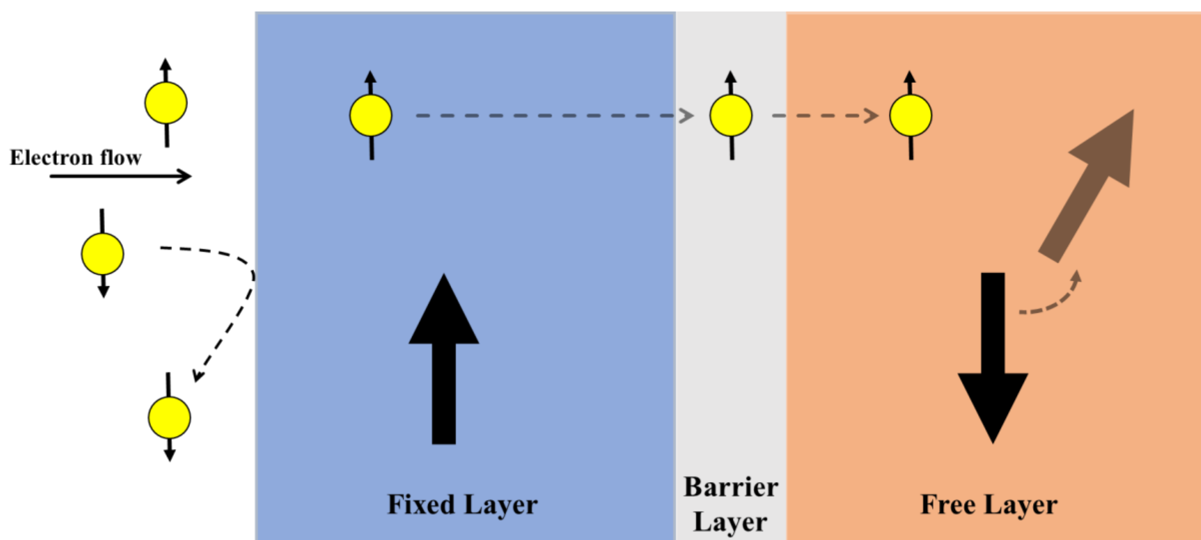

Fig. 1.3: Schematic of spin-transfer torque (STT) mechanism

The discovery of STT has made remarkable advancements in our MRAM technology today. A typical bit cell of STT-MRAM consists of an MTJ structure, where the read and write operation is performed by sensing the magnetoresistance and switching the free layer. Although STT-MRAM has promising power consumption and magnetic retention performance, it has certain drawbacks. Since the reading and writing operations share the same current path, it introduces potential disturbance and interference between these operations. There is a risk of unexpected writing to an MTJ cell during a read operation, leading to reliability issues. Moreover, due to the large write current and thin oxide barrier in STT-MRAM, the dielectric

breakdown might occur in the tunnelling barrier after repeated usage, thus reducing the reliability of STT-MRAM. A potential solution to these read-write disturbances and dielectric breakdown is the application of spin-orbit torque (SOT) switching.

As shown in Fig. 1.4, the SOT-MRAM structure has separate word bit-lines and read bit-lines for read and write operations, respectively. The read operation is similar to that in STT-MRAM devices, where a current less than the threshold current, I_c, is passed through the read bit-line, and the MTJ resistance is determined based on the magnetization of the free layer relative to the fixed layer. In the write mode, current from the write bit-line and access transistor switches the magnetization direction of the perpendicular MTJ. This design allows separate optimization for read and write operations. The SOT-MRAM switching employs an in-plane current-induced SOT, which does not pass through the tunnelling barrier, enhancing endurance and reliability compared to STT-MRAM. A more in-depth understanding of the principles and mechanism of SOT is discussed in Chapter 2.

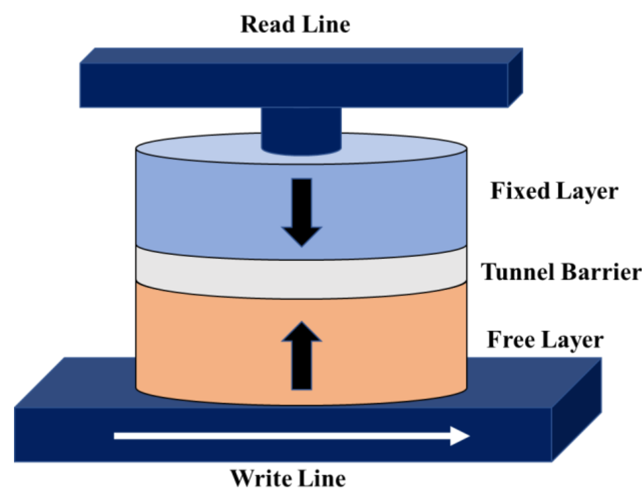

Fig. 1.4: Schematic of SOT-MRAM structure

Spin-Orbit torque (SOT) vs Spin-Transfer Torque (STT)

Although SOT-MRAM employs a larger cell size due to its 3-terminal design, it generally outperforms STT-MRAM at both the cell and array levels, as evidenced by comparative metrics such as read/write times and write energy (Table 1), where SOT-MRAM demonstrates significantly superior performance. Moreover, the endurance of SOT-MRAM is anticipated to exceed that of STT-MRAM, primarily because of the lower current densities required for

switching, which consequently reduce the stress on the device and extend its lifespan. This aspect is crucial in prolonging device reliability and is particularly beneficial in applications.

Table 1: Adapted from [23], performance comparison between STT-MRAM and SOT-MRAM

Parameters	STT-MRAM	SOT-MRAM
Write Time (ns/bit)	5	1
Write Energy(fj/bit)	160	46
Read Time (ps)	146	82
Write Latency (ns)	1.27	0.95
Read Latency (ns)	2.50	2.14

1.3 Motivation

Spin-orbit torque (SOT) has emerged as a highly promising technique for achieving efficient and reliable magnetization switching for memory storage and other applications. Extensive research is being undertaken to identify materials exhibiting a high charge-to-spin conversion efficiency. In order to characterize the SOT efficiency in a material, several quantification techniques are typically employed. These techniques include, spin-torque ferromagnetic resonance (ST-FMR), time-resolve magneto-optical Kerr effect (TR-MOKE), hysteresis loop shift, and harmonic Hall technique [24–31]. However, these characterizations technique have limitations, for instance, not accounting for the spin backflow and spin memory loss. Due to the existence of spin backflow, where the spins are reflected back into the HM layer, and spin memory loss, where the spin flips beyond the spin diffusion length [32–34], quantification of the net spins that diffused into the FM layer from the HM layer has remained unsolved, specifically for FM/HM bilayer structure. The quantification of spin accumulation encounters distinct challenges due to the inherently low signal magnitude associated with this phenomenon. This inherently low signal often imposes limitations on the spatial imaging capabilities, consequently restricting the resolution to the constraints of the optical diffraction limit [35]. A more direct approach to quantify spin accumulation in a ferromagnetic layer within a heavy metal/ferromagnetic (HM/FM) structure is by X-ray magnetic circular dichroism (XMCD). However, applying XMCD necessitates access to a synchrotron facility, a requirement that substantially limits its accessibility and broad applicability. Therefore, a robust and easily accessible characterization technique that can directly quantify the spin

accumulation in the FM layer has been a subject of continued pursuit in the effort of understanding the SOT mechanism.

Given the growing interest in identifying materials that can enhance SOT efficiency, the need for a more efficient characterization technique is becoming increasingly apparent. This SOT efficiency quantifies the conversion of charge to spin current, driving torque on magnetization through spin-orbit coupling. The existing methods for quantifying SOT, as mentioned above, commonly involve the fabrication of micro- or nanoscale devices, which necessitate a series of lithographic processes. These additional steps not only consume valuable resources but also add significantly to the overall processing time. Hence, developing a technique that could reliably characterize SOT efficiencies with minimal processing requirements, reduced equipment dependency, and lower time investment is currently a significant area of focus in the field of spintronics research.

Today, the commonly used material to generate high charge-to-spin conversion are the heavy metal, Platinum (Pt), Tantalum (Ta), and Tungsten (W). These heavy metals can generate a conversion efficiency ranging from 10 to 30%, which are relatively high compared to other normal metals where the conversion is negligible [14,36–43]. Apart from the choice of material, researchers have been continually exploring methods to enhance SOT efficiency, employing techniques such as interfacial engineering, doping, alloying, and strain-engineering [44–51]. While heavy metal-based SOT devices have shown notable advancements, their development still limited by charge-to-spin conversion efficiency of less than 100%. To address this efficiency gap, researchers have investigated alternative materials that might provide higher conversion efficiency. In recent years, attention has been directed towards using unconventional materials, such as topological insulators (TIs). Due to its unique spin-momentum locking and topologically protected surface states, it can generate high charge-to-spin conversion of larger than 100%. Large spin Hall angle, θ_{SH}, has been reported in several TIs, such as $\theta_{SH} = 3.5$ in Bi_2Se_3, $\theta_{SH} = 18.6$ in Bi_xSe_{1-x}, and $\theta_{SH} = 52$ in BiSb/MnGa [52–54]. However, one should be aware that the generally low bulk conductivity state can lead to an overestimation in θ_{SH} if not accurately accounted for in the evaluation. Despite the potential of TIs, the topological surface state (TSS) is sensitive to perturbations. For instance, when a TI interfaces directly with a FM, the discrepancy in the work function between the TI and FM can cause a shift in the TSS below the Fermi energy level. This displacement may lead to the

hybridization of these surface states with the metal bands, subsequently disrupting the helical spin structure, which result in the spin-momentum locking property not preserved [55–58]. Hence, it is crucial to implement interface engineering techniques to preserve the TSS. By investigating the TI-FM interface, we can optimize the device performance by maintaining the TSS, preserving the unique spin-momentum locking property, and thus maximizing the potential of TI-based spintronic devices.

As mentioned earlier, the spin-momentum locking at the TSS is prone to disturbance such as adjacent to a topological insulator with a ferromagnet material. Previously theoretical studies have shown that the SOT generated from the TIs vanished with it is coupled with a ferromagnet with in-plane magnetic anisotropy (IMA) [59–62]. On the contrary, other studies have shown that SOT can be generated even with it is coupled with a ferromagnet with in-plane magnetization [63]. Meanwhile, a ferromagnet with perpendicular magnetic anisotropy (PMA) allows the opening of a gap at the Dirac point, causing the Dirac fermions to be massive [59,60]. These discrepancies in the TI/FM interface are yet to be fully understood. In addition, numerous theoretical models propose varying influences of these magnetic moments on the SOT induced by TIs, but there is still limited experimental work to verify these models [59,60,64,65]. Therefore, a systematic investigation is required to study the influence of magnetic moment on the spin-orbit torque generated by the topological insulator.

1.4 Thesis Outline

The thesis is structured as follows:

Chapter 2 provides a comprehensive examination of the fundamental principles and theoretical framework that govern spin-orbit torque. This chapter begins with a discussion on spin-orbit coupling. We then delved into the generation of spin current from the phenomenon of spin Hall effect and Rashba-Edelstein effect. In the latter part of Chapter 2, I then delved into the discussion on topological insulators in spintronics application. This discussion includes the fundamental properties of topological insulators, such as quantum Hall effect and quantum anomalous Hall effect, which leads to high charge-to-spin conversion, which are crucial for spintronics applications.

Chapter 3 will cover the details of the fabrication process and characterization techniques employed in this work. Here, I also introduce on my work, where I quantify the spin-orbit torque directly in a blanket film without any lithography processes.

In Chapter 4, I establish an all-electrical novel quantification of spin accumulation in the ferromagnetic layer using DC bias harmonic Hall measurements. This newly introduced technique provides an all-electrical alternative to determine spin accumulation by utilizing the easily accessible harmonic Hall characterization technique.

Subsequently, in Chapter 5, I demonstrate the use of various non-magnetic insertion layer materials between the topological insulator and ferromagnet interface to preserve the topological surface state and promote spin-orbit torque efficiency through the crystallinity control of topological insulator.

Next, in Chapter 6, I explore on the influence of magnetic moments on spin-orbit torque that is generated by the topological insulator surface state in a topological insulator – ferromagnet heterostructure. We then constructed a theoretical model to simulate the surface states and provide theoretical evidence for the impact of perpendicular magnetic anisotropy on spin-orbit torque.

Lastly, in Chapter 7, we summarized the work presented in this thesis. In addition, potential future works are proposed to further enhance the strength of spin-orbit torque using topological insulators.

Reference

[1] W. F. Brown, *Thermal Fluctuations of a Single-Domain Particle*, Phys. Rev. **130**, 1677 (1963).

[2] L. Néel, *Magnetism and Local Molecular Field*, Science (80-.). **174**, 985 (1971).

[3] S. Kumar and D. K. Aswal, *Thin Film and Significance of Its Thickness BT - Recent Advances in Thin Films*, in edited by S. Kumar and D. K. Aswal (Springer Singapore, Singapore, 2020), pp. 1–12.

[4] A. Piegari and E. Masetti, *Thin Film Thickness Measurement: A Comparison of Various Techniques*, Thin Solid Films **124**, 249 (1985).

[5] P Poulopoulos and K Baberschke, *Magnetism in Thin Films*, J. Phys. Condens. Matter **11**, 9495 (1999).

[6] S. Kumar, S. K. Sharma, Alimuddin, M. Knobel, R. J. Choudhary, C. G. Lee, B. H. Koo, and R. Kumar, *Structural and Magnetic Properties of Bulk and Thin Films of Mg0.95Mn0.05Fe2O4*, Curr. Appl. Phys. **9**, 1009 (2009).

[7] M. Dobromir, M. Neagu, G. Popa, H. Chiriac, V. Pohoaţă, and C. Hison, *Surface and Bulk Magnetic Behavior of Fe–Si–B Amorphous Thin Films*, J. Magn. Magn. Mater. **316**, e904 (2007).

[8] M. Konc, P. Spisak, P. Kollar, P. Sovak, O. Dusa, and T. Reininger, *Temperature Dependence of the Magnetization and of the Other Physical Properties of Rapidly Quenched Amorphous CoB Alloys*, IEEE Trans. Magn. **30**, 524 (1994).

[9] N. S. E. Osman and T. Moyo, *Temperature Dependence of Coercivity and Magnetization of Sr1/3Mn1/3Co1/3Fe2O4 Ferrite Nanoparticles*, J. Supercond. Nov. Magn. **29**, 361 (2016).

[10] J. Ul Ahsan and H. Singh, *Temperature Dependent Magnetization in Co@Fe Nanoparticles*, Phys. B Condens. Matter **627**, 413488 (2022).

[11] I. M. Obaidat, B. Issa, B. A. Albiss, and Y. Haik, *Temperature Dependence of Saturation Magnetization and Coercivity in Mn0.5Zn0.5Gd0.02Fe1.98O4 Ferrite Nanoparticles*, IOP Conf. Ser. Mater. Sci. Eng. **92**, 12012 (2015).

[12] *CMOS with a Spin*, Nat. Electron. **2**, 263 (2019).

[13] K. L. Wang, J. G. Alzate, and P. Khalili Amiri, *Low-Power Non-Volatile Spintronic Memory: STT-RAM and Beyond*, J. Phys. D. Appl. Phys. **46**, 74003 (2013).

[14] L. Liu, C.-F. Pai, Y. Li, H. W. Tseng, D. C. Ralph, and R. A. Buhrman, *Spin-Torque Switching with the Giant Spin Hall Effect of Tantalum.*, Science **336**, 555 (2012).

[15] H. Iwai, *CMOS Technology after Reaching the Scale Limit*, in *Extended Abstracts - 2008 8th International Workshop on Junction Technology (IWJT '08)* (2008), pp. 1–2.

[16] G. Binasch, P. Grünberg, F. Saurenbach, and W. Zinn, *Enhanced Magnetoresistance in Layered Magnetic Structures with Antiferromagnetic Interlayer Exchange*, Phys. Rev. B **39**, 4828 (1989).

[17] M. N. Baibich, J. M. Broto, A. Fert, F. N. Van Dau, F. Petroff, P. Etienne, G. Creuzet, A. Friederich, and J. Chazelas, *Giant Magnetoresistance of (001)Fe/(001)Cr Magnetic Superlattices*, Phys. Rev. Lett. **61**, 2472 (1988).

[18] B. Dieny, *Giant Magnetoresistance in Spin-Valve Multilayers*, J. Magn. Magn. Mater. **136**, 335 (1994).

[19] S. Parkin, *Spin-Polarized Current in Spin Valves and Magnetic Tunnel Junctions*, MRS Bull. **31**, 389 (2006).

[20] M. A. Khan, J. Sun, B. Li, A. Przybysz, and J. Kosel, *Magnetic Sensors-A Review and Recent Technologies*, Eng. Res. Express **3**, 22005 (2021).

[21] J. S. Moodera, L. R. Kinder, T. M. Wong, and R. Meservey, *Large Magnetoresistance at Room Temperature in Ferromagnetic Thin Film Tunnel Junctions*, Phys. Rev. Lett. **74**, 3273 (1995).

[22] L. Berger, *Emission of Spin Waves by a Magnetic Multilayer Traversed by a Current*, Phys. Rev. B **54**, 9353 (1996).

[23] R. Saha, Y. P. Pundir, and P. Kumar Pal, *Comparative Analysis of STT and SOT Based MRAMs for Last Level Caches*, J. Magn. Magn. Mater. **551**, 169161 (2022).

[24] I. Razdolski, A. Alekhin, U. Martens, D. Bürstel, D. Diesing, M. Münzenberg, U. Bovensiepen, and A. Melnikov, *Analysis of the Time-Resolved Magneto-Optical Kerr Effect for Ultrafast Magnetization Dynamics in Ferromagnetic Thin Films*, J. Phys. Condens. Matter **29**, 174002 (2017).

[25] H. Y. Poh, C. C. I. Ang, T. L. Jin, F. N. Tan, G. J. Lim, S. Wu, F. Poh, and W. S. Lew, *Continuous Film Spin-Orbit Torque Characterization via Four Probe Measurement*, Appl. Phys. Lett. **121**, 12405 (2022).

[26] C.-F. Pai, M. Mann, A. J. Tan, and G. S. D. Beach, *Determination of Spin Torque Efficiencies in Heterostructures with Perpendicular Magnetic Anisotropy*, Phys. Rev. B **93**, 144409 (2016).

[27] H. Y. Poh, C. C. I. Ang, W. L. Gan, G. J. Lim, and W. S. Lew, *Direct Spin Accumulation Quantification in Ferromagnetic Heterostructures Using DC Bias Harmonic Hall Measurement*, Phys. Rev. B **104**, 224416 (2021).

[28] H. Wu et al., *Magnetic Memory Driven by Topological Insulators*, Nat. Commun. **12**, 6251 (2021).

[29] J. Wei, C. He, X. Wang, H. Xu, Y. Liu, Y. Guang, C. Wan, J. Feng, G. Yu, and X. Han, *Characterization of Spin-Orbit Torque Efficiency in Magnetic Heterostructures with Perpendicular Magnetic Anisotropy via Spin-Torque Ferromagnetic Resonance*, Phys. Rev. Appl. **13**, 34041 (2020).

[30] M. Hayashi, J. Kim, M. Yamanouchi, and H. Ohno, *Quantitative Characterization of the Spin-Orbit Torque Using Harmonic Hall Voltage Measurements*, Phys. Rev. B - Condens. Matter Mater. Phys. **89**, 1 (2014).

[31] E. S. Park, D. K. Lee, B. C. Min, and K. J. Lee, *Elimination of Thermoelectric Artifacts in the Harmonic Hall Measurement of Spin-Orbit Torque*, Phys. Rev. B **100**, 214438 (2019).

[32] K. Chen and S. Zhang, *Spin Pumping in the Presence of Spin-Orbit Coupling*, Phys. Rev. Lett. **114**, 126602 (2015).

[33] K. Hashimoto, G. Tatara, and C. Uchiyama, *Spin Backflow: A Non-Markovian Effect on Spin Pumping*, Phys. Rev. B **99**, 205304 (2019).

[34] J. Borge and I. Tokatly, *Ballistic Spin Transport in the Presence of Interfaces with Strong Spin-Orbit Coupling*, Phys. Rev. B **96**, (2017).

[35] J. Ding, W. Zhang, M. B. Jungfleisch, J. E. Pearson, H. Ohldag, V. Novosad, and A. Hoffmann, *Direct Observation of Spin Accumulation in Cu Induced by Spin Pumping*, Phys. Rev. Res. **2**, 13262 (2020).

[36] Y. Wang, P. Deorani, X. Qiu, J. H. Kwon, and H. Yang, *Determination of Intrinsic Spin Hall Angle in Pt*, Appl. Phys. Lett. **105**, 152412 (2014).

[37] F. Luo, Q. Y. Wong, S. Li, F. Tan, G. J. Lim, X. Wang, and W. S. Lew, *Dependence of Spin-Orbit Torque Effective Fields on Magnetization Uniformity in Ta/Co/Pt Structure*, Sci. Rep. **9**, 1 (2019).

[38] E. Sagasta, Y. Omori, S. Vélez, R. Llopis, C. Tollan, A. Chuvilin, L. E. Hueso, M. Gradhand, Y. Otani, and F. Casanova, *Unveiling the Mechanisms of the Spin Hall Effect in Ta*, Phys. Rev. B **98**, 60410 (2018).

[39] L. Wang, K. Shi, S. Peng, K. Cao, H. Yang, J. Gao, W. Zhao, and C. Zhao, *Large Spin Hall Effect of Perpendicularly Magnetized β-W/CoFeB/MgO Layers with High Thermal Stability*, Jpn. J. Appl. Phys. **58**, 50903 (2019).

[40] H. L. Wang, C. H. Du, Y. Pu, R. Adur, P. C. Hammel, and F. Y. Yang, *Scaling of Spin Hall Angle in 3d, 4d, and 5d Metals from YFeO/Metal Spin Pumping*, Phys. Rev. Lett.

112, 197201 (2014).

[41] R. Bansal, G. Nirala, A. Kumar, S. Chaudhary, and P. K. Muduli, *Large Spin Hall Angle in β-W Thin Films Grown on CoFeB without Oxygen Plasma*, SPIN **08**, 1850018 (2018).

[42] R. Yu, B. F. Miao, L. Sun, Q. Liu, J. Du, P. Omelchenko, B. Heinrich, M. Wu, and H. F. Ding, *Determination of Spin Hall Angle and Spin Diffusion Length in ${\beta}$-Phase-Dominated Tantalum*, Phys. Rev. Mater. **2**, 74406 (2018).

[43] K.-U. Demasius, T. Phung, W. Zhang, B. P. Hughes, S.-H. Yang, A. Kellock, W. Han, A. Pushp, and S. S. P. Parkin, *Enhanced Spin-Orbit Torques by Oxygen Incorporation in Tungsten Films.*, Nat. Commun. **7**, 10644 (2016).

[44] M. Obstbaum et al., *Tuning Spin Hall Angles by Alloying*, Phys. Rev. Lett. **117**, 167204 (2016).

[45] L. Zhu, D. C. Ralph, and R. A. Buhrman, *Enhancement of Spin Transparency by Interfacial Alloying*, Phys. Rev. B **99**, 180404 (2019).

[46] T. Zhao et al., *Enhancement of Out-of-Plane Spin–Orbit Torque by Interfacial Modification*, Adv. Mater. **35**, 2208954 (2023).

[47] C.-Y. Hu, Y.-F. Chiu, C.-C. Tsai, C.-M. Lee, M.-Y. Song, S.-J. Lin, X. Bao, and C.-F. Pai, *Interfacial Engineering Strategies for Efficient Spin–Orbit Torque Devices with Pt Alloys*, ACS Appl. Electron. Mater. **5**, 968 (2023).

[48] C.-Y. Hu and C.-F. Pai, *Benchmarking of Spin–Orbit Torque Switching Efficiency in Pt Alloys*, Adv. Quantum Technol. **3**, 2000024 (2020).

[49] G. D. Hwee Wong et al., *Strain-Mediated Spin–Orbit Torque Enhancement in Pt/Co on Flexible Substrate*, ACS Nano **15**, 8319 (2021).

[50] J. Wei et al., *Enhancement of Spin–Orbit Torque by Strain Engineering in SrRuO3 Films*, Adv. Funct. Mater. **31**, 2100380 (2021).

[51] G. D. H. Wong, C. C. I. Ang, W. Gan, W. C. Law, Z. Xu, F. Xu, C. S. Seet, and W. S. Lew, *Reversible Strain-Induced Spin–Orbit Torque on Flexible Substrate*, Appl. Phys. Lett. **119**, 42402 (2021).

[52] H. Y. Poh, C. C. I. Ang, G. J. Lim, T. L. Jin, S. H. Lee, E. K. Koh, F. Poh, and W. S. Lew, *Crystallinity Control of the Topological-Insulator Surface Bi85Sb15 (012) via Interfacial Engineering for Enhanced Spin-Orbit Torque*, Phys. Rev. Appl. **19**, 1 (2023).

[53] A. R. Mellnik et al., *Spin-Transfer Torque Generated by a Topological Insulator*, Nature **511**, 449 (2014).

[54] M. DC et al., *Room-Temperature High Spin–Orbit Torque Due to Quantum Confinement in Sputtered BixSe(1–x) Films*, Nat. Mater. **17**, 800 (2018).

[55] N. Roschewsky, E. S. Walker, P. Gowtham, S. Muschinske, F. Hellman, S. R. Bank, and S. Salahuddin, *Spin-Orbit Torque and Nernst Effect in Bi-Sb/Co Heterostructures*, Phys. Rev. B **99**, 195103 (2019).

[56] P. Noel, C. Thomas, Y. Fu, L. Vila, B. Haas, P. H. Jouneau, S. Gambarelli, T. Meunier, P. Ballet, and J. P. Attané, *Highly Efficient Spin-to-Charge Current Conversion in Strained HgTe Surface States Protected by a HgCdTe Layer*, Phys. Rev. Lett. **120**, 167201 (2018).

[57] J. Zhang, J. P. Velev, X. Dang, and E. Y. Tsymbal, *Band Structure and Spin Texture of ${\mathrm{Bi}}_{2}{\mathrm{Se}}_{3} 3d$ Ferromagnetic Metal Interface*, Phys. Rev. B **94**, 14435 (2016).

[58] J.-C. Rojas-Sánchez et al., *Spin to Charge Conversion at Room Temperature by Spin Pumping into a New Type of Topological Insulator: $\ensuremath{\alpha}$-Sn Films*, Phys. Rev. Lett. **116**, 96602 (2016).

[59] Y. T. Hsu, K. Park, and E. A. Kim, *Hybridization-Induced Interface States in a Topological-Insulator-Ferromagnetic-Metal Heterostructure*, Phys. Rev. B **96**, 235433 (2017).

[60] P. B. Ndiaye, C. A. Akosa, M. H. Fischer, A. Vaezi, E. A. Kim, and A. Manchon, *Dirac Spin-Orbit Torques and Charge Pumping at the Surface of Topological Insulators*, Phys. Rev. B **96**, 014408 (2017).

[61] S. Ghosh and A. Manchon, *Spin-Orbit Torque in a Three-Dimensional Topological Insulator-Ferromagnet Heterostructure: Crossover between Bulk and Surface Transport*, Phys. Rev. B **97**, 1 (2018).

[62] R. S. Akzyanov, *Born Approximation Study of the Strong Disorder in Magnetized Surface States of Topological Insulator*, 1 (2023).

[63] J. Y. Li, R. Q. Wang, M. X. Deng, and M. Yang, *In-Plane Magnetization Effect on Current-Induced Spin-Orbit Torque in a Ferromagnet/Topological Insulator Bilayer with Hexagonal Warping*, Phys. Rev. B **99**, 1 (2019).

[64] Q. Liu, C. X. Liu, C. Xu, X. L. Qi, and S. C. Zhang, *Magnetic Impurities on the Surface of a Topological Insulator*, Phys. Rev. Lett. **102**, 1 (2009).

[65] A. Kosma, P. Rüßmann, S. Blügel, and P. Mavropoulos, *Strong Spin-Orbit Torque Effect on Magnetic Defects Due to Topological Surface State Electrons in Bi_2Se_3*, Phys. Rev. B **102**, 144424 (2020)

Chapter 2

Background in Spin Transport and Topological Insulator

In this chapter, a thorough examination of the underlying principles and theoretical framework of spin-orbit torque is presented. The discussion commences with an analysis of magnetization dynamics, elucidating the diverse components that impact the magnetization of ferromagnetic materials. Subsequently, the generation of spin currents *via* the spin Hall effect mechanism is explored, providing a deeper understanding of the fundamental processes governing spin-orbit torque. In the later part of this chapter, a detailed discussion on topological insulators in Spintronics is covered. This discussion includes the fundamental properties of topological insulators, such as the quantum Hall effect and quantum anomalous Hall effect, which lead to high charge-to-spin conversion, which are crucial for spintronics applications. Lastly, this Chapter also includes a literature review on the current state of the art for topological insulators for spin-orbit torque applications.

2.1 Spintronics: Spin-Orbit Coupling to Spin-Orbit Torque

2.1.1 Spin-Orbit Coupling

The spin-orbit coupling (SOC) is a relativistic interaction between the spin of electrons and their orbital motion around the nucleus in a finite electric field [1–5]. In the electron frame of reference, the electric field generated by the nucleus gives rise to an effective magnetic field that is orthogonal to the electron's trajectory. This effective magnetic field interacts with the magnetic moment associated with the electron's spin, resulting in a Lorentz force that acts perpendicular to the electron's motion. Considering two frames of reference, s for the nucleus, and s', for the electron. The electric field, $\boldsymbol{E}$ and magnetic field, $\boldsymbol{B}$ can be expressed in the respective frame of reference using Lorentz transformation,

$$\boldsymbol{E}'_{\parallel} = \boldsymbol{E}_{\parallel} \qquad \boldsymbol{B}'_{\parallel} = \boldsymbol{B}_{\parallel} \tag{2.1}$$

$$\boldsymbol{E}'_{\perp} = \gamma(\boldsymbol{E}_{\perp} = \boldsymbol{v} \times \boldsymbol{B}) \qquad \boldsymbol{B}_{\perp}{}' = \gamma(\boldsymbol{B}_{\perp} - \frac{1}{c^2}\boldsymbol{v} \times \boldsymbol{E}) \tag{2.2}$$

where $\gamma = \frac{1}{\sqrt{1-v^2/c^2}}$ is the Lorentz factor, and c is the speed of light. The interaction between this $\boldsymbol{B}_{\perp}'$ and the electron's spin is thus call the spin-orbit coupling. The electron possesses an intrinsic spin angular momentum, $\boldsymbol{S}$, which gives rise to a magnetic moment $\boldsymbol{\mu_S}$. The relation between the magnetic moment and the spin angular momentum can be described as $\boldsymbol{\mu_S} = -\frac{e}{m_e}\boldsymbol{S}$, where e is the electron charge and m_e is the effective mass of electron. Due to the Heisenberg uncertainty principle, the precise measurement of $\boldsymbol{S}$ is not possible. Instead, we can visualize $\boldsymbol{S}$ as a vector precessing around the $\hat{z}$ -axis. For an electron, the projections of $\boldsymbol{S}$ can assume two quantized values, $\boldsymbol{S}_z = \hbar m_s$, where $m_s = \pm\frac{1}{2}$, representing the magnetic spin quantum number. The energy interaction between the magnetic moment and the magnetic field is expressed as $E_{SOC} = -\boldsymbol{\mu_S}.\boldsymbol{B}_{\perp}'$. This interaction gives rise to two distinct energy states for the system: the low-energy state, where $\boldsymbol{\mu_S} \parallel \boldsymbol{B}_{\perp}'$, and the high-energy state, where $-\boldsymbol{\mu_S} \parallel \boldsymbol{B}_{\perp}'$. Consequently, due to energy minimization, the most favorable configuration occurs when the spins align parallel to the magnetic field. Thus, the Hamiltonian that arises from SOC, H_{SOC} can then be defined as [6],

$$H_{SOC} = \frac{\hbar}{4m^2c^2}(\nabla V \times \boldsymbol{p}).\boldsymbol{\sigma} \tag{2.3}$$

This spin-orbit coupling can be categorized into (i) Symmetry-independent, and (ii) symmetry-dependent. The former originates from atomic orbitals and is present in all types of crystals, while the latter only exists in crystals without inversion symmetry [6].

In a periodic crystal, the spin degeneracy of electron and hole states arises from the combined effect of spatial inversion symmetry and time reversal symmetry. Both symmetry operations transform the wave vector k into $-k$, but time-reversal also flips the spin. This can be expressed as follows:

$$\text{Time reversal symmetry: } E_{\pm}(k) = E_{\mp}(-k) \tag{2.4}$$

$$\text{Space inversion symmetry: } E_{\pm}(k) = E_{\pm}(-k) \tag{2.5}$$

This spin degeneracy of electron and hole states must be broken to generate a spin-polarized current. Consequently, either time reversal symmetry or spatial inversion symmetry should be

broken. One way to break this symmetry is by applying a magnetic field, resulting in the generation of spin-polarized current.

2.1.2 Spin Hall Effect

The spin Hall effect (SHE) has gained significant interest from the spintronics community since the first prediction by Mikhail I. Dyakonov and Vladimir I. Perel in 1971 [7,8]. Spin Hall effect is a relativistic spin-orbit coupling interaction which generates spin current from charge current in materials with strong spin-orbit coupling (SOC) due to spin-dependent scattering mechanisms [9–12]. Similarly, the opposite effect, inverse spin Hall effect (ISHE), allows the conversion from spin current to charge current when current passes through a material with high SOC [13–15].

The spin polarization from the spin Hall effect (SHE) is orthogonal to both the transverse spin current and longitudinal charge current, as depicted in Fig. 2.1. This arises due to the strong spin-orbit coupling in the material, which causes a spatial separation of spin polarizations and generates a transverse spin current [16–18]. The generated spin current is defined as, $J_s = \theta_{SH}(J_c \times \hat{\sigma})$, where $\hat{\sigma}$ is the spin polarization direction, θ_{SH} is the spin Hall angle. The spin Hall angle serves as a measure of charge-to-spin conversion efficiency and can be expressed as $\theta_{SH} = \frac{J_s}{J_c}$. Numerous studies have been conducted to achieve higher charge-to-spin efficiency, primarily focusing on the three contributing factors to the SHE: intrinsic scattering (Berry phase) and extrinsic scattering (Skew-scattering and side-jump scattering) [19–25]. The following subsection will provide an in-depth discussion on these spin-scattering mechanisms.

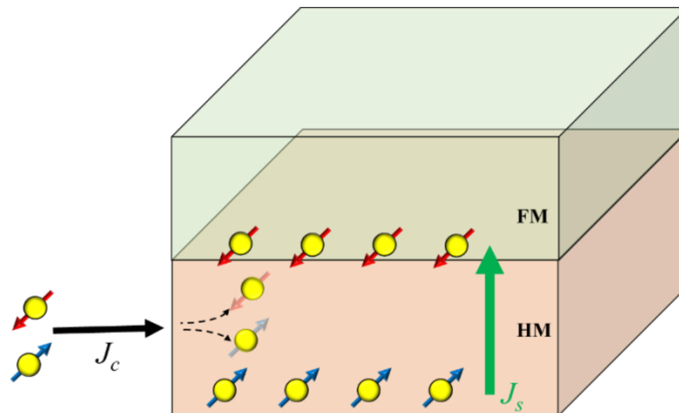

Fig. 2.1: Schematic of spin Hall effect (SHE), where the current is injected into the heavy metal (HM) layer, and due to strong spin-orbit coupling (SOC), the electrons are scattered depending on the orientation of their spin.

Extrinsic Scattering

The spin-orbit interaction refers to the coupling between an electron's spin and its orbital angular momentum. This interaction arises due to the relativistic motion of electrons in a magnetic field produced by the positively charged atomic nucleus. The spin-orbit Hamiltonian can be written as,

$$H_{so} = \lambda_{so}\hat{l}\,.\hat{s}, \tag{2.6}$$

where λ_{SO} is the spin-orbit coupling constant, $\hat{l}$ and $\hat{s}$ are the orbital angular momentum operator and spin angular momentum operator, respectively. The presence of impurities induces an electric field, and when the electron passes through these impurities, it experiences a magnetic field orthogonal to its velocity in the electron frame of reference. The magnetic field due to the spin-orbit interaction is defined as $B_{so} = \frac{\mu_0 Zev}{4\pi r^2}$. The interaction energy, ϵ_{so} can be written as,

$$\epsilon_{so} = -\mu_B B_{so}, \tag{2.7}$$

where μ_B is the Bohr magneton. There are two types of spin-dependent scattering mechanisms due to extrinsic spin-orbit interaction: Skew scattering and side-jump scattering.

Skew scattering

Skew scattering is a spin-splitting process where electrons scatter against a positively charged impurity, taking different scattering angles depending on their spins. This mechanism was based on asymmetric scattering by Mott [26]. In the presence of impurities, the extent of the deflection experienced by electrons depends on the difference in spin-orbit coupling between the impurity and the host material [27–29]. Heavier metals typically exhibit stronger spin-orbit interaction than lighter elements, as shown in (2.2). Due to this SOC, the magnetic force will deflect the electrons left or right depending on the electron's spin. This spin-dependent force differentially influences the motion of electrons with varying spin orientations,

resulting in the separation of electron spins. The illustration of these mechanisms is shown in Fig. 2.2.

Side-jump scattering

The side-jump mechanisms were first proposed by Smith in the 1950s and later introduced again by Berger in 1970 [30–32]. This mechanism induces a spin-dependent transverse displacement of an electron wave package upon collision with a charged impurity. Unlike skew scattering, the side-jump contribution to the spin Hall conductivity is independent of scattering processes. As a result, the spin Hall resistivity, arising due to the side-jump mechanism, can be expressed as:

$$\rho_{xy}^{SH} = a\rho_{xx} + b\rho_{xx}^2, \tag{2.8}$$

where a and b is are the side-jump and skew-scattering contributions, respectively. The illustration of these mechanisms is shown in Fig. 2.2.

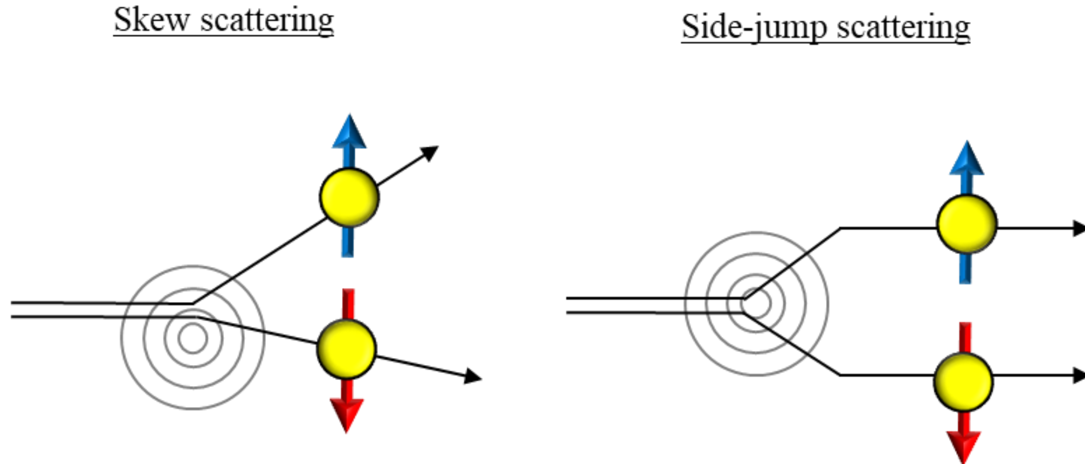

Fig. 2.2: Schematic of extrinsic scattering (Left) Skew scattering (Right) Side-jump scattering

Intrinsic Scattering

In the intrinsic scattering mechanism, it is dependent purely on the electronic band structures of the material [33,34]. When an electric field, $\boldsymbol{E}$, is applied it accelerates the electrons, causing them to acquire a spin-dependent anomalous velocity. This anomalous

velocity is orthogonal to $\boldsymbol{E}$, and is proportional to the integral of the Berry curvature for each occupied band over the Fermi surface. This can be expressed as,

$$\boldsymbol{v} = e\boldsymbol{E} \times \boldsymbol{\Omega}, \tag{2.9}$$

where $\boldsymbol{\Omega}$ is the Berry phase curvature. This $\boldsymbol{\Omega}$ can be interpreted as an effective magnetic field in k-space of the Rashba spin-split band structure. This term is independent of any disorder in the material. The estimation of the Berry curvature can be obtained through *ab-initio* calculations [35]. Experimental results have shown that the intrinsic scattering is the dominating mechanism to the spin Hall effect for heavy metal. Theoretical calculations have predicted large charge-to-spin conversion efficiency, and the opposite in sign for Pt and Ta, which is well-verified in experimental work. The intrinsic mechanism correlates the sign of spin Hall angle to the band filling [36]. In the case where the noble metal has more than a half-filled d-band (Pt, Pd, Ir, Au), the spin Hall angle will be positive [36–40]. On the other hand, the spin Hall angle will be negative in heavy metal with less than a half-filled d-band (Ta, W, Mo) [38,41–45].

2.1.3 Rashba-Edelstein Effect

The Rashba-Edelstein effect (REE) is a spin-orbit interaction phenomenon that manifests in systems lacking inversion symmetry, particularly at interfaces between two dissimilar materials [46–51]. This absence of inversion symmetry leads to electric field, E $= E\hat{z}$, where E is the electric field and $\hat{z}$ is the unit vector surface normal. This can be defined as [34],

$$H_R = \alpha_R \hat{\boldsymbol{\sigma}}.\left(z \times \hat{\boldsymbol{k}}\right), \tag{2.10}$$

where α_R is the Rashba coefficient, $\hat{\boldsymbol{\sigma}}$ is the Pauli spin matrix operator, and $\hat{\boldsymbol{k}}$ is the wavevector operator. Conversely, the symmetric atomic potential, ∇V_a is typically larger than the crystal potential field ($\nabla V_a \gg \nabla V_{cf}$). As such, the potential gradient in the solid state is dominated by the potential drop close to the nucleus [52]. However, the significance of Rashba SOC becomes apparent when considering the Bloch wavefunctions of conduction electrons. The asymmetry in the potential at surfaces or interfaces distorts these wavefunctions, enhancing the orbital

component of the spin-orbit interaction. This interaction between the distorted Bloch wavefunctions and the asymmetric potential at the surface leads to a strong atomic spin-orbit coupling effect, observed as the Rashba-Edelstein effect (REE).

The REE can be considered as 2D electron gas model, representative of the electronic bands at a material surface. Fig. 2.3 depicts two different scenarios: (a) when the space-inversion symmetry is preserved, and (b) when space-inversion symmetry is broken, which leads to a momentum-dependent spin splitting in the electronic bands. This splitting is due to the Rashba field $\boldsymbol{B'}_{\perp}$, that points in varying directions depending on the equilibrium direction, $\boldsymbol{k}$.

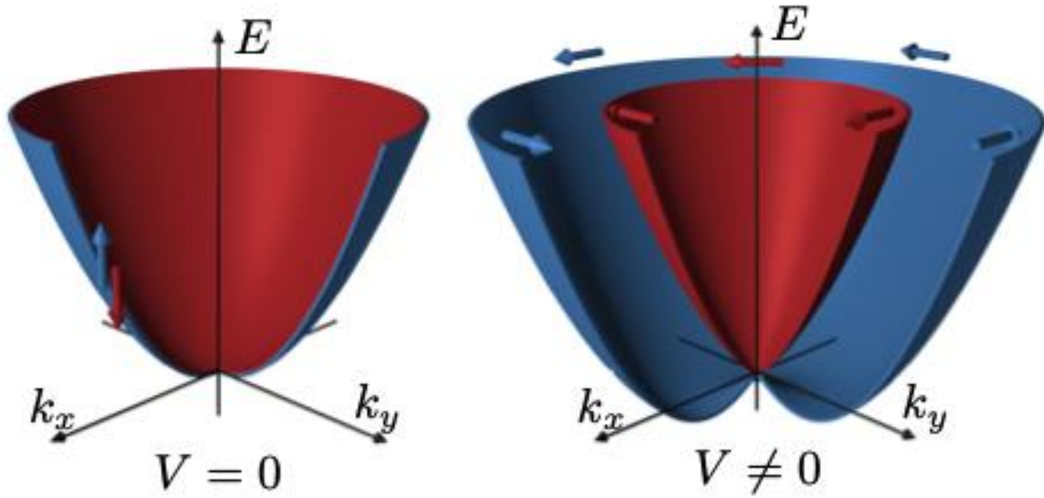

Fig. 2.3: Energy dispersion of 2DEG, $E \propto k^2$ (a) with space-inversion symmetry, and (b) broken space-inversion symmetry. Figure is adapted from [50].

Figure 2.4 shows the Fermi surface at equilibrium and perturbed Fermi surface, respectively. The perturbation in the Fermi surface is due to the applied electric field along the $-x$-direction, as such, this Rashba field allows the quantization of spin to be in the y-axis. The applied electric field will shift the Fermi surfaces of both bands such that the red band is dominated by spin-down electrons and the blue band by spin-up electrons. As a result, the induced current has a net spin-up polarization. $(S_{y_{\uparrow}} > S_{y_{\downarrow}} \rightarrow +y)$. We define the spin-polarized current vector, J_S, as the difference between the current vectors of electrons with upward and downward spins, $J_{\uparrow}$ and $J_{\downarrow}$, respectively, while the charge current J_c is defined as their sum [50]. A pure spin current only carries the spin angular momentum. This model shows

the Rashba-Edelstein effect as an effective mechanism for charge-to-spin conversion, enabling the generation of a spin polarization that is parallel to the y-axis, when the current is injected along the x-direction.

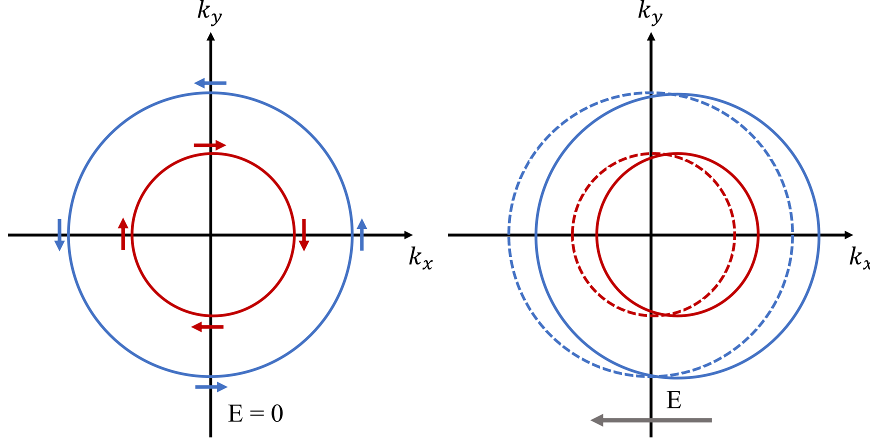

Fig. 2.4: Fermi surface of the (a) Fermi surface of a split band at equilibrium (b) Fermi surface of a split band under applied electric field along the x-direction

2.1.4 Magnetization Dynamics

The magnetization dynamic is first introduced by Landau and Lifshitz in 1935, which is described as [53] ,

$$\frac{\partial \boldsymbol{M}}{\partial t} = -\gamma \mu_0 \boldsymbol{M} \times \boldsymbol{H_{eff}}, \tag{2.11}$$

where $\boldsymbol{M}$ is the magnetization vector, $\gamma = \frac{ge}{2m_e}$ is the gyromagnetic ratio, g is the g-factor, and $\boldsymbol{H_{eff}}$ is the effective field. The $\boldsymbol{H_{eff}}$ is comprised of a combination of external magnetic field, $\boldsymbol{H_{ext}}$, demagnetization field, $\boldsymbol{H_{demag}}$, anisotropy field, $\boldsymbol{H_{ani}}$. From (2.11), one can observed that the $\boldsymbol{M}$ will experience a precessional motion with the precession axis aligned along the direction of $\boldsymbol{H_{eff}}$. This precession as described in (2.11) is an undamped precession, with a constant precessional cone angle. However, when the magnetization misaligned with $\boldsymbol{H_{eff}}$, a finite time is required for the magnetization to change its precession trajectory to the direction of minimal energy. As such, Gilbert introduced a damping term to the LL model, which is known as the Landau-Lifshitz-Gilbert (LLG) equation. This LLG equation is defined as [53],

$$\frac{\partial \boldsymbol{M}}{\partial t} = -\gamma\mu_0 \boldsymbol{M} \times \boldsymbol{H_{eff}} - \alpha \boldsymbol{M} \times \frac{\partial \boldsymbol{M}}{\partial t}, \tag{2.12}$$

where α is the Gilbert damping, where the former and latter terms on the right correspond to the precession terms and damping terms, respectively. The magnetization dynamics is illustrated in Fig. 2.5.

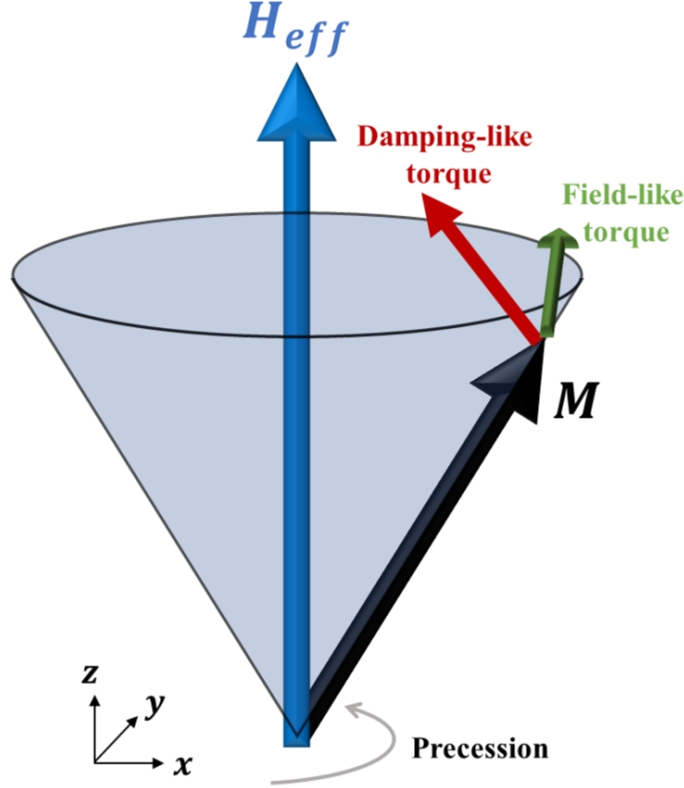

Fig. 2.5: Illustration of magnetization dynamics governed by the Landau-Lifshitz Gilbert (LLG) equations. The black arrow, *M*, is the magnetization of a ferromagnet, and the blue arrow represents the effective field, H_{eff}. The red and green arrows represent damping and field-like torque, respectively, where they are mutually orthogonal to each other.

Now, considering a spin-polarized electrons injected in a ferromagnetic layer. The magnetization of the ferromagnetic layer will experience a torque from the polarized spin. In 1996, Slonczewski further modified the LLG equation to account for this current-induced torque. This Landau-Lifshitz-Gilbert-Slonczewski (LLGS) equation is defined as,

$$\frac{\partial \boldsymbol{M}}{\partial t} = -\gamma\mu_0 \boldsymbol{M} \times \boldsymbol{H_{eff}} - \alpha \boldsymbol{M} \times \frac{\partial \boldsymbol{M}}{\partial t} + \tau_{DL} \boldsymbol{M} \times (\boldsymbol{\sigma} \times \boldsymbol{M}) + \tau_{FL} \boldsymbol{\sigma} \times \boldsymbol{M} \tag{2.13}$$

where the third and fourth term on the right corresponds to the current-induced damping-like and field-like torque, respectively, and $\boldsymbol{\sigma}$ is the spin polarization orientation.

2.2 Topological Insulator in Spintronics

Topological insulator (TIs) is a class of material where the bulk exhibits insulating behavior while supporting conducting states at its surface or edges. These conducting states are a result of strong spin-orbit coupling and are topologically protected, hence, they are robust against perturbations such as impurities or minor structural disorders. As such, Tis have gained numerous attention in the field of spintronics application. These materials are distinguished by their unique topological features and intrinsic band structure, resulting in efficient charge-to-spin conversion.

In this section, an in-dept analysis is discussed on the role of topological insulators in spintronics, and emphasizing the physics of spin-polarized currents and spin-momentum locking.

2.2.1 Quantum Hall Effect

The Quantum Hall Effect (QHE) is a remarkable quantum phenomenon observed in two-dimensional electron systems under the influence of a strong perpendicular magnetic field. This quantized version of Hall effect was first proposed in a 2D electron gas system in 1970s [54], and later observed by Klaus v. Klitzing in 1980 [55]. QHE has since become a subject of extensive study in condensed matter physics, providing deep insights into the nature of electronic states in low-dimensional systems and the role of topology in solid-state physic [56–61].

In the QHE system, the Hall conductivity becomes quantized under a strong magnetic field,

$$\sigma_{xy} = \frac{e^2}{2\pi\hbar}\upsilon, \tag{2.14}$$

where υ assumes any integer value. It has been experimentally demonstrated that a 2D confined electron gas exhibits a Hall resistance characterized by a plateau-like structure as shown in Fig. 2.6. This result significantly differs from the classical Hall resistivity, where

linearity is observed. Also, as described in (2.14), the quantization is independent of materials properties and impurities.

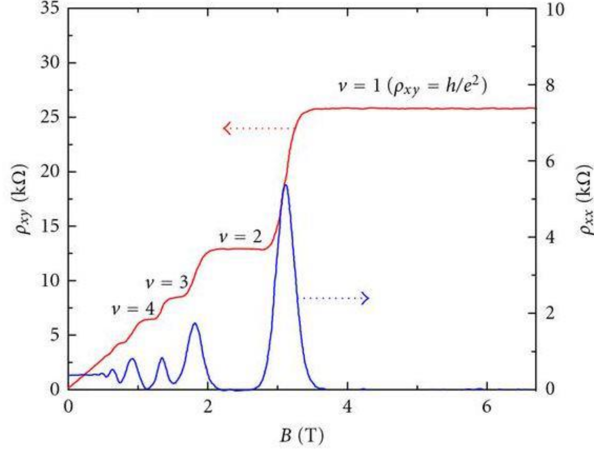

Fig. 2.6 Typical quantum Hall effect results, measured at 30mK in InGaAs-based heterostructure, adopted from [62].

In the presence of strong magnetic field, the 2D electron gas will exhibit quantized cyclotron motions, resulting in the discrete energy level, known as Landau levels. Given a magnetic field along the $\hat{z}$-direction, using the Landau gauge $\boldsymbol{A} = By\hat{x}$, the Hamiltonian can be written as,

$$H = \frac{1}{2m}\left(p_x + \frac{eBy}{c}\right)^2 + \frac{1}{2m}p_y^2, \tag{2.15}$$

We can then solve this Hamiltonian by separating the variable x and y, $\psi(x,y) = \frac{1}{2\pi}e^{ikx}\phi(y)$. The Hamiltonian can be redefined as,

$$\left[-\frac{\hbar^2}{2m}\partial_y^2 + \frac{1}{2}m\omega_c^2(y - y_0)\right]\phi(y) = E\phi(y), \tag{2.16}$$

where $\omega_c = eB/m$ is the cyclotron frequency, and $y_0 = k\sqrt{\frac{\hbar}{m\omega_c}}$. One can note that (2.16) exhibits the form of quantum harmonic oscillator. Thus, the solution to the time-dependent equation is given by,

$$\phi(x,y,t) = \frac{1}{2\pi}e^{i(kx-\omega_c t)}\Phi_{\mathrm{n}}(y - y_0), \tag{2.17}$$

thus, the electrons occupied at the Landau levels at specific quantized energy with the energies given by,

$$E_n = \left(n + \frac{1}{2}\right)\hbar\omega_c, \tag{2.18}$$

This result shows that when a strong magnetic field is applied to a system of free electrons, the energy landscape of the system undergoes a significant transformation. These electrons, originally obeying the principles of Dirac-Fermi statistics, are subjected to quantization of their energy states. The resulting quantized states have an energy gap of $\hbar\omega_c$, which manifests a direct proportionality to the applied magnetic field. With increasing magnetic field, Landau levels rise in energy and can intersect the chemical potential of the system. Depending on whether the chemical potential falls within a gap or lies within a Landau level, the 2D electron gas can take on semiconductor-like insulating properties or metallic conducting properties, respectively. This results in a periodic oscillation of resistance with respect to the inverse of the magnetic field [63–65].

The QHE is protected by the time-reversal symmetry, which ensures that the edge states in the system remain gapless and contribute to the observed quantized Hall resistance [66,67]. In a semi-classical picture, the influence of a strong external magnetic field on a 2D electron system induces localized cyclotron orbits, as illustrated in Fig. 2.7. This direction of cyclotron motions, or chirality, is determined by the sign of both the charge and the magnetic field. Interestingly, for the electrons that locate at the edge state of the system, these electrons bounce off the boundary and continue to move along the 1D edge via a series of skipping cyclotron orbits. As a result, edge transport is immune to backscattering, leading to a dissipationless conduction channel.

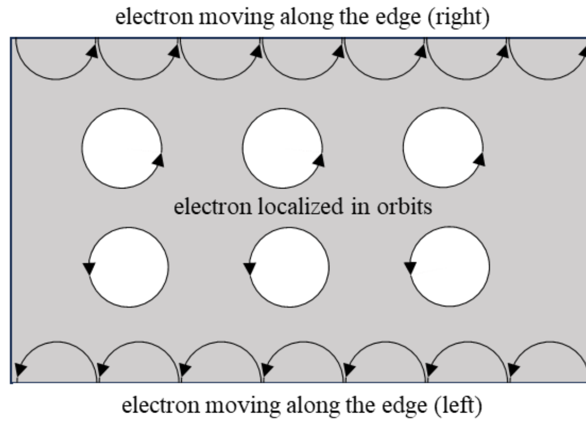

Fig. 2.7: Schematic of chiral conductive edge

2.2.2 Quantum Spin Hall Effect

The Quantum Spin Hall Effect (QSHE) concept originated from the theoretical work of Kane and Mele in 2005 [68]. It later became experimentally substantiated in 2007 through research on HgTe wells. The QSHE is defined by the presence of two non-dissipative edge states, each exhibiting contrasting attributes: opposite spins, propagation directions, Chern numbers, and chirality, as depicted in Fig. 2.8. The separation between the spin-up and spin-down charge edge states can be accomplished in materials that demonstrate an inverted band structure, a result of strong spin-orbit coupling (SOC).

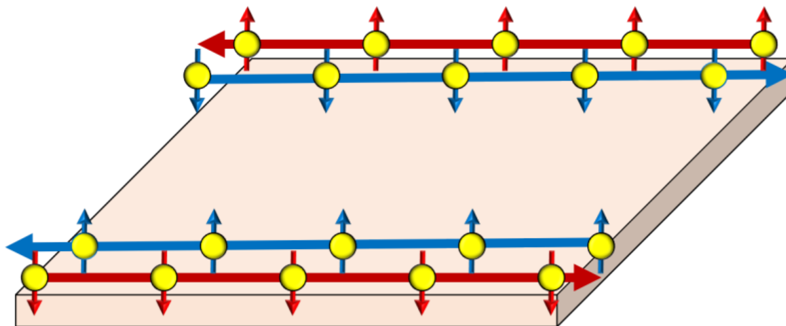

Fig. 2.8: Schematic of quantum spin Hall effect (QSHE)

Similarly to QHE, the QSHE is characterized by an insulating bulk, while its edge conduction is dissipationless. Due to strong SOC, it confines the direction of electron depending on the spin state. In order to reverse the trajectory, the spin state of the electron must be flipped, however this is impossible as it is constrained by the time-reversal symmetry (TRS).

These edge states of differing chirality form a Kramer's pair, with each state being degenerate to the other. Kramer's degeneracy theorem stipulates that, for each energy eigenstate of a TRS system with a half-integer total spin, there must be at least one other degenerate eigenstate. The time-reversal operator, T, is anti-unitary, giving $T^2 = 1$ for integer angular momentum. In contrast, for half-odd-integer angular momentum, we have $T^2 = -1$, indicating the presence of a degenerate state. Also, the matrix elements of a TR-invariant perturbation between two Kramer's degenerate states vanish, thus not allowing any backscattering or hybridization between the spin-up and spin-down states. As a result, the edge conduction in QSHE, which is dissipationless, is protected by TRS. From an energy band perspective, Kramer's theorem also necessitates the intersection of the edge state at a high-symmetry point in the Brillouin zone. This results in two 1D Dirac bands that correspond to the helical edge states intersecting each other at k = 0.

2.2.3 Quantum Anomalous Hall effect

The quantum Anomalous Hall effect (QAHE) was first proposed in 1988 by Haldane [68]. It represents a unique state of topological matter that combines the characteristics of quantum Hall and topological insulator states. Unlike the QHE, which requires strong external magnetic fields to obtain quantization state, the QAHE can achieve this quantization state without any external field. This quantization state is achieved by the influence of local magnetic moments and strong spin-orbit coupling (SOC) within the heterostructure. Although this spontaneous magnetization can break time-reversal symmetry, such a system is experimentally hard to achieve. However, the topological surface state is no longer protected when the TI is confined into a 2D limit and introduce magnetism. Given an out-of-plane magnetization, the Hamiltonian for the surface is written as,

$$H = v_F\left(-k_y\sigma_x + k_x\sigma_y\right) + m\sigma_z, \tag{2.19}$$

From (2.19), the introduction of magnetic interaction into the topological insulators causes the opening of a mass gap at the Dirac point, resulting in the Dirac surface state to be massive. Interestingly, a chiral edge state similar to that in the QHE forms within this gap. For a non-magnetic TI, if the Fermi level lies within the bulk gap, the sample will exhibit an insulator in bulk and conduct on the surface. On the other hand, for MTIs, given the Fermi

level lies within the surface gap, both the bulk and surface will exhibit insulating behaviour, but there is still dissipationless transport of electrons. The first experimental observation of QAHE was reported in Cr-doped $(Bi\text{-}Sb)_2Te_3$ thin films, which were grown on $SrTiO_3$ [69]. At a low temperature of 30 mK, when the gating voltage is adjusted to achieve charge neutrality at -1.5V, the Hall resistance (R_{xy}) attains a quantized value of h/e^2. This quantization corresponds to a significant decrease in the longitudinal resistance (R_{xx}), indicative of dissipationless edges. When the gating voltage shifts the Fermi level away from the gap, this distinctive quantum behavior diminishes.

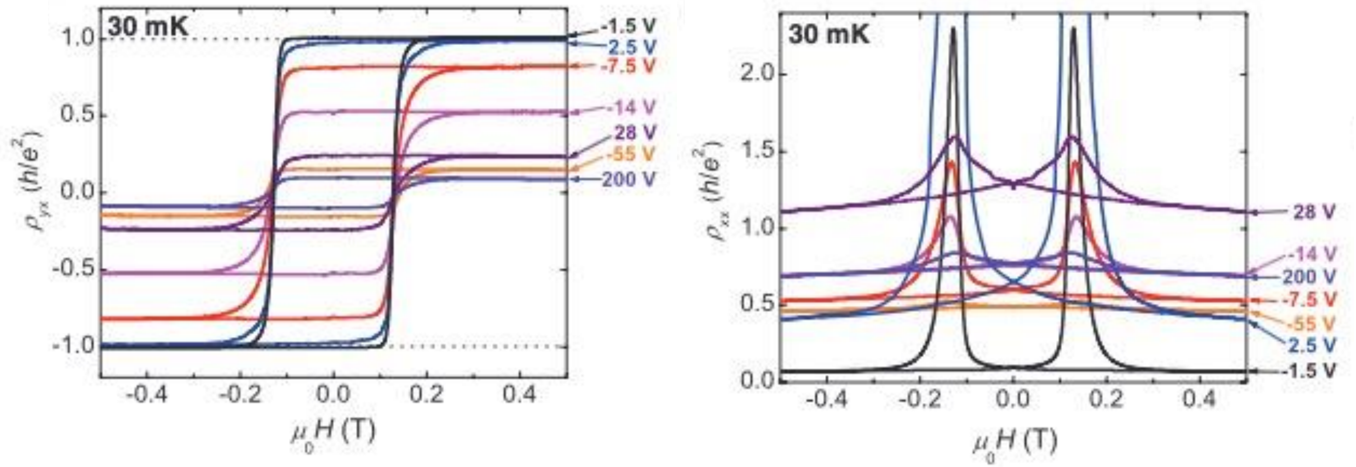

Fig. 2.9: Observation of Quantum Anomalous Hall effect at 30mK in Cr-doped $(Bi\text{-}Sb)_2Te_3$ thin films. (Left) ρ_{xy} with varying magnetic field at different gate voltage. (Right) ρ_{xx} with varying magnetic field at different gate voltage.

2.2.4 3D Topological Insulator

The 3D topological insulators, an advancement from 2D quantum spin Hall insulators, were theoretically proposed prior to experimental validation [70]. Fu and Kane postulated the $Bi_{1-x}Sb_x$ system as a potential 3D topological insulator, which was later confirmed through ARPES characterization of bulk crystals. These systems exhibit a unique trait: in the presence of time-reversal symmetry, surface state electrons can only scatter to antipodal momentum by concomitantly reversing their spin direction, mirroring the 2D topological insulator case. Subsequently, the family of Bi_2Se_3 and Bi_2Te_3 were then reported and discussed [71–74]. Fig.2.10 shows the ARPES measurement of the Bi_2Se_3 crystal where robust surface states are observed. This surface state shows the presence of Dirac surface state, which has a linear relation with the momentum vector.

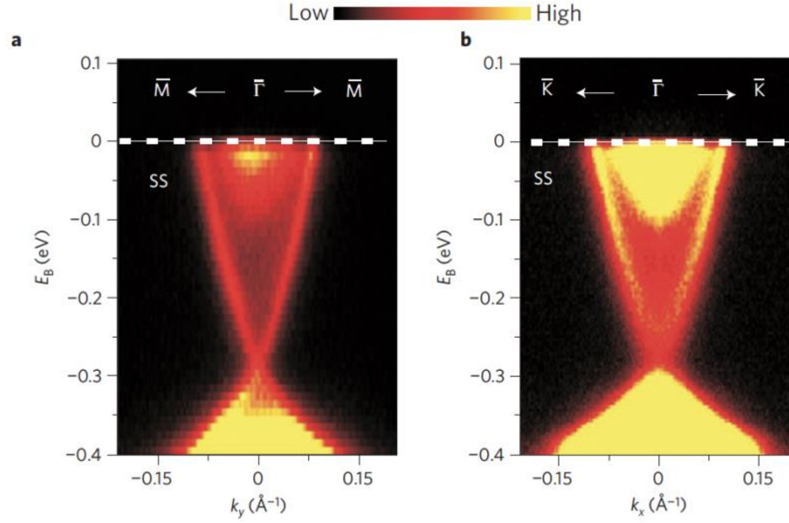

Fig. 2.10: ARPES measurements of surface electronics band dispersion on Bi_2Se_3(111) around the Γ- point. Adapted from [72].

One may visualize a 3D topological insulator as a stack of a 2D QSH system, as shown in Fig. 2.11. This may be due to the fact that that the Fermi surface encloses two of the Γ points, in which it is sensitive to disorder as the surface state is not protected by TRS. On the other hand, if only a single Γ point is enclosed, a strong topological insulator is formed, as shown in Fig. 2.11. This 2D Fermi can be extended to 3D as it is a slab cut out in the x-y momentum plane from the 3D dispersion cone. As such, it is crucial to understand the numbers of Gamma points enclosed by Fermi surface as the number of Gamma points enclosed by the Fermi surface is integral to determine the material's topological class via the Z_2 invariant. This count directly influences whether the material exhibits topologically protected surface states, which is crucial for applications exploiting the unique properties of topological insulators.

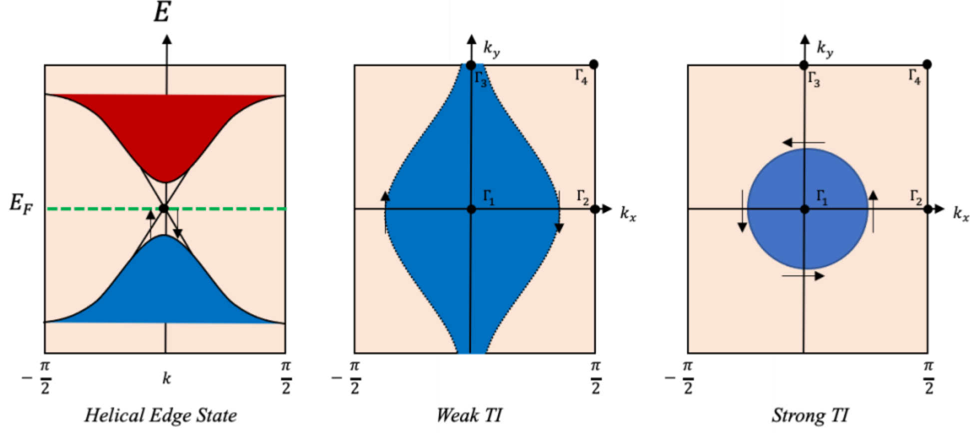

Fig. 2.11: (Left) Surface state dispersion (Middle) Weak TI where the Fermi contour enclosing even Γ points (Right) Strong TI where the Fermi contour enclose an odd number of Γ points

2.2.5 Spin-Orbit Torque in Topological Insulator

Topological insulator (TI) is a promising candidate for replacing heavy metals in spintronics applications due to their large charge-to-spin conversion [75–78]. One prominent feature of TIs is that their surface state is protected by TRS. The surface state in a 3D TIs can be considered as a 2D massless Dirac fermion, exhibiting spin-momentum locking properties. Under the influence of an applied electric field, it will induce a non-equilibrium spin accumulation generating a polarized electron. These polarized electrons can exchange their angular momentum with the adjacent ferromagnetic layer, thus switching its initial magnetization state, also known as spin-orbit torque (SOT). Numerous experiments have shown that the charge-to-spin conversion in TIs is a few order larger than the conventional heavy metals such as Pt, W and Ta [36,37,79–83].

The TIs and ferromagnetic insulator (FMI) system has been studied extensively [84–89]. The Hamiltonian of the bilayer TI/FMI is defined as,

$$H = v_F \hat{\boldsymbol{\sigma}} . (\boldsymbol{p} \times \hat{z}) + \frac{\Delta}{2} \hat{\boldsymbol{\sigma}} . \boldsymbol{m}, \tag{2.20}$$

where v_F is the Fermi velocity, $\boldsymbol{\sigma}$ is the spin Pauli operator, Δ is the exchange interaction, and $\boldsymbol{m}$ is the magnetization unit vector. The eigenenergy yield as,

$$\epsilon_k = s\sqrt{\left(vk_x + \frac{\Delta}{2}m_y\right)^2 + \left(vk_y - \frac{\Delta}{2}m_x\right)^2 + \frac{\Delta^2}{4}m_z^2}, \tag{2.21}$$

As shown in (2.21), when the magnetization lies in the in-plane direction, the Dirac cone will be shifted in the $k_{x,y}$ direction, whereas it will open a gap at the Dirac point when the magnetization lies out-of-plane, causing the Dirac fermions to be massive [90,91]. In the context of SOT, the damping-like (DL) torque and field-like (FL) torque are expressed as [36,92],

$$\boldsymbol{T} = T_{FL}\boldsymbol{m} \times \boldsymbol{\sigma} + T_{DL}m_z\boldsymbol{m} \times (\hat{z} \times \boldsymbol{\sigma}), \tag{2.22}$$

where the field-like torque term arises from the conventional Rashba-Edelstein effect (REE), while the damping-like torque term arises from the intrinsic contribution, which is proportional to m_z. One can see that in (2.22), the torque will vanish when the magnetization lies in-plane, which differs drastically to the damping-like torque in LLG.

2.2.6 Advancement in Topological Insulator for Spintronics

The concept of a 3D topological insulators (TIs) was first theoretically predicted by Fu, Kane, and Mele in 2007 [70]. In 2014, Fan *et. al* first experimentally demonstrated SOT magnetization switching in Cr-doped TI heterostructure, Cr-$(Bi_xSb_{1-x})Te3/(Bi_xSb_{1-x})_2Te_3$ at 1.9 K [93]. Subsequently, Mellnik *et al.* have reported a high generation of SOT in room temperature, using TI bilayer structure, Bi_2Se_3 / $Ni_{0.8}Fe_{0.2}$ [94]. Later in 2015, Wang *et. al* performed temperature dependent study in a Bi_2Se_3/CoFeB bilayer heterostructure to show that the topological surface state is dominant in the generation of SOT at low temperature [95]. Shortly after, the manifestation of SOT from TIs was demonstrated in various TI/FM heterostructures, using different characterization methods such as second harmonic technique, ST-FMR, and hysteresis loop shift [96–100]. One significant advancement to this field of study was presented by Khang *et. al* in 2018, where they reported an exceptionally large SOT efficiency of 52, in a sputtered $Bi_{0.9}Sb_{0.1}/Mn_{0.45}Ga_{0.55}$ bilayer heterostructure [101]. This efficiency is several orders of magnitude greater than conventional heavy metals (HMs).

Extensive research has been carried out in recent years to further improve the SOT efficiency, and reducing the power consumption for SOT magnetization switching. Although

various TIs systems has been proposed, there exists a large discrepancy in the reported values of SOT efficiency in TIs. This SOT efficiency ranges drastically from 0.1 to several hundred, depending on the fabrication technique and characterization methods. In addition, the mechanism of the spin generation in TIs has remains elusive. There is still a dispute in the origin of SOT between bulk and surface state, as it is difficult to disentangle between these two factors [102].

One possible reason for this debate may arise from the high diffusivity of Bismuth and chalcogens. This attribute can potentially create a magnetic dead layer in the ferromagnetic material, thereby degrading the quality of the interface between the TIs and FM. As such, researchers have incorporated a nonmagnetic insertion layer between the TI and FM to preserve the interface. However, the introduction of an additional insertion layer between the TI and FM may influence the coupling between the spin polarization of TI and FM, possibly leading to a reduction in SOT [103]. Therefore, it is important to choose an appropriate insertion layer to prevent any disturbance in the topological surface state of the TIs, and also improve the crystallinity of the TIs, which can potentially result in the enhancement of SOT. In this thesis, we have conducted comprehensive investigations on the influence of different insertion layers on SOT. These findings will be thoroughly discussed in Chapter 5 of the thesis.

References

[1] J. Fujita and H. Miyazawa, *Spin-Orbit Coupling in Heavy Nuclei*, Prog. Theor. Phys. **17**, 366 (1957).

[2] S. Kim et al., *Giant Orbital Anisotropy with Strong Spin–Orbit Coupling Established at the Pseudomorphic Interface of the Co/Pd Superlattice*, Adv. Sci. **9**, 2201749 (2022).

[3] A. Soumyanarayanan, N. Reyren, A. Fert, and C. Panagopoulos, *Emergent Phenomena Induced by Spin–Orbit Coupling at Surfaces and Interfaces*, Nature **539**, 509 (2016).

[4] V. Galitski and I. B. Spielman, *Spin–Orbit Coupling in Quantum Gases*, Nature **494**, 49 (2013).

[5] M. Blume, R. E. Watson, and R. E. Peierls, *Theory of Spin-Orbit Coupling in Atoms I. Derivation of the Spin-Orbit Coupling Constant*, Proc. R. Soc. London. Ser. A. Math. Phys. Sci. **270**, 127 (1997).

[6] H. Mathur, *Thomas Precession, Spin-Orbit Interaction, and Berry's Phase*, Phys. Rev. Lett. **67**, 3325 (1991).

[7] M. I. Dyakonov and V. I. Perel, *Current-Induced Spin Orientation of Electrons in Semiconductors*, Phys. Lett. A **35**, 459 (1971).

[8] M. I. D'Yakonov and V. I. Perel', *Possibility of Orienting Electron Spins with Current*, ZhETF Pisma Redaktsiiu **13**, 657 (1971).

[9] J. E. Hirsch, *Spin Hall Effect*, Phys. Rev. Lett. **83**, 1834 (1999).

[10] J. Sinova, S. O. Valenzuela, J. Wunderlich, C. H. Back, and T. Jungwirth, *Spin Hall Effects*, Rev. Mod. Phys. **87**, 1213 (2015).

[11] S. Zhang, *Spin Hall Effect in the Presence of Spin Diffusion*, Phys. Rev. Lett. **85**, 393 (2000).

[12] T. Jungwirth, J. Wunderlich, and K. Olejník, *Spin Hall Effect Devices*, Nat. Mater. **11**, 382 (2012).

[13] T. Kimura, Y. Otani, T. Sato, S. Takahashi, and S. Maekawa, *Room-Temperature Reversible Spin Hall Effect*, Phys. Rev. Lett. **98**, 156601 (2007).

[14] B. F. Miao, S. Y. Huang, D. Qu, and C. L. Chien, *Inverse Spin Hall Effect in a Ferromagnetic Metal*, Phys. Rev. Lett. **111**, 66602 (2013).

[15] X. R. Wang, *Anomalous Spin Hall and Inverse Spin Hall Effects in Magnetic Systems*, Commun. Phys. **4**, 55 (2021).

[16] A. Manchon and S. Zhang, *Theory of Spin Torque Due to Spin-Orbit Coupling*, Phys.

Rev. B **79**, 94422 (2009).

[17] W. Wang et al., *Unconventional Spin Currents Generated by the Spin-Orbit Precession Effect in Perpendicularly Magnetized $\mathrm{Co}\text{\ensuremath{-}}\mathrm{Tb}$ Ferrimagnetic System*, Phys. Rev. Appl. **17**, 34026 (2022).

[18] A. Davidson, V. P. Amin, W. S. Aljuaid, P. M. Haney, and X. Fan, *Perspectives of Electrically Generated Spin Currents in Ferromagnetic Materials*, Phys. Lett. A **384**, 126228 (2020).

[19] P. Yang et al., *Enhancement of the Spin–Orbit Torque Efficiency in W/Cu/CoFeB Heterostructures via Interface Engineering*, Appl. Phys. Lett. **117**, 82409 (2020).

[20] J. Bokor, *Enhancement of the Spin Hall Effect in Heavy Metal Bilayers*, in (2016).

[21] *Hal-01579001v1*.

[22] B. Coester, G. D. H. Wong, Z. Xu, J. Tang, W. L. Gan, and W. S. Lew, *Enhanced Spin Hall Conductivity in Tungsten-Copper Alloys*, J. Magn. Magn. Mater. **523**, 167545 (2021).

[23] O. A. Santos, E. F. Silva, M. Gamino, J. B. S. Mendes, S. M. Rezende, and A. Azevedo, *Investigation of Large Enhancement of Spin Hall Angle in Heterostructures of Ag Nanoparticles Randomly Grown in Pt*, AIP Adv. **9**, 35025 (2019).

[24] J.-Y. Kim, D.-S. Han, M. Vafaee, S. Jaiswal, K. Lee, G. Jakob, and M. Kläui, *Enhancement of Spin Hall Conductivity in W–Ta Alloy*, Appl. Phys. Lett. **117**, 142403 (2020).

[25] T. Ng, Y. Luo, J. Yuan, Y. Wu, H. Yang, and L. Shen, *Origin and Enhancement of the Spin Hall Angle in the Weyl Semimetals LaAlSi and LaAlGe*, Phys. Rev. B **104**, 14412 (2021).

[26] N. F. Mott and N. H. D. Bohr, *The Scattering of Fast Electrons by Atomic Nuclei*, Proc. R. Soc. London. Ser. A, Contain. Pap. a Math. Phys. Character **124**, 425 (1997).

[27] T. Ziman, B. Gu, and S. Maekawa, *Skew Scattering from Correlated Systems Impurities and Collective Excitations in the Spin Hall Effect*, J. Phys. Soc. Japan **86**, 110051 (2017).

[28] H. Ishizuka and N. Nagaosa, *Large Anomalous Hall Effect and Spin Hall Effect by Spin-Cluster Scattering in the Strong-Coupling Limit*, Phys. Rev. B **103**, 235148 (2021).

[29] M. M. Glazov and L. E. Golub, *Skew Scattering and Side Jump Drive Exciton Valley Hall Effect in Two-Dimensional Crystals.*, Phys. Rev. Lett. **125**, 157403 (2020).

[30] J. Smit, *The Spontaneous Hall Effect in Ferromagnetics I*, Physica **21**, 877 (1955).

[31] J. Smit, *The Spontaneous Hall Effect in Ferromagnetics II*, Physica **24**, 39 (1958).

[32] L. Berger, *Side-Jump Mechanism for the Hall Effect of Ferromagnets*, Phys. Rev. B **2**, 4559 (1970).

[33] F. Sousa, G. Tatara, and A. Ferreira, *Skew-Scattering-Induced Giant Antidamping Spin-Orbit Torques: Collinear and out-of-Plane Edelstein Effects at Two-Dimensional Material/Ferromagnet Interfaces*, Phys. Rev. Res. **2**, 43401 (2020).

[34] U. Shashank et al., *Disentanglement of Intrinsic and Extrinsic Side-Jump Scattering Induced Spin Hall Effect in N-Implanted Pt*, Phys. Rev. B **107**, 64402 (2023).

[35] J. Sinova, S. O. Valenzuela, J. Wunderlich, C. H. Back, and T. Jungwirth, *Spin Hall Effects*, Rev. Mod. Phys. **87**, 1213 (2015).

[36] A. Manchon, J. Železný, I. M. Miron, T. Jungwirth, J. Sinova, A. Thiaville, K. Garello, and P. Gambardella, *Current-Induced Spin-Orbit Torques in Ferromagnetic and Antiferromagnetic Systems*, Rev. Mod. Phys. **91**, 35004 (2019).

[37] Y. Wang, P. Deorani, X. Qiu, J. H. Kwon, and H. Yang, *Determination of Intrinsic Spin Hall Angle in Pt*, Appl. Phys. Lett. **105**, (2014).

[38] H. Y. Poh, C. C. I. Ang, W. L. Gan, G. J. Lim, and W. S. Lew, *Direct Spin Accumulation Quantification in Ferromagnetic Heterostructures Using DC Bias Harmonic Hall Measurement*, Phys. Rev. B **104**, 224416 (2021).

[39] T. Fache, J. C. Rojas-Sanchez, L. Badie, S. Mangin, and S. Petit-Watelot, *Determination of Spin Hall Angle, Spin Mixing Conductance, and Spin Diffusion Length in CoFeB/Ir for Spin-Orbitronic Devices*, Phys. Rev. B **102**, 64425 (2020).

[40] J. T. Brangham, K.-Y. Meng, A. S. Yang, J. C. Gallagher, B. D. Esser, S. P. White, S. Yu, D. W. McComb, P. C. Hammel, and F. Yang, *Thickness Dependence of Spin Hall Angle of Au Grown on Y3Fe5O12 Epitaxial Films*, Phys. Rev. B **94**, 54418 (2016).

[41] K. Sriram, J. Pala, B. Paikaray, A. Haldar, and C. Murapaka, *Effect of Seed Layer Thickness on the Ta Crystalline Phase and Spin Hall Angle*, Nanoscale **13**, 19985 (2021).

[42] R. Bansal, G. Nirala, A. Kumar, S. Chaudhary, and P. K. Muduli, *Large Spin Hall Angle in β-W Thin Films Grown on CoFeB without Oxygen Plasma*, SPIN **08**, 1850018 (2018).

[43] W. Skowroński, Ł. Karwacki, S. Ziętek, J. Kanak, S. Łazarski, K. Grochot, T. Stobiecki, P. Kuświk, F. Stobiecki, and J. Barnaś, *Determination of Spin Hall Angle in Heavy-Metal/Co-Fe-B-Based Heterostructures with Interfacial Spin-Orbit Fields*, Phys. Rev. Appl. **11**, 24039 (2019).

[44] M. Morota, K. Ohnishi, T. Kimura, and Y. Otani, *Spin Hall Effect in Molybdenum Wires*,

J. Appl. Phys. **105**, 07C712 (2009).

[45] O. Mosendz, J. E. Pearson, F. Y. Fradin, G. E. W. Bauer, S. D. Bader, and A. Hoffmann, *Quantifying Spin Hall Angles from Spin Pumping: Experiments and Theory*, Phys. Rev. Lett. **104**, 46601 (2010).

[46] Q. Xie et al., *Rashba–Edelstein Effect in the h-BN Van Der Waals Interface for Magnetization Switching*, Adv. Mater. **34**, 2109449 (2022).

[47] A. El Hamdi, J.-Y. Chauleau, M. Boselli, C. Thibault, C. Gorini, A. Smogunov, C. Barreteau, S. Gariglio, J.-M. Triscone, and M. Viret, *Observation of the Orbital Inverse Rashba–Edelstein Effect*, Nat. Phys. (2023).

[48] T. S. Ghiasi, A. A. Kaverzin, P. J. Blah, and B. J. van Wees, *Charge-to-Spin Conversion by the Rashba–Edelstein Effect in Two-Dimensional van Der Waals Heterostructures up to Room Temperature*, Nano Lett. **19**, 5959 (2019).

[49] G. Bihlmayer, O. Rader, and R. Winkler, *Focus on the Rashba Effect*, New J. Phys. **17**, 50202 (2015).

[50] C. Liu, H. Gao, Y. Li, K. Wang, L. A. Burton, and W. Ren, *Manipulation of the Rashba Effect in Layered Tellurides MTe (M = Ge, Sn, Pb)*, J. Mater. Chem. C **8**, 5143 (2020).

[51] Semion Saikin, *A Drift-Diffusion Model for Spin-Polarized Transport in a Two-Dimensional Non-Degenerate Electron Gas Controlled by Spin–Orbit Interaction*, J. Phys. Condens. Matter **16**, 5071 (2004).

[52] G. Bihlmayer, P. Noël, D. V Vyalikh, E. V Chulkov, and A. Manchon, *Rashba-like Physics in Condensed Matter*, Nat. Rev. Phys. **4**, 642 (2022).

[53] L. LANDAU and E. LIFSHITZ, *On the Theory of the Dispersion of Magnetic Permeability in Ferromagnetic Bodies*, Perspect. Theor. Phys. **169**, 51 (1992).

[54] T. Ando, Y. Matsumoto, and Y. Uemura, *Theory of Hall Effect in a Two-Dimensional Electron System*, J. Phys. Soc. Japan **39**, 279 (1975).

[55] K. V. Klitzing, G. Dorda, and M. Pepper, *New Method for High-Accuracy Determination of the Fine-Structure Constant Based on Quantized Hall Resistance*, Phys. Rev. Lett. **45**, 494 (1980).

[56] R. B. Laughlin, *Quantized Hall Conductivity in Two Dimensions*, Phys. Rev. B **23**, 5632 (1981).

[57] D. J. Thouless, M. Kohmoto, M. P. Nightingale, and M. den Nijs, *Quantized Hall Conductance in a Two-Dimensional Periodic Potential*, Phys. Rev. Lett. **49**, 405 (1982).

[58] K. von Klitzing, *The Quantized Hall Effect*, Rev. Mod. Phys. **58**, 519 (1986).

[59] K. von Klitzing, *Quantum Hall Effect: Discovery and Application*, Annu. Rev. Condens. Matter Phys. **8**, 13 (2017).

[60] K. von Klitzing, *Developments in the Quantum Hall Effect*, Philos. Trans. R. Soc. A Math. Phys. Eng. Sci. **363**, 2203 (2005).

[61] S. Li, C. M. Wang, Z. Z. Du, F. Qin, H.-Z. Lu, and X. C. Xie, *3D Quantum Hall Effects and Nonlinear Hall Effect*, Npj Quantum Mater. **6**, 96 (2021).

[62] D. R. Cooper et al., *Experimental Review of Graphene*, ISRN Condens. Matter Phys. **2012**, 1 (2012).

[63] K. von Klitzing et al., *40 Years of the Quantum Hall Effect*, Nat. Rev. Phys. **2**, 397 (2020).

[64] Y. Zhang, Y.-W. Tan, H. L. Stormer, and P. Kim, *Experimental Observation of the Quantum Hall Effect and Berry's Phase in Graphene*, Nature **438**, 201 (2005).

[65] J. Ge, Y. Liu, J. Li, H. Li, T. Luo, Y. Wu, Y. Xu, and J. Wang, *High-Chern-Number and High-Temperature Quantum Hall Effect without Landau Levels*, Natl. Sci. Rev. **7**, 1280 (2020).

[66] M. Dc et al., *Room-Temperature High Spin–Orbit Torque Due to Quantum Confinement in Sputtered BixSe(1–x) Films*, Nat. Mater. **17**, 800 (2018).

[67] C. D. Spataru and F. Léonard, *Fermi-Level Pinning, Charge Transfer, and Relaxation of Spin-Momentum Locking at Metal Contacts to Topological Insulators*, Phys. Rev. B - Condens. Matter Mater. Phys. **90**, 3 (2014).

[68] C. L. Kane and E. J. Mele, *Quantum Spin Hall Effect in Graphene*, Phys. Rev. Lett. **95**, 226801 (2005).

[69] C.-Z. Chang et al., *Experimental Observation of the Quantum Anomalous Hall Effect in a Magnetic Topological Insulator.*, Science **340**, 167 (2013).

[70] L. Fu, C. L. Kane, and E. J. Mele, *Topological Insulators in Three Dimensions*, Phys. Rev. Lett. **98**, 106803 (2007).

[71] D. Hsieh, D. Qian, L. Wray, Y. Xia, Y. S. Hor, R. J. Cava, and M. Z. Hasan, *A Topological Dirac Insulator in a Quantum Spin Hall Phase*, Nature **452**, 970 (2008).

[72] Y. Xia et al., *Observation of a Large-Gap Topological-Insulator Class with a Single Dirac Cone on the Surface*, Nat. Phys. **5**, 398 (2009).

[73] T. Sato, K. Segawa, K. Kosaka, S. Souma, K. Nakayama, K. Eto, T. Minami, Y. Ando, and T. Takahashi, *Unexpected Mass Acquisition of Dirac Fermions at the Quantum Phase Transition of a Topological Insulator*, Nat. Phys. **7**, 840 (2011).

[74] J. H. Dil, *Spin- and Angle-Resolved Photoemission on Topological Materials*, Electron. Struct. **1**, 23001 (2019).

[75] H. Y. Poh, C. C. I. Ang, G. J. Lim, T. L. Jin, S. H. Lee, E. K. Koh, F. Poh, and W. S. Lew, *Crystallinity Control of the Topological-Insulator Surface Bi85Sb15 (012) via Interfacial Engineering for Enhanced Spin-Orbit Torque*, Phys. Rev. Appl. **19**, 1 (2023).

[76] E. Longo et al., *Large Spin-to-Charge Conversion at Room Temperature in Extended Epitaxial Sb2Te3 Topological Insulator Chemically Grown on Silicon*, Adv. Funct. Mater. **32**, 2109361 (2022).

[77] J. Han and L. Liu, *Topological Insulators for Efficient Spin–Orbit Torques*, APL Mater. **9**, 60901 (2021).

[78] N. H. D. Khang, S. Nakano, T. Shirokura, Y. Miyamoto, and P. N. Hai, *Ultralow Power Spin–Orbit Torque Magnetization Switching Induced by a Non-Epitaxial Topological Insulator on Si Substrates*, Sci. Rep. **10**, 1 (2020).

[79] Z. Xu, G. D. H. Wong, J. Tang, E. Liu, W. Gan, F. Xu, and W. S. Lew, *Large Spin Hall Angle Enhanced by Nitrogen Incorporation in Pt Films*, Appl. Phys. Lett. **118**, 62406 (2021).

[80] S. Woo, M. Mann, A. J. Tan, L. Caretta, and G. S. D. Beach, *Enhanced Spin-Orbit Torques in Pt / Co / Ta Heterostructures Enhanced Spin-Orbit Torques in Pt / Co / Ta Heterostructures*, Appl. Phys. Lett. **105**, 212404 (2016).

[81] B. Feng, J. Weng, B. C. Yang, S. X. Qu, and X. D. Zhang, *Characterization of Surface Oxide Films on Titanium and Bioactivity*, Biomaterials **24**, 4663 (2003).

[82] G. D. Hwee Wong et al., *Strain-Mediated Spin–Orbit Torque Enhancement in Pt/Co on Flexible Substrate*, ACS Nano **15**, 8319 (2021).

[83] S. Woo, M. Mann, A. Tan, L. Carreta, and G. Beach, *Characterization of Spin-Orbit Torques in Pt/Co/Ta Structures*, 2015 IEEE Int. Magn. Conf. 1 (2015).

[84] Y. Tserkovnyak, A. Brataas, and G. E. W. Bauer, *Enhanced Gilbert Damping in Thin Ferromagnetic Films*, Phys. Rev. Lett. **88**, 117601 (2002).

[85] Y. Tserkovnyak, D. A. Pesin, and D. Loss, *Spin and Orbital Magnetic Response on the Surface of a Topological Insulator*, Phys. Rev. B **91**, 41121 (2015).

[86] Y. Tserkovnyak, A. Brataas, and G. E. W. Bauer, *Spin Pumping and Magnetization Dynamics in Metallic Multilayers*, Phys. Rev. B **66**, 224403 (2002).

[87] K. Fujiwara, Y. Fukuma, J. Matsuno, H. Idzuchi, Y. Niimi, Y. Otani, and H. Takagi, *5d Iridium Oxide as a Material for Spin-Current Detection*, Nat. Commun. **4**, 2893 (2013).

[88] S. Fukami, T. Anekawa, C. Zhang, and H. Ohno, *A Spin–Orbit Torque Switching Scheme with Collinear Magnetic Easy Axis and Current Configuration*, Nat. Nanotechnol. **11**, 621 (2016).

[89] J. Fujimoto and H. Kohno, *Transport Properties of Dirac Ferromagnet*, Phys. Rev. B **90**, 214418 (2014).

[90] F. Zhang, C. L. Kane, and E. J. Mele, *Surface State Magnetization and Chiral Edge States on Topological Insulators*, Phys. Rev. Lett. **110**, 1 (2013).

[91] A. Sakai and H. Kohno, *Spin Torques and Charge Transport on the Surface of Topological Insulator*, Phys. Rev. B - Condens. Matter Mater. Phys. **89**, 1 (2014).

[92] P. B. Ndiaye, C. A. Akosa, M. H. Fischer, A. Vaezi, E. A. Kim, and A. Manchon, *Dirac Spin-Orbit Torques and Charge Pumping at the Surface of Topological Insulators*, Phys. Rev. B **96**, 014408 (2017).

[93] Y. Fan et al., *Magnetization Switching through Giant Spin-Orbit Torque in a Magnetically Doped Topological Insulator Heterostructure.*, Nat. Mater. **13**, 699 (2014).

[94] A. R. Mellnik et al., *Spin-Transfer Torque Generated by a Topological Insulator*, Nature **511**, 449 (2014).

[95] Y. Wang, P. Deorani, K. Banerjee, N. Koirala, M. Brahlek, S. Oh, and H. Yang, *Topological Surface States Originated Spin-Orbit Torques in ${\mathrm{Bi}}_{2}{\mathrm{Se}}_{3}$*, Phys. Rev. Lett. **114**, 257202 (2015).

[96] J. Han, A. Richardella, S. A. Siddiqui, J. Finley, N. Samarth, and L. Liu, *Room-Temperature Spin-Orbit Torque Switching Induced by a Topological Insulator*, Phys. Rev. Lett. **119**, 77702 (2017).

[97] Q. Shao, H. Wu, Q. Pan, P. Zhang, L. Pan, K. Wong, X. Che, and K. L. Wang, *Room Temperature Highly Efficient Topological Insulator/Mo/CoFeB Spin-Orbit Torque Memory with Perpendicular Magnetic Anisotropy*, in *2018 IEEE International Electron Devices Meeting (IEDM)* (2018), pp. 36.3.1-36.3.4.

[98] X. Che et al., *Strongly Surface State Carrier-Dependent Spin–Orbit Torque in Magnetic Topological Insulators*, Adv. Mater. **32**, 1907661 (2020).

[99] H. Wu et al., *Spin-Orbit Torque Switching of a Nearly Compensated Ferrimagnet by Topological Surface States*, Adv. Mater. **31**, 1901681 (2019).

[100] H. Y. Poh, C. C. I. Ang, G. J. Lim, T. L. Jin, S. H. Lee, E. K. Koh, F. Poh, and W. S. Lew, *Crystallinity Control of the Topological-Insulator Surface*

${\mathrm{Bi}}_{85}{\mathrm{Sb}}_{15}(012)$ via Interfacial Engineering for Enhanced Spin-Orbit Torque, Phys. Rev. Appl. **19**, 34012 (2023).

[101] N. H. D. Khang, Y. Ueda, and P. N. Hai, *A Conductive Topological Insulator with Large Spin Hall Effect for Ultralow Power Spin–Orbit Torque Switching*, Nat. Mater. **17**, 808 (2018).

[102] H. Wang, J. Kally, C. Şahin, T. Liu, W. Yanez, E. J. Kamp, A. Richardella, M. Wu, M. E. Flatté, and N. Samarth, *Fermi Level Dependent Spin Pumping from a Magnetic Insulator into a Topological Insulator*, Phys. Rev. Res. **1**, 12014 (2019).

[103] F. Bonell, M. Goto, G. Sauthier, J. F. Sierra, A. I. Figueroa, M. V Costache, S. Miwa, Y. Suzuki, and S. O. Valenzuela, *Control of Spin–Orbit Torques by Interface Engineering in Topological Insulator Heterostructures*, Nano Lett. **20**, 5893 (2020).

Chapter 3 Experimental Techniques

In this chapter, details of the fabrication process and characterization techniques employed in this work are discussed. All thin film depositions are performed using magnetron sputtering. Lithography process is used to pattern the devices for electrical measurement. Harmonic Hall technique is adopted to quantify the spin-orbit torque of the spintronics heterostructure. Here, I also introduce my work, where I quantify the spin-orbit torque directly in a blanket film without any lithography processes.

3.1 Device Fabrication

In this section, the Hall cross devices for the magnetic heterostructure used in the work of Chapters 4, 5 and 6 are described. This fabrication process involved three main procedures: (i) Deposition, (ii) Lithography (iii) Etching process.

The fabrication process begins with a thermally oxidized silicon wafer as a substrate. The wafer is cleaved into a 1 cm by 1 cm dimension to facilitate deposition and lithography. Before further processing, the wafers undergo a cleaning procedure to remove any impurities or foreign substances that may interfere with the subsequent processing steps. This cleaning step is crucial for ensuring the quality of the final product. The wafers were thoroughly cleaned using a multi-step process that involved submerging them in an isopropanol bath, followed by an acetone bath in an ultrasonic cleaner. After rinsing with isopropanol, they were dried using a dry nitrogen jet to ensure that no residue was left on the surface. The fabrication process adopted in this work involves two different methods, depending on the requirements of the samples:

(i) Lithography → Deposition → Lift-off
(ii) Deposition → Lithography → Etching

Upon completion of the Hall-cross devices fabrications, contact pads are then added using the (lithography → Deposition →Lift-off) procedure. This step is crucial for enabling the electrical measurement of the devices.

The following subsections will provide in-depth details on the various steps involved in the fabrication process, including the cleaning procedure, lithography, deposition, lift-off, and contact pad fabrication. Each step will be explained in detail to give a comprehensive understanding of the fabrication process used in this work.

3.1.2 Magnetron Sputtering Deposition

Magnetron sputtering is a form of physical vapour deposition technique, a widely utilized thin film deposition technique employed across various scientific disciplines and industries [1–3]. This method enables the production of high-quality thin films with well-controlled thickness, composition, and uniformity, making them particularly suitable for applications in the fields of electronics, optics, and materials science.

The schematic and working principle of magnetron sputtering is shown in Figure 3.1. The working principle behind sputtering involves the generation of plasma in a vacuum chamber, where positively charged ions collide with a target material, ejecting its atoms in the process. These sputtered atoms then travel through the chamber and deposit onto a substrate, forming a thin film [1,4,5].

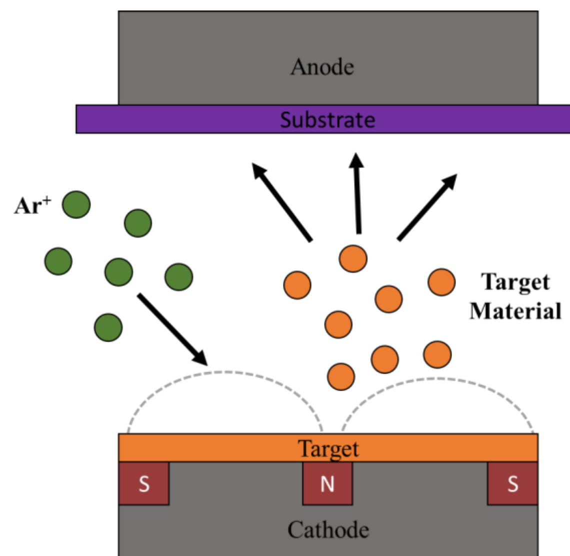

Figure 3.1: Schematic of magnetron sputtering deposition process.

The process begins by placing the target material and substrate inside a vacuum chamber under a low-pressure condition, typically in the order of 10^{-7} to 10^{-8} Torr. This

condition minimizes the collisions between sputtered atoms and other background gas molecules, ensuring high-quality film deposition. Typically, argon gas is utilized to create the plasma to bombard the targets due to its relatively high atomic mass and being inserted. This argon plasma is ignited by applying high voltage to the target. These argon ions within the plasma are propelled toward the target, where they collide with and knock out the surface atoms of the target [6]. These released atoms then travel as gaseous particles toward the substrate. The deposition is therefore achieved by landing these particles on the substrate, reforming as a solid thins films.

Usually, metallic targets utilize DC power, while insulating targets require radio frequency (RF) power. If a DC power is employed on an insulating target, it causes the accumulation of a positive charge, which hinders the attraction of Argon ions for target bombardment. Charge accumulation is undesirable since it can lead to arcing, which disrupts the sputtering process or damages the target. On the other hand, RF power discharges the accumulated charge during half its cycle, thus overcoming the charge accumulation problem. RF sputtering has additional benefits, such as a more uniform use of the sputtering target due to the diffused plasma and resolving the disappearing anode problem that occurs as dielectric coats the anode, disrupting the electric fields. However, RF sputtering is generally more expensive and necessitates higher voltage and more costly power supplies, and it has much slower sputtering rates compared to DC sputtering.

The overview of the sputtering systems in the laboratory is shown in Fig. 3.1. Here, I utilize two custom-made AJA ATC-Orion 8 UHV sputtering systems, where I can deposit sixteen different types of materials on our substrate without breaking the vacuum. The deposition thickness of the thin film is determined based on a calibrated sputtering rate rather than relying on *in situ* thickness monitoring. This approach utilizes nominal values to estimate the deposited film's thickness during the sputtering process. The calibration process involves depositing materials for an extended duration on a blanket sample with a small drop of photoresist applied. After the deposition, a lift-off process is conducted to remove the photoresist, leaving behind the deposited material. An atomic force microscope (AFM) is then utilized to measure the thickness of the deposited material accurately, providing a basis for calibration of the sputtering rates.

Fig. 3.1: (Top) Image of two customized-made AJA ATC-Orion 9 UHV sputtering system (Bottom) Two x 8 different targets in the main chamber

3.1.3 Electron Beam Lithography

Electron beam lithography (EBL) is a high-resolution patterning technique capable of achieving nanometer-scale regime [7–9]. Here, we use the Raith eLINE EBL system, as shown in Fig. 3.2, to pattern our devices. The overall lithography process encompasses three key steps: spin coating, exposure, and developing. Before the patterning process, a negative resist is spin-

coated on the wafer at a rotation speed of 6000 rpm for 60 seconds, resulting in a thin resist layer. Following this, the spin-coated wafer is subjected to a soft-bake at 115°C for 90 seconds. This is to solidify the photoresist in preparation for exposure.

Fig. 3.2: Image of an Electron Beam Lithograph Setup (Raith eLine EBL)

During the fabrication of Hall-cross devices on deposited magnetic multilayer samples, negative resist, MaN 2401 is utilized to protect the exposed region during the subsequent etching process. Within the EBL system, multiple alignments are required to ensure the proper focusing of the electron beam and to guide the path of the beam during exposure. Apart from patterning, the EBL also has the function of scanning electron microscope (SEM) to view the surface of the samples in a nanometer regime, as shown in Fig. 3.3. After the exposure process, the wafer is developed using ma-D 532 developer, with de-ionized water to halt the developing process. It is crucial to monitor the developing time, as overly long or short duration can lead to undesirably wide pattern or unwanted residual resist, respectively.

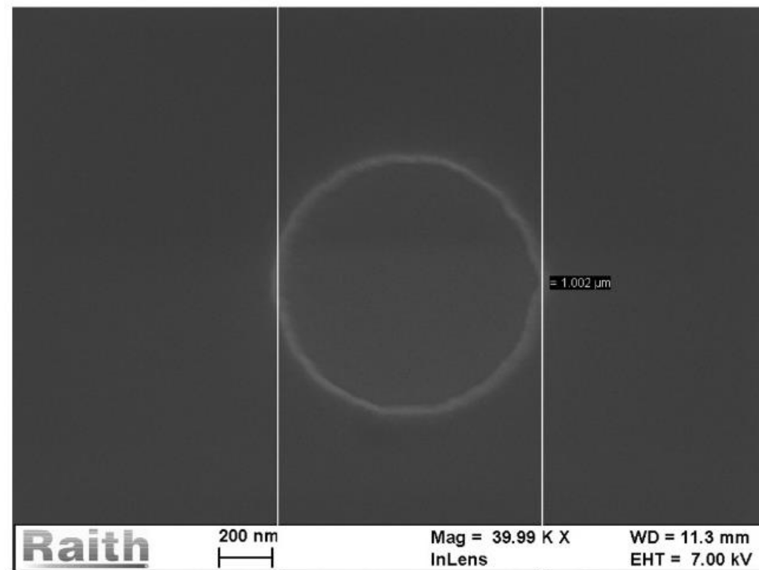

Fig. 3.3: SEM image of a 1 μm device

3.1.4 Ion Beam Etching

Ion Beam Etching (IBE) is a highly precise and versatile material removal technique employed in various applications across fields such as microelectronics, nanotechnology, and surface engineering [10,11]. This advanced method enables the controlled and selective etching of materials at the nanoscale, making it an indispensable tool in the fabrication of nanodevices.

The working principle of ion beam etching relies on the bombardment of a material surface with a directed beam of energetic ions, typically argon plasma. These high-energy ions interact with the target material, causing the ejection of surface atoms through processes such as sputtering, physical etching, or reactive ion etching. By controlling the ion beam incidence angle, it is possible to achieve highly accurate and reproducible etching profiles. Prior to the IBE process, a photoresist is applied to cover the region of interest where Hall-cross devices are located. This protective photoresist layer will prevent the Hall-cross structure from being etched away during the etching process.

In my work, I use the AJA ATC-2020-IM ion beam etching system as shown in Fig. 3.4. During the etching process, to minimize the redeposition of material, the stage is positioned at a 10° angle relative to the argon beam. This angled configuration helps reduce the likelihood of sputtered materials reattaching to the sample surface. Under the bombardment of ions, both

the sample and the sample stage experience significant heating, making water cooling essential. Despite the use of water cooling, the etching process is still divided into multiple segments (15 mins per segment), with intermediate pauses of 15 minutes, to allow the sample to cool down, ensuring optimal conditions for precise etching.

Fig. 3.4: Image of a ion-beam etching setup

3.2 Device Characterization Technique

In this section, we will explore the characterization technique employed to analyze our samples. The vibrating sample magnetometer (VSM) is utilized to determine the magnetic properties of our samples, while X-ray diffraction (XRD) is used to investigate the crystal structure of our samples.

3.2.1 Vibrating Sample Magnetometer

The VSM is a well-known technique employed to quantify the magnetic properties of a wide range of materials [12–15]. The VSM operates based on the principles of Faraday law,

where the sample with a magnetic moment is oscillated under a uniform magnetic field, thus causing the changed in magnetic flux, which results in the generation of electromotive force (EMF) [16–18]. This induced voltage is proportional to the magnetic moment of the materials, and this voltage is picked up by the pickup coils in the VSM.

In my experimental setup, I utilized the LakeShore 8604, as shown in Fig. 3.5. The system comprises of the sample holder, piezo-driven oscillator, electromagnet, and pickup coils. Prior to the measurement, the sample is securely attached to the sample holder rod using adhesive tape. The sample holder rode has the degree of freedom to rotate 360°, enabling the measurement of the sample easy and hard axis. The rod is positioned between two electromagnet poles, capable of generating a magnetic field of up to 2 T, depending on the pole gap distance. The piezo-driven oscillator vertically oscillates at 83 Hz during the measurement, while the electromagnet applies a preset sweeping magnetic field orthogonal to the oscillation. The pickup coil, which has been pre-calibrated with a reference Ni sphere, detects the induced voltage, thereby providing information about the magnetic moment of the sample.

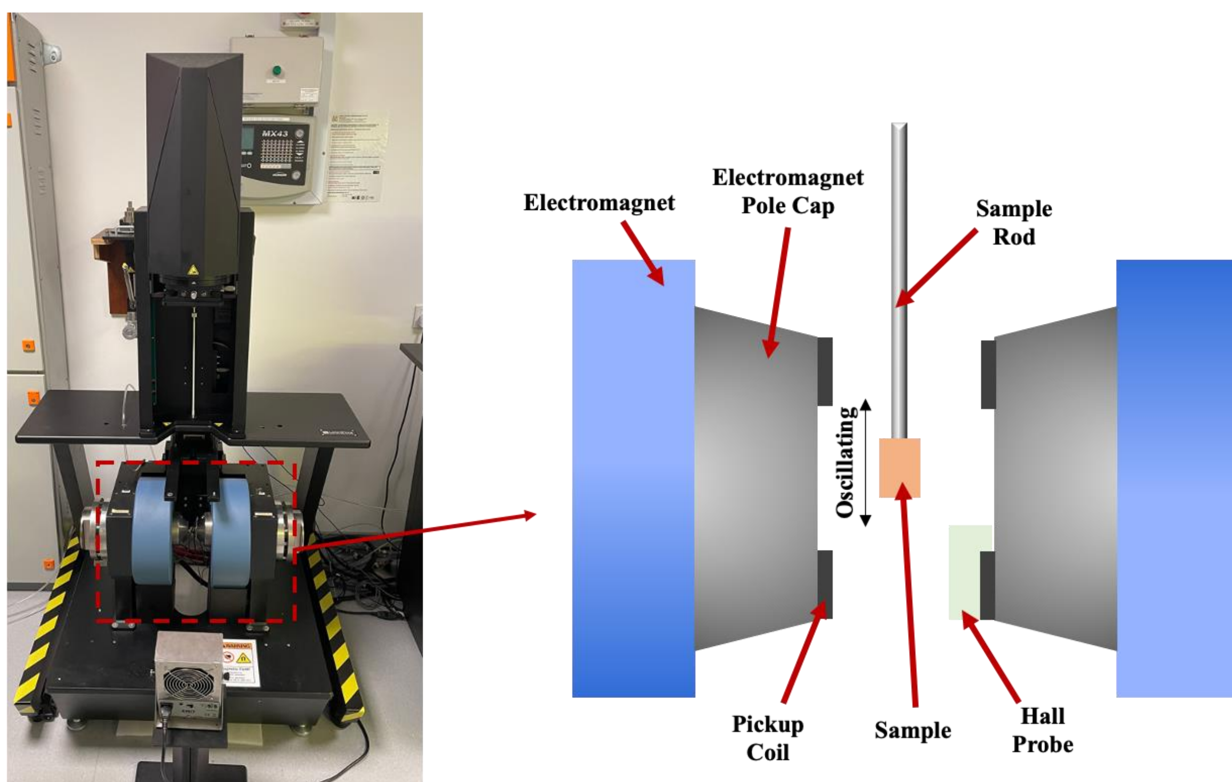

Fig. 3.5: (Left) Image of LakeShore 8604 VSM (Right) Zoom-in illustration of the electromagnet, pickup coil and sample mounted on the piezo-driven oscillator

3.2.2 X-Ray Diffraction

The XRD is a non-destructive technique to investigate the crystallographic structure of materials [19,20]. This technique provides information about the arrangement of atoms in a crystal lattice, phase composition, crystalline size, and other critical properties that influence the material performance in diverse applications.

The working principle of XRD is based on the interaction between emitted X-rays and the crystal lattice of the material [21–23]. When a monochromatic X-ray beam is incident upon a crystalline sample, the X-rays are scattered by the atoms or ions in the lattice. Constructive interference of the scattered X-rays occurs when the path difference between the X-ray scattered by different lattice planes satisfies Bragg's law [24,25],

$$n\lambda = 2d \sin\theta, \tag{3.0}$$

where n is an integer for the order of diffraction, λ is the wavelength of the X-ray beam, and θ is the angle between the X-ray beam and the diffraction plane. The schematic of the XRD setup and working principle is, as shown in Fig. 3.6. By measuring the intensity of the diffracted X-rays as a function of the diffraction angle (2θ), we can obtain a unique diffraction pattern, also known as an XRD pattern, which serves as a 'fingerprint' of the material crystal structure.

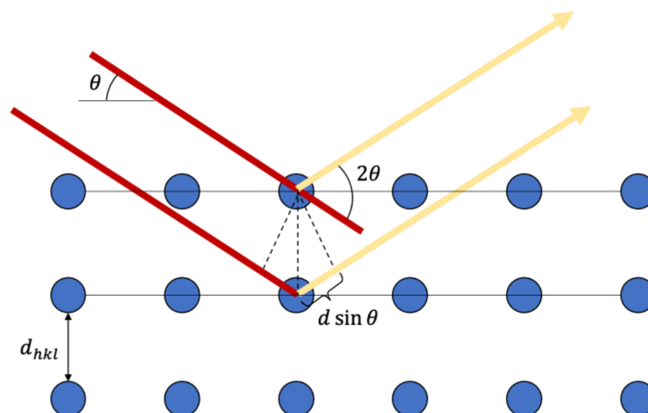

Fig. 3.6: Illustration of X-ray beam reflecting off the sample

3.3 Harmonic Hall Technique

The Harmonic Hall technique is a viable electrical technique to quantify spin-orbit torque in magnetic materials [26–31]. This technique is first adopted by M. Hayashi. *et. al* [28], where low-frequency alternating current (AC) is applied to the magnetic heterostructure. The applied current causes a perturbation in the magnetization, hence inducing a Hall voltage. This voltage is then detected and measured using a lock-in amplifier, providing valuable insights into the materials' spin-orbit torque properties. In this section, we will first discuss on the experimental setup implementing the Harmonic Hall technique. Following this, we will provide a detailed understanding and derivations of the harmonic Hall voltage.

3.3.1 Harmonics Hall Technique Setup

The setup for the harmonics Hall technique comprises of the following key equipment,

(i) Keithley 6221 AC/DC Sourcemeter
(ii) Signal Recovery 7265 DSP Lock-in Amplifier
(iii) Lakeshore EM4-HVA

In order to apply current and readout voltage from our Hall-cross devices in the harmonic Hall measurement, the Hall-cross device is wire-bonded to a customized chip carrier as shown in Fig. 3.7. The chip carrier, along with the device, is mounted onto a rotating stage situated between the electromagnets. This rotating stage allows the device to rotate from 0° to 360° in the azimuthal angle, with respect to the applied magnetic field. A Gaussmeter probe is placed near the chip carrier to measure the magnetic field generated by the electromagnet. Depending on the requirement of the experiment, additional permanent magnets can be mounted onto the setup orthogonal to the electromagnet direction ($\hat{y}, \hat{z}$).

MATLAB/LabView have been developed to establish communication with the above-mentioned equipment using GPIB cables. These scripts are designed to perform the harmonic Hall measurement by applying an AC current, sweeping the magnetic field as required by the experiment, and detecting the harmonic Hall voltage from the lock-in amplifier. Upon the measurement, the data will be fitted based on analytical modelling which will be discussed in the next subsection.

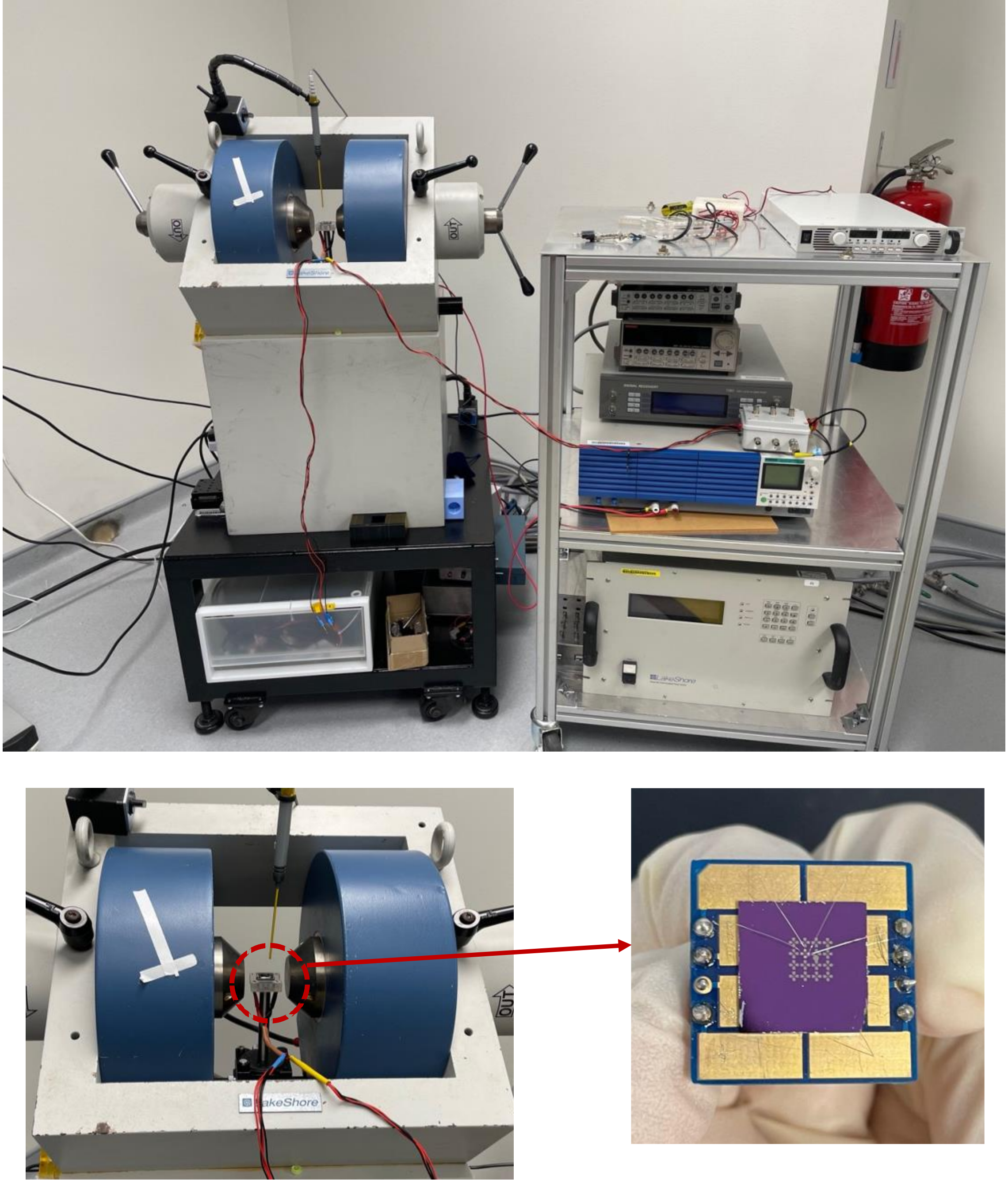

Fig. 3.7: (Top) Image of Harmonic Hall measurement setup Setup (Bottom) Zoom-in view between the pole gap and the wire-bonded device on a customized chip carrier

3.3.2 Derivation of Harmonic Hall Voltage

Starting off with the effect of current-induced spin torques, we introduce the Landau-Lifshitz -Gilbert equation, which is defined as [32,33],

$$\frac{d\vec{\boldsymbol{m}}}{dt} = -\gamma\vec{\boldsymbol{m}} \times \vec{\boldsymbol{H}}_{eff} + \alpha\vec{\boldsymbol{m}} \times \frac{d\vec{\boldsymbol{m}}}{dt} + \gamma H_{FL}\vec{\boldsymbol{m}} \times \hat{\boldsymbol{\sigma}} + \gamma H_{DL}\vec{\boldsymbol{m}} \times (\hat{\boldsymbol{\sigma}} \times \vec{\boldsymbol{m}}), \qquad (3.2)$$

where γ is the gyromagnetic ratio, $\vec{\boldsymbol{m}}$ is the magnetization vector, α is the Gilbert damping constant, $\vec{\boldsymbol{H}}_{eff}$ is the effective magnetic field. H_{FL} and H_{DL} are the field-like and damping-like field, respectively. The field-like torque causes a precession about the magnetization, $\Delta\phi$, while the damping-like torque produces an out-of-plane rotation of the magnetization layer, $\Delta\theta$. From those magnetic responses to the current, we can calculate how the voltage response accordingly. The harmonic Hall voltage typically contains contributions from the anomalous Hall effect (AHE), and the planar Hall effect [24,34]. Here, we define ΔR_A and ΔR_P as the changed in Hall resistance due to AHE and PHE, respectively. The Hall resistance, R_{xy} is express as,

$$R_{xy} = \frac{1}{2}\Delta R_A \cos\theta + \frac{1}{2}\Delta R_P \sin^2\theta \sin 2\phi, \tag{3.3}$$

where R_A and R_p are the anomalous Hall and planar Hall resistance, respectively, while θ and ϕ are the polar and azimuthal angle, respectively. Owning to the modulation introduced by the AC, θ and ϕ can be expressed as $\theta = \theta_0 + \Delta\theta$, and $\phi = \phi_0 + \Delta\phi$, respectively. In this harmonic Hall setup, small angle approximation is assumed, hence $\Delta\theta \ll 1$, and $\Delta\phi \ll 1$. Thus, we can expand Rxy= $\frac{1}{2}\Delta R_A \cos\theta + \frac{1}{2}\Delta R_P \sin^2\theta \sin 2\phi$, (3.3) as,

$$R_{xy} \approx \frac{1}{2}\Delta R_A(\cos\theta_0 - \Delta\theta\sin\theta_0) +$$

$$\frac{1}{2}\Delta R_P(\sin^2\theta_0 + \Delta\theta\sin 2\theta)(\sin 2\phi_0 + 2\Delta\phi\cos 2\phi), \tag{3.4}$$

The Hall voltage is the product between injected current and Hall resistance, $V_{xy} = IR_{xy}$. Here, given a sinusoidal current, $I = \Delta I \sin\omega t$, the current-induced effective field oscillates with the injected current. One should note that the frequency, ω, should be small to avoid any phase difference between the current and effective field oscillation. With the assistance of a lock-in amplifier, frequency mixing occurs, which yields,

$$V_{xy} = V_0 + V_\omega \sin\omega t + V_{2\omega}\cos 2\omega t, \tag{3.5}$$

where

From $Vxy= V_0 + V_\omega \sin \omega t + V_{2\omega} \cos 2\omega t,$ (3.5), the V_0, V_ω and $V_{2\omega}$ can be expressed as,

$$V_0 = \frac{1}{2}\Delta I \begin{bmatrix} \frac{1}{2}\Delta\theta(\Delta R_A \sin\theta_0 + \Delta R_P \sin 2\theta_0 \sin 2\phi_0) \\ +\frac{1}{2}(\Delta\phi\Delta R_P \sin^2\theta_0 \cos 2\phi_0) \end{bmatrix}, \quad (3.6)$$

$$V_\omega = \frac{1}{2}\Delta \mathrm{I}\ (\Delta R_A \cos\theta_0 + \Delta R_P \sin^2\theta_0 \sin 2\phi_0), \quad (3.7)$$

$$V_{2\omega} = -\frac{1}{2}\Delta I \begin{bmatrix} \frac{1}{2}\Delta\theta(\Delta R_A \sin\theta_0 + \Delta R_P \sin 2\theta_0 \sin 2\phi_0) \\ +\frac{1}{2}(\Delta\phi\Delta R_P \sin^2\theta_0 \cos 2\phi_0) \end{bmatrix}, \quad (3.8)$$

As can be seen in (3.6), (3.7), and (3.8), the damping-like field and field-like field are described in the harmonic Hall voltages.

In-plane Magnetic Anisotropy (IMA) System

In the case when the magnetic structure has an in-plane magnetic anisotropy, the energy of the system is given by [31,35],

$$E = \left(N_z M_s^2 - K_p\right)\sin^2\theta - M_s H_z \sin\theta - M_s H_x \cos\theta\cos\phi - M_s H_y \cos\theta \sin\phi, \quad (3.9)$$

where $H_{x,y,z}$ is the total effective magnetic field, M_s is the saturation magnetization, N_z is the demagnetization factor along the out-of-plane direction, and K_p is the interface perpendicular m
a
g
n
e
t
i
c

a
n
i
s
o

$$\frac{\partial E}{\partial\theta} = M_s H_p \sin\theta\cos\theta - M_s H_z \cos\theta + M_s H_x \sin\theta\cos\phi + M_s H_y \sin\theta\sin\phi = 0, \quad (3.10)$$

$$\frac{\partial E}{\partial\phi} = M_s H_x \cos\theta\sin\phi - M_s H_y \cos\theta\sin\phi = 0, \quad (3.11)$$

We can further reduce$\partial E \partial\theta$ $= M_s H_p \sin\theta\cos\theta - M_s H_z \cos\theta + M_s H_x \sin\theta\cos\phi + M_s H_y \sin\theta\sin\phi = 0$, (3.10) and (3.11) using small angle approximation, assuming that the polar angle, θ caused by the AC modulation is small. From this assumption, we then yield,

$$\sin\theta = \frac{H_z}{H_p + H_x\cos\phi + H_y\sin\phi}, \tag{3.12}$$

$$\tan\phi = \frac{H_y}{H_x}, \tag{3.13}$$

In a typical device with in-plane magnetic anisotropy, we can assume that $H_p \gg H_{x,y}$, therefore the 2nd and 3rd terms in the dominator of sinθ=$HzHp+Hx$cos$\phi+Hy$sinϕ, ▯

(3.12) can be ignored. The spin-orbit torque effective field is coupled into two terms: Field-like (FL) and Damping-like (DL). The FL and DL terms are defined as $\boldsymbol{H_F} = H_F\hat{y}$ and $\boldsymbol{H_{DL}} = H_{DL}\boldsymbol{m}\times\hat{y}$, respectively [34,36–38]. Due to the influence of SOT, the injection of a low-frequency AC causes transformations in both FL and DL. Specifically, the FL and DL transform into $\boldsymbol{H_F} = (H_F\sin\omega t)\,\hat{y}$ and $\boldsymbol{H_{DL}} = (H_{DL}\cos\phi\sin\omega t)\,\hat{z}$, respectively. The modulations of the magnetization angle, $\Delta\theta$ and $\Delta\phi$, induced by SOT are then expressed as [35,39],

$$\Delta\theta_0 = \left(\frac{1}{H_P}H_{DL}\cos\phi\right)\sin\omega t, \tag{3.14}$$

$$\Delta\phi_0 = \frac{\cos^2\phi_0}{H_x}H_F\sin\omega t. \tag{3.15}$$

The tilted angle of magnetization concerning the easy axis is governed by the combined effects of the externally applied field and the SOT effective field, $\theta(\phi) = \theta_0(\phi_0) + \Delta\theta_0(\Delta\phi_0)$. Using (3.12)- (3.15), we can rewrite (3.4) as,

as

$$\mathrm{R_{xy}} = R_A\sin(\theta + \Delta\theta_0)\sin\omega t + R_P\cos^2(\theta_0 + \Delta\theta_0)\sin\big(2(\phi_0 + \Delta\phi_0)\big)\sin\omega t\,, \tag{3.16}$$

Assuming there is no external applied field in the $\hat{z}$-direction, $\theta = 0$, the above equation can be further reduced to,

$$\mathrm{R_{xy}} = (R_A\Delta\theta)\sin\omega t + \big(R_p(\sin 2\phi + 2\Delta\phi\cos 2\phi)\big)\sin\omega t, \tag{3.17}$$

substituting (3.12) and (3.13) into (3.17), we will therefore yield,

$$R_{xy} = (R_P \sin 2\phi)\sin \omega t - R_A \frac{H_D}{2H_p}\cos\phi \cos 2\omega t$$
$$-R_P \frac{H_F}{H_x}(2\cos^4\phi - \cos^2\phi)\cos 2\omega t + C, \tag{3.18}$$

where the first harmonic Hall resistance, R_ω and second harmonic Hall resistance, $R_{2\omega}$ is defined as,

$$R_\omega = R_P \sin 2\phi, \tag{3.19}$$
$$R_{2\omega} = R_A \frac{H_D}{2H_p} X + R_P \frac{H_F}{H_x}(X^4 - X^2), \tag{3.20}$$

where $X = \cos\phi$. It is evident that in order to obtain the damping-like and field-like terms, one must examine the second harmonic Hall resistance, $R_{2\omega}$, as indicated in (3.20), which is a 4th-order quadratic equation. The planar Hall effect (PHE) can be easily determined by fitting a sine curve to the first harmonic Hall resistance. Meanwhile, sweeping the out-of-plane field can directly obtain the anomalous Hall effect (AHE) value.

Perpendicular Magnetic Anisotropy (PMA) System

In the case for a system with magnetization pointing out-of-plane from the surface normal, we assume that the equilibrium magnetization does not deviate much from the *z*-axis. We then can rewrite (3.14) and (3.15) as,

$$\Delta\theta_0 = \frac{\Delta H_x \cos\phi + \Delta H_y \sin\phi}{(H_k + H_z)}, \tag{3.21}$$
$$\Delta\phi_0 = \frac{\Delta H_y H_x - \Delta H_x H_y}{H_x^2 + H_y^2}, \tag{3.22}$$

The first and second harmonic voltage is defined as,

$$V_\omega = \frac{1}{2}\Delta I \left[R_A + \left(R_P \sin 2\phi - \frac{R_A}{2}\right)\left(\frac{H}{H_k + H_z}\right)^2\right], \tag{3.23}$$

$$V_{2\omega} = \Delta I \frac{H}{(H_k+H_z)^2} \left[\left(-\frac{1}{4}R_A + R_P \sin 2\phi\right)(\Delta H_x \cos\phi + \Delta H_y \sin\phi) - \frac{1}{2}R_P \cos 2\phi(\Delta H_y \cos\phi - \Delta H_x \sin\phi)\right], \tag{3.24}$$

Using (3.23) and (3.24), we can isolate the effective spin-orbit torque terms by taking the partial derivative and second partial derivative for the $V_{2\omega}$ and V_{ω}, respectively. Thus, the damping-like field and field-like field is express as,

$$\Delta H_x = -2 \frac{\partial V_{2\omega}}{\partial H_x} / \frac{\partial^2 V_{\omega}}{\partial^2 H_x} , \tag{3.25}$$

$$\Delta H_y = -2 \frac{\partial V_{2\omega}}{\partial H_y} / \frac{\partial^2 V_{\omega}}{\partial^2 y} , \tag{3.26}$$

When the planar Hall resistance is significant and cannot be neglected, it is necessary to incorporate a correct factor, $\zeta = \frac{R_P}{R_A}$, to account for the influence of the planar Hall effect on the measurements. The corrected damping-like and field-like fields are thus described as,

$$\Delta H_{x,corrected} = -2 \frac{\Delta H_x \pm 2\zeta \Delta H_y}{1-4\zeta^2}, \tag{3.27}$$

$$\Delta H_{y,corrected} = -2 \frac{\Delta H_y \pm 2\zeta \Delta H_x}{1-4\zeta^2}, \tag{3.28}$$

3.4 Four Probe Technique for Spin-Orbit Torque Characterization

I establish a newly developed technique to determine the spin-orbit torque directly in a continuous film. In this section, I will give a detailed discussion on the developed technique. This technique is a cost-effective characterization of SOT efficiency, which is akin to the current in-plane technique that is currently widely used in the industry for obtaining tunnelling magnetoresistance from thin-film stacks without any lithography steps.

3.4.1 Experimental Details

A continuous film with a stack of Pt(5 nm)/Co(1.4 nm)/Ti(2 nm) was deposited on the SiO_2 substrate using DC magnetron sputtering. Hall-cross device of 5×20 μm was also fabricated as a control sample to determine how the four-probe measure SOT is corrected to align with that measured in the Hall-cross device. The SOT quantification is carried out using

the conventional harmonic method [28,40–42]. Continuous film and Hall cross-device of MgO(2 nm)/Pt(3 nm)/Co(1.4 nm)/Ti(2 nm) were fabricated to validate the difference between four-probe measured SOT in continuous film and conventional harmonic in Hall cross-device. Here, I am quantifying the Hall voltage in the continuous film, therefore, a pair of probes for current injection and a pair for reading voltage is required. The voltage probes are located along the perpendicular bisector between the current probes to minimize errors due to mechanical movement. A customized four-probe arranged in a rhombus geometry with diagonals of 4 mm by 8 mm were built. The four probes made of BeCu were used to ensure minimal response under magnetic fields during measurement. The current probe (I_s ,I_g) and voltage probe (V_s ,V_g) are fixed in the shorter (4 mm) and longer (8 mm) diagonal of the rhombus, respectively, as shown in Fig. 3.8.

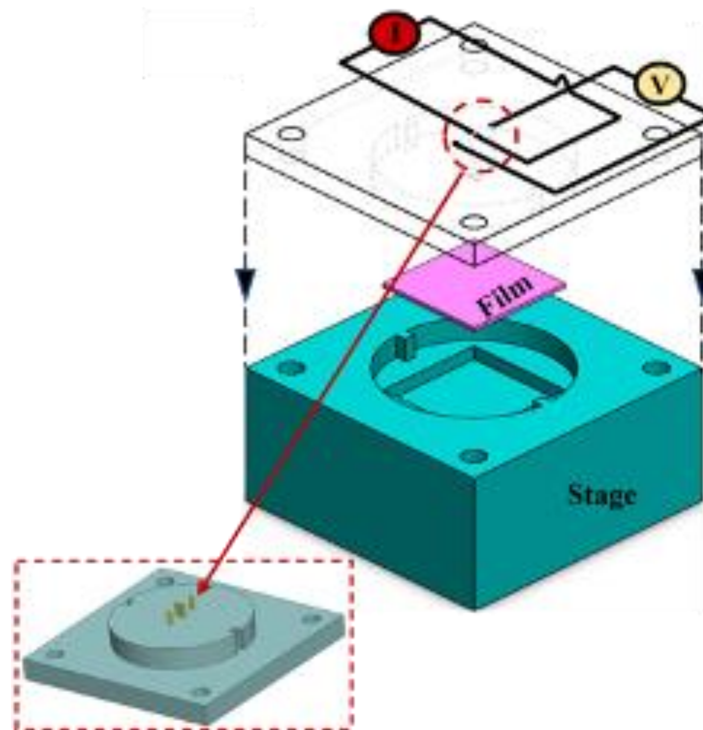

Fig. 3.8: Schematic setup for four-probe harmonic Hall measurement where the current probe distance and voltage probe distance are 4 mm and 8 mm, respectively.

3.4.2 Modeling for Current Distribution

Utilizing the finite-element method (FEM) simulations via COMSOL, I performed a detailed analysis to quantify the extent of current shunting influenced by the placement of voltage probes. As indicated in Fig. 3.9, our simulations provided a comprehensive map of

current distribution for an array of distances between voltage probes. A significant shunting effect was observed for probe separations ≤4 mm. Based on the FEM simulation results, a voltage probe separation of 8 mm emerged as the optimal configuration, where the shunting effect was reduced to less than 6% of the total injected current density.

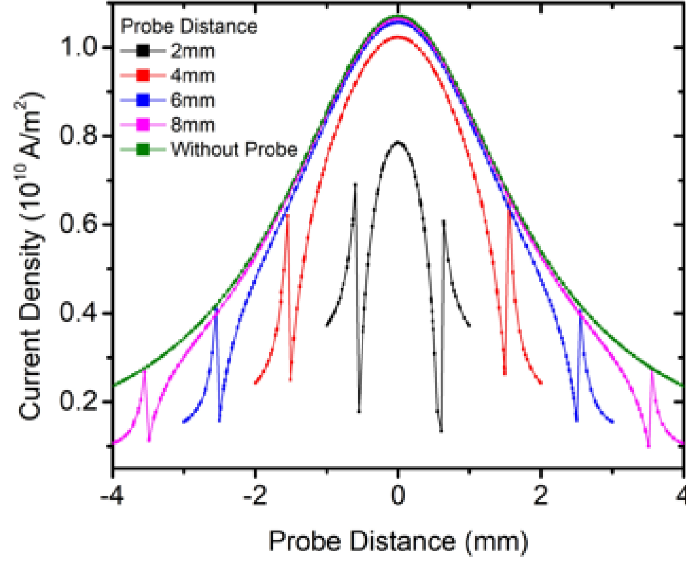

Fig. 3.9: Current distribution due to shunting effects across the different voltage probe distances, d = 2, 4, 6, and 8 mm at a current probe distance of 8 mm.

To gain a deeper understanding on the current density distribution in Hall cross-device and continuous film, FEM was also performed on Hall cross-device with a dimension of $5 \times 20\ \mu m$ and continuous film dimension $4mm \times 8mm$. Fig. 3.10(a) and Fig. 3.10(b) show the FEM simulation results of the surface current between a Hall cross-device and continuous film, respectively. The Hall cross-device displays a near-uniform current distribution due to its defined boundary conditions. In contrast, the continuous film displayed a distinctively divergent current distribution due to the unconstrained boundary. Therefore, a square-like and Gaussian-like current distribution across the characterization width was obtained in the Hall device and continuous film, respectively, as illustrated in Fig. 3.10(c). From the current distribution profile obtained from the finite element simulation, we will discuss the correlation of H_{DL} between Hall cross-device and continuous film. The typical Hall voltage in a strong static field is given by $V_H = \int J(y) R_A dA$, where $J(y)$ is the function of current density distribution dependent on spatial position, y and the anomalous Hall resistance, R_A. The total Hall voltage can be expressed as the summation of the zeroth-order harmonic Hall voltage, V_0 the first harmonic Hall voltage, V_ω and second harmonic Hall voltages, $V_{2\omega}$ [28,43–46],

$$V_H = V_0 + V_\omega \sin \omega t + V_{2\omega} \cos \omega t, \tag{3.29}$$

$$V_\omega = \frac{1}{2} \Delta I R_A \cos \theta$$

$$V_\omega = \frac{1}{2} R_A \cos \theta \int J(y)\, dA, \tag{3.30}$$

$$V_{2\omega} = -\frac{1}{2}\left(\Delta I R_A \sin \theta\right) \Delta \theta$$

$$V_{2\omega} = -\frac{1}{2} R_A \sin \theta \int J(y) \Delta \theta dA, \tag{3.31}$$

where $\Delta\theta$ is the change in the polar magnetization angle from its equilibrium due to the current-induced SOT. This $\Delta\theta$ is proportional to I which yields,

$$V_{2\omega} = \frac{1}{2} k_1 R_A \sin \theta \int | J(y) |^2 dA, \tag{3.32}$$

where $k_1 = \Delta\theta / J$ is a coefficient accounting for the linearly scaling of $\Delta\theta$ to current density. Utilizing V_ω and $V_{2\omega}$, the damping-like field, H_{DL} can be defined by the following relation [28,35,47,48]:

$$\boldsymbol{H}_{DL} = -2\left(\frac{\partial \boldsymbol{V}_{2\omega}}{\partial \boldsymbol{H}} \Big/ \frac{\partial^2 \boldsymbol{V}_\omega}{\partial \boldsymbol{H}^2} \right), \tag{3.33}$$

$$H_{DL} = -2\left(\frac{\partial}{\partial H}\left(\frac{1}{2} k_1 R_A \sin \theta \int | J(y) |^2 dA \right) \Big/ \frac{\partial^2}{\partial H^2}\left(\frac{1}{2} R_A \cos \theta \int J(y) dA \right) \right)$$

$$\boldsymbol{H}_{DL} = k_2 \frac{\int | \boldsymbol{J}(y) |^2 \boldsymbol{dA}}{\int \boldsymbol{J}(y) \boldsymbol{dA}}, \tag{3.34}$$

where k_2 is a linear scaling of H_{DL} per unit current density. To evaluate a correction factor, β_{SOT}, correlating H_{DL} term between Hall cross-device and continuous film, β_{SOT} is defined as,

$$\beta_{SOT} = k_3 \frac{H_{DL,Blanket} / \int J_{Blanket}(y) dy}{H_{DL,Device} / \int J_{Device}(y) dy} = k_3 \frac{\chi_{DL,Blanket}}{\chi_{DL,Device}} = k_3 \frac{\int \left| g_{Blanket}(y) \right|^2 dy}{\int g_{Blanket}(y) dy}, \tag{3.35}$$

where χ_{DL} is the damping-like efficiency and k_3 is a linear scaling factor between J_{avg} and J_0. J_{avg} is the average current density across the whole structure given by $J_{avg} = \frac{I}{t\,w}$, where I is the current, t is the film thickness, and w is the distance between the voltage probe. J_0 is the peak current density across the continuous film, and $g(y)$ is the current distribution in the film.

Therefore, the SOT in Hall cross-device is scalable to SOT in the continuous film by a single constant, β_{SOT}. As shown in (3.35), this β_{SOT} is independent of R_A, indicating that β_{SOT} is constant for any given materials in an identical four-probe geometry setup.

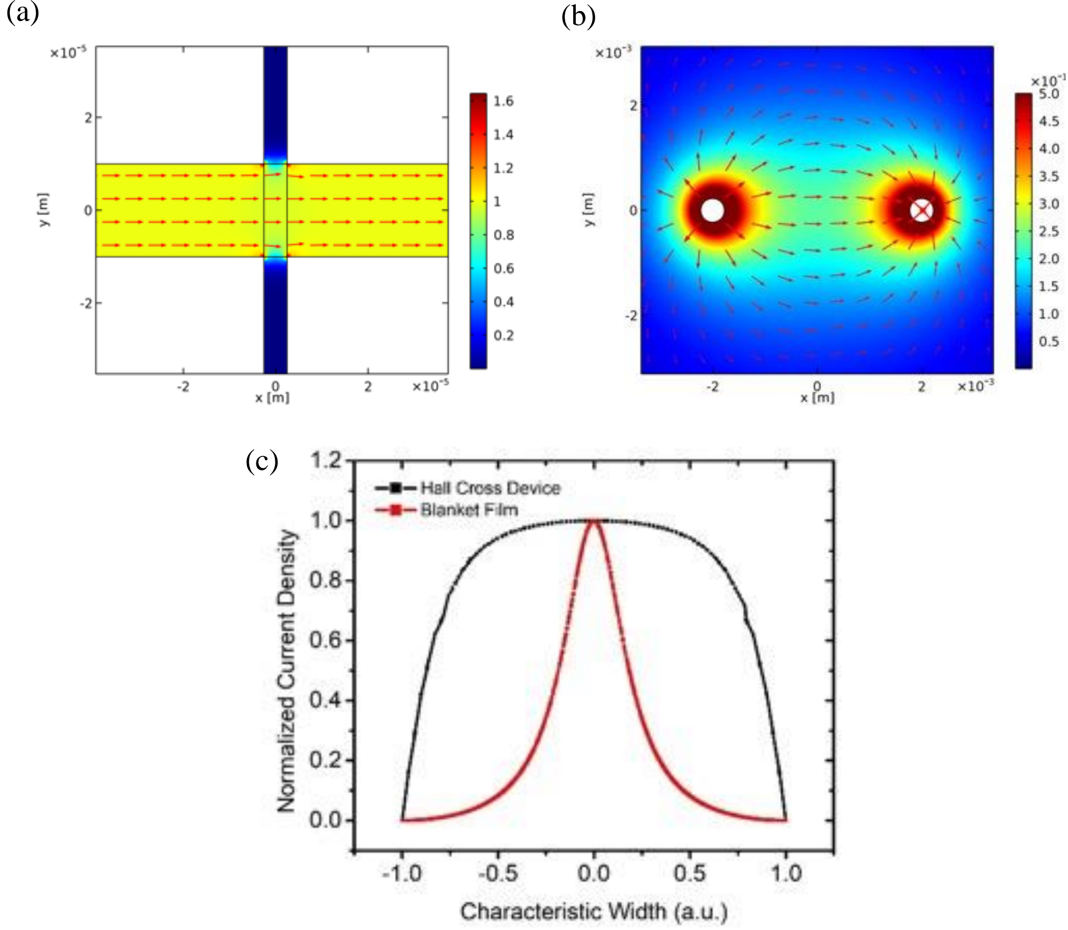

Fig. 3.10: (a) Current distribution in a 20 µm by 5 µm Hall cross device. (b) Current distribution in a continuous thin film at a current probe distance of 8 mm. (c) Current distribution profile of Hall cross device and continuous film.

3.4.3 Spin-Orbit Torque Characterization using Four Probe Technique

Aside from the differences in using a continuous film instead of a Hall cross-device, the four-probe harmonic Hall measurement uses the setup and procedure as the conventional harmonic Hall measurement. The four-probe setup was placed in an in-plane (IP) sweeping magnetic field, H_x of ± 2780 Oe and a fixed out-of-plane (OOP) magnetic field, H_z of 800 Oe. Since the area of measurement in the continuous film is significantly larger than Hall cross-device, a H_Z is required to ensure the PMA continuous film remains saturated without domain nucleation within the effective measurement area [49–52]. AC current was injected through the continuous film in a longitudinal scheme with respect to H_x. The effective area is defined

by the distance between the voltage probe and thin film thickness. The first and second harmonic Hall voltage, V_{ω} and $V_{2\omega}$ were then measured with different current densities ranging from $J_c = 4 \times 10^8$ A/m^2 to 5×10^8 A/m^2. The damping-like field, H_{DL} was then extracted from V_{ω} and $V_{2\omega}$ using (3.33). Fig. 3.11(a) and Fig. 3.11(b) shows the V_{ω} and $V_{2\omega}$ signals with respect to H_y under a range of current densities. To prevent any Joule heating due to the high current injected, the continuous film was subject to cooling period of a duration of 120 s before each current density measurement. The H_{DL} is then extracted by using (3.33) and the damping-like efficiency, χ_{DL} is obtained by fitting H_{DL} against J_c as shown in Fig. 3.11(c). The values shown in Fig. 3.11(c) are averaged over five measurements and the error bar is determined by the standard deviation across all five measurements. To enhance the rigidity and stability of the experimental setup, particularly under the influence of strong magnetic fields, the utilization of non-ferrous pins was undertaken. Non-ferrous materials, which are intrinsically non-magnetic, offer a pivotal advantage in magnetic field-sensitive experiments. The absence of a magnetic response ensures that the pins remain unaffected by the magnetic field, thereby eliminating a potential source of experimental error. However, the high current required for thin film measurements inevitably introduce setup perturbations that limits the measurement resolution, leading to the error shown in Fig. 3.11(c) and Fig. 3.11(d). Here, I have obtained the uncorrected four-probe damping-like efficiency, $\chi_{DL,Blanket}$ of 532 ± 44 Oe per A/m^2 for Pt/Co/Ti structure, which is notably larger than the literature values [40,49,50,53,54]. As previously discussed, the divergence of the current in continuous film is not constraint to a boundary, unlike a pattern Hall cross-device. Therefore, a correction factor, β_{SOT} is necessary to correct $\chi_{DL.Blanket}$ to the damping-like efficiency of device, $\chi_{DL,Device}$. This correction factor, β_{SOT} is experimentally quantified by taking the ratio of χ_{DL} between continuous film and patterned Hall cross device with the identical Pt/Co/Ti heterostructure. The damping-like efficiency of the device, $\chi_{DL,Device}$ was subsequently measured using harmonic Hall technique and found to be 8.4 Oe per 10^{10} A/m^2 as shown in Fig. 3.11(e). Thus, $\beta_{SOT} = k_3 \frac{\chi_{DL,Blanket}}{\chi_{DL,Device}} = 62$ is experimentally evaluated.

I further validated the β_{SOT} value by repeating the experiment with different heterostructure, Ti(2)/Pt(5)/Co(1.4)/Ta(5). Similarly, the uncorrected $\chi_{DL.Blanket}$ of the continuous film and $\chi_{DL.Device}$ of the Hall-cross device are measured to be 971 ± 30 Oe per 10^{10} A/m^2 and 16.1 Oe per 10^{10} A/m^2 respectively, as shown in Fig. 3.11(d) and Fig. 3.11(f), and thus, $\beta_{SOT} = 60$ is evaluated. Therefore, we can conclude that β_{SOT} is measured to be

~ 62. The contribution of SOT from the planar Hall resistance is neglected in this work, as it is negligible in comparison to the anomalous Hall resistance in the PMA sample. Note that the value of β_{SOT} remains unaffected by this estimate as it is a ratio of H_{DL} magnitudes between the continuous film and Hall cross-device computed under the same assumptions. Utilizing this value of β_{SOT}, H_{DL} of any ferromagnetic heterostructure can directly be determined without any lithography process.

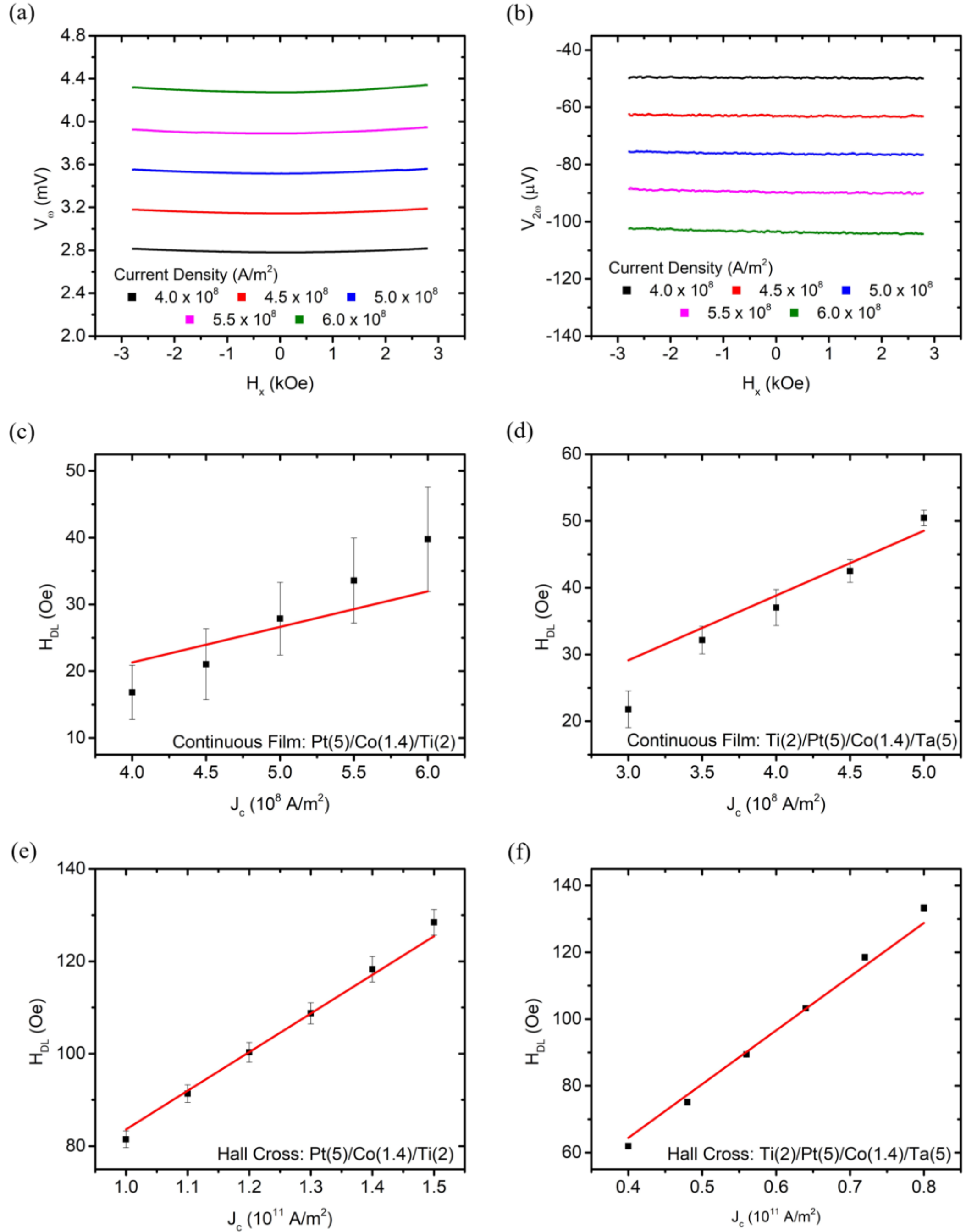

Fig. 3.11: (a) First harmonic voltage, V_ω and (b) second harmonic voltage, $V_{2\omega}$ in a four-probe harmonic measurement across different ranges of current densities, J_c for Pt/Co/Ti continuous film. (c) and (d) Four-probe results for damping-like field, H_{DL} as a function of J_c for

Pt(5)/Co(1.4)/ Ti(2) and Ti(2)/Pt(5)/Co(1.4)/Ta(5), respectively. (e) and (f) Damping-like field, H_{DL} as a function of J_c for Pt(5)/Co(1.4)/Ti(2) and Ti(2)/Pt(5)/Co(1.4)/Ta(5) for Hall cross devices.

In addition to the SOT measurement, the four-probe is also applicable in measuring out-of-plane magnetic hysteresis loop using the anomalous Hall resistance measurement. The anomalous Hall resistance, R_{AHE} of the Pt/Co/Ti structure are measured by applying a sweeping out-of-plane field, H_z of ± 400 Oe concurrently with an AC current density, J_c of 1×10^9 A/m^2 and 1×10^{10} A/m^2 to the continuous film and Hall device, respectively. Fig. 3.12(a) shows the ratio between anomalous Hall resistance, R_{AHE} (Hall cross-device and continuous film) and R_{sat}, where R_{sat} is the magnitude of anomalous Hall resistance of Hall device. The $R_{AHE,device}$ is found to be approximately 20 times larger than $R_{AHE,blanket}$ due to the non-uniform current distribution. The correction factor in AHE measurement should not be compared directly with SOT measurement because in AHE measurement, an OP field is applied to saturate the magnetization in $\pm m_z$. Since the magnetization is always in $\boldsymbol{M} = \pm(0,0,m_z)$, hence $\Delta m = 0$. Therefore, AHE measurement is linearly proportional to the profile of the non-uniform current distribution shown in Fig. 3.12(b). Whereas in the harmonic Hall measurement for SOT, I am measuring ΔR_H which is dependent on the changed in magnetization $\Delta m(x, y, z)$. Due to SOT, $\Delta m(x, y, z)$ will be perturbed following the current density distribution, hence the SOT measurement is directly proportional to the square of the profile of the non-uniform current distribution, which results in different correction factors obtained between AHE and SOT measurement.

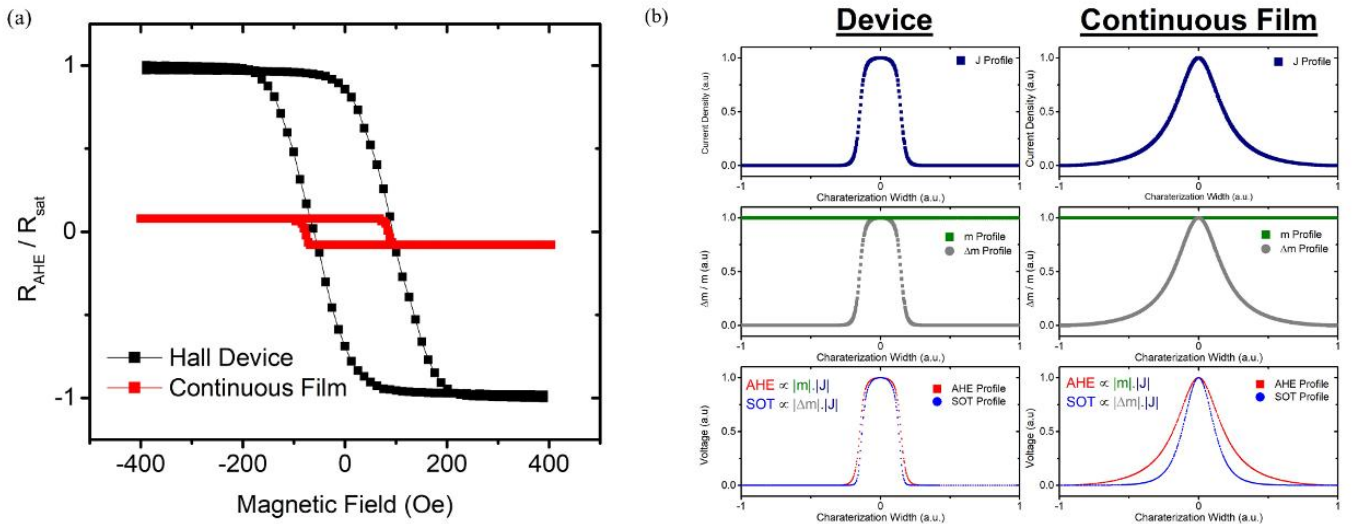

Fig. 3.12: Ratio between anomalous Hall resistance, R_{AHE} (Hall cross device and continuous film) and R_{sat}, where R_{sat} is the magnitude of anomalous Hall resistance of Hall device. (b) Comparison between Hall cross-device and continuous film for current density profile (1st row), m and Δm profile (2nd row), and AHE / SOT profile (3rd row).

In summary, I have presented a novel measurement technique employing a four-probe setup to directly ascertain the SOT in heterostructures, circumventing the need for time-consuming and resource-intensive lithography processes. The H_{DL} of continuous films was successfully characterized using the harmonic Hall technique by accounting for the divergent current distribution via a constant scaling factor. This correction factor of 62, was experimentally quantified by taking the ratio of H_{DL} between continuous films and Hall devices. The proposed technique offers a cost-effective means of characterizing SOT efficiency, which is akin to the current in-plane method widely employed in the industry to obtain tunnelling magnetoresistance from thin-film stacks without necessitating lithographic steps.

References

[1] F. Shi, *Introductory Chapter: Basic Theory of Magnetron Sputtering*, in edited by D. F. Shi (IntechOpen, Rijeka, 2018), p. Ch. 4.

[2] D. Constantin, M. Apreutesei, R. Arvinte, A. Marin, O. C. Andrei, and D. Munteanu, *MAGNETRON SPUTTERING TECHNIQUE USED FOR COATINGS DEPOSITION; TECHNOLOGIES AND APPLICATIONS*, in (2011).

[3] R. Kukla, *Magnetron Sputtering on Large Scale Substrates: An Overview on the State of the Art*, Surf. Coatings Technol. **93**, 1 (1997).

[4] S. Swann, *Film Thickness Distribution in Magnetron Sputtering*, Vacuum **38**, 791 (1988).

[5] S. Swann, *Magnetron Sputtering*, Phys. Technol. **19**, 67 (1988).

[6] J. A. Thornton, *Influence of Apparatus Geometry and Deposition Conditions on the Structure and Topography of Thick Sputtered Coatings*, J. Vac. Sci. Technol. **11**, 666 (1974).

[7] A. Acharya and S. Sahoo, *Electron Beam Lithography and It ' s Application in Nanoscale Fabrication*, **8**, 91 (2018).

[8] K. Mølhave, D. N. Madsen, and P. Bøggild, *A Simple Electron-Beam Lithography System.*, Ultramicroscopy **102**, 215 (2005).

[9] A. A. Tseng, K. Chen, C. D. Chen, and K. J. Ma, *Electron Beam Lithography in Nanoscale Fabrication: Recent Development*, IEEE Trans. Electron. Packag. Manuf. **26**, 141 (2003).

[10] L. Mader and J. Hoepfner, *Ion Beam Etching of Silicon Dioxide on Silicon*, J. Electrochem. Soc. **123**, 1893 (1976).

[11] P. J. Revell and G. F. Goldspink, *A Review of Reactive Ion Beam Etching for Production*, Vacuum **34**, 455 (1984).

[12] W. Burgei, M. J. Pechan, and H. Jaeger, *A Simple Vibrating Sample Magnetometer for Use in a Materials Physics Course*, Am. J. Phys. **71**, 825 (2003).

[13] S. Foner, *Versatile and Sensitive Vibrating-Sample Magnetometer*, Rev. Sci. Instrum. **30**, 548 (2004).

[14] M. Nasrollahzadeh, M. Atarod, M. Sajjadi, S. M. Sajadi, and Z. Issaabadi, *Chapter 6 - Plant-Mediated Green Synthesis of Nanostructures: Mechanisms, Characterization, and Applications*, in *An Introduction to Green Nanotechnology*, edited by M. Nasrollahzadeh, S. M. Sajadi, M. Sajjadi, Z. Issaabadi, and M. B. T.-I. S. and T. Atarod,

Vol. 28 (Elsevier, 2019), pp. 199–322.

[15] S. First and V. S. M. Principles, *Vsm Principles*, Water 1 (2006).

[16] P. Kinsler, *Faraday's Law and Magnetic Induction: Cause and Effect, Experiment and Theory*, Physics.

[17] D. Erenso, *Faraday's Law*, Virtual and Real Labs for Introductory Physics II.

[18] F. C. Strong, *Faraday's Laws in One Equation*, J. Chem. Educ. **38**, 98 (1961).

[19] A. A. Bunaciu, E. gabriela Udriştioiu, and H. Y. Aboul-Enein, *X-Ray Diffraction: Instrumentation and Applications*, Crit. Rev. Anal. Chem. **45**, 289 (2015).

[20] H. A. Foner and N. Adan, *The Characterization of Papers by X-Ray Diffraction (XRD): Measurement of Cellulose Crystallinity and Determination of Mineral Composition*, J. Forensic Sci. Soc. **23**, 313 (1983).

[21] A. Ali, Y. W. Chiang, and R. M. Santos, *X-Ray Diffraction Techniques for Mineral Characterization: A Review for Engineers of the Fundamentals, Applications, and Research Directions*, Minerals.

[22] Y. Joly, S. D. Matteo, and O. Bunău, *Resonant X-Ray Diffraction: Basic Theoretical Principles*, Eur. Phys. J. Spec. Top. **208**, 21 (2012).

[23] A. L. Ryland, *X-Ray Diffraction*, J. Chem. Educ. **35**, 80 (1958).

[24] R. P. T. McGuire, *Anisotropic Magnetoresistance in Ferromagnetic 3d Alloys.Pdf*, IEEE Trans. Magn. **11**, (1975).

[25] M. A. Roberts and C. C. Tang, *Angular Resolution of Parallel Foils on a Synchrotron Powder Diffractometer*, J. Synchrotron Radiat. **5**, 1270 (1998).

[26] S. Li, S. Goolaup, J. Kwon, F. Luo, W. Gan, and W. S. Lew, *Deterministic Spin-Orbit Torque Induced Magnetization Reversal in Pt/[Co/Ni] n /Co/Ta Multilayer Hall Bars*, Sci. Rep. **7**, 1 (2017).

[27] Q. Y. Wong, C. Murapaka, W. C. Law, W. L. Gan, G. J. Lim, and W. S. Lew, *Enhanced Spin-Orbit Torques in Rare-Earth Pt/ [Co/Ni] 2/Co/Tb Systems*, Phys. Rev. Appl. **11**, 024057 (2019).

[28] M. Hayashi, J. Kim, M. Yamanouchi, and H. Ohno, *Quantitative Characterization of the Spin-Orbit Torque Using Harmonic Hall Voltage Measurements*, Phys. Rev. B - Condens. Matter Mater. Phys. **89**, 1 (2014).

[29] X. Fan, H. Celik, J. Wu, C. Ni, K. J. Lee, V. O. Lorenz, and J. Q. Xiao, *Quantifying Interface and Bulk Contributions to Spin-Orbit Torque in Magnetic Bilayers*, Nat. Commun. **5**, (2014).

[30] E. S. Park, D. K. Lee, B. C. Min, and K. J. Lee, *Elimination of Thermoelectric Artifacts*

in the Harmonic Hall Measurement of Spin-Orbit Torque, Phys. Rev. B **100**, 214438 (2019).

[31] M. Hayashi, J. Kim, M. Yamanouchi, and H. Ohno, *Quantitative Characterization of the Spin-Orbit Torque Using Harmonic Hall Voltage Measurements*, Phys. Rev. B - Condens. Matter Mater. Phys. **89**, 144425 (2014).

[32] V. G. Bar'yakhtar and B. A. Ivanov, *The Landau-Lifshitz Equation: 80 Years of History, Advances, and Prospects*, Low Temp. Phys. **41**, 663 (2015).

[33] G V Skrotskiĭ, *The Landau-Lifshitz Equation Revisited*, Sov. Phys. Uspekhi **27**, 977 (1984).

[34] K. Garello, I. M. Miron, C. O. Avci, F. Freimuth, Y. Mokrousov, S. Blügel, S. Auffret, O. Boulle, G. Gaudin, and P. Gambardella, *Symmetry and Magnitude of Spin-Orbit Torques in Ferromagnetic Heterostructures*, Nat. Nanotechnol. **8**, 587 (2013).

[35] F. Luo, S. Goolaup, W. C. Law, S. Li, F. Tan, C. Engel, T. Zhou, and W. S. Lew, *Simultaneous Determination of Effective Spin-Orbit Torque Fields in Magnetic Structures with in-Plane Anisotropy*, Phys. Rev. B **95**, 174415 (2017).

[36] J. Yoon, S.-W. Lee, J. H. Kwon, J. M. Lee, J. Son, X. Qiu, K.-J. Lee, and H. Yang, *Anomalous Spin-Orbit Torque Switching Due to Field-like Torque-Assisted Domain Wall Reflection.*, Sci. Adv. **3**, e1603099 (2017).

[37] H. Wu, S. A. Razavi, Q. Shao, X. Li, K. L. Wong, Y. Liu, G. Yin, and K. L. Wang, *Spin-Orbit Torque from a Ferromagnetic Metal*, Phys. Rev. B **99**, 1 (2019).

[38] Y. Wang, P. Deorani, X. Qiu, J. H. Kwon, and H. Yang, *Determination of Intrinsic Spin Hall Angle in Pt*, Appl. Phys. Lett. **105**, (2014).

[39] H. Y. Poh, C. C. I. Ang, W. L. Gan, G. J. Lim, and W. S. Lew, *Direct Spin Accumulation Quantification in Ferromagnetic Heterostructures Using DC Bias Harmonic Hall Measurement*, Phys. Rev. B **104**, 224416 (2021).

[40] T. Jin, W. C. Law, D. Kumar, F. Luo, Q. Y. Wong, G. J. Lim, X. Wang, W. S. Lew, and S. N. Piramanayagam, *Enhanced Spin–Orbit Torque Efficiency in Pt/Co/Ho Heterostructures via Inserting Ho Layer*, APL Mater. **8**, 111111 (2020).

[41] S. C. Baek, V. P. Amin, Y.-W. Oh, G. Go, S.-J. Lee, G.-H. Lee, K.-J. Kim, M. D. Stiles, B.-G. Park, and K.-J. Lee, *Spin Currents and Spin–Orbit Torques in Ferromagnetic Trilayers*, Nat. Mater. **17**, 509 (2018).

[42] L. You, O. J. Lee, D. Bhowmik, D. Labanowski, J. Hong, J. Bokor, and S. Salahuddin, *Switching of Perpendicularly Polarized Nanomagnets with Spin Orbit Torque without an External Magnetic Field by Engineering a Tilted Anisotropy*, Proc. Natl. Acad. Sci.

U. S. A. **112**, 10310 (2015).

[43] E.-S. Park, D.-K. Lee, B.-C. Min, and K.-J. Lee, *Elimination of Thermoelectric Artifacts in the Harmonic Hall Measurement of Spin-Orbit Torque*, Phys. Rev. B **100**, 214438 (2019).

[44] B. Han, B. Wang, Z. Yan, T. Wang, D. Yang, X. Fan, Y. Wang, and J. Cao, *Determination of the Spin-Orbit Torques in Ferromagnetic--Heavy-Metal Bilayers Using Harmonic Longitudinal Voltage Measurements*, Phys. Rev. Appl. **13**, 14065 (2020).

[45] L. Neumann and M. Meinert, *Influence of the Hall-Bar Geometry on Harmonic Hall Voltage Measurements of Spin-Orbit Torques*, AIP Adv. **8**, 95320 (2018).

[46] C. Engel, S. Goolaup, F. Luo, and W. S. Lew, *Characterizing Angular Dependence of Spin-Orbit Torque Effective Fields in Pt/(Co/Ni)2/Co/IrMn Structure*, IEEE Trans. Magn. **53**, (2017).

[47] C. Engel, S. Goolaup, F. Luo, and W. S. Lew, *Quantitative Characterization of Spin-Orbit Torques in Pt/Co/Pt/Co/Ta/BTO Heterostructures Due to the Magnetization Azimuthal Angle Dependence*, Phys. Rev. B **96**, 054407 (2017).

[48] Y. Du, R. Thompson, M. Kohda, and J. Nitta, *Origin of Spin–Orbit Torque in Single-Layer CoFeB Investigated via in-Plane Harmonic Hall Measurements*, AIP Adv. **11**, 25033 (2021).

[49] X. Tao, Q. Liu, B. Miao, R. Yu, Z. Feng, L. Sun, B. You, J. Du, K. Chen, S. Zhang, L. Zhang, Z. Yuan, D. Wu, and H. Ding, *Self-Consistent Determination of Spin Hall Angle and Spin Diffusion Length in Pt and Pd: The Role of the Interface Spin Loss.*, Sci. Adv. **4**, eaat1670 (2018).

[50] S. Keller, L. Mihalceanu, M. R. Schweizer, P. Lang, B. Heinz, M. Geilen, T. Brächer, P. Pirro, T. Meyer, A. Conca, D. Karfaridis, G. Vourlias, T. Kehagias, B. Hillebrands, and E. T. Papaioannou, *Determination of the Spin Hall Angle in Single-Crystalline Pt Films from Spin Pumping Experiments*, New J. Phys. **20**, 53002 (2018).

[51] X. Liu, W. L. Lim, L. V Titova, M. Dobrowolska, J. K. Furdyna, M. Kutrowski, and T. Wojtowicz, *Perpendicular Magnetization Reversal, Magnetic Anisotropy, Multistep Spin Switching, and Domain Nucleation and Expansion in Ga1−xMnxAs Films*, J. Appl. Phys. **98**, 63904 (2005).

[52] T. Nishimura, D.-H. Kim, T. Okuno, Y. Hirata, Y. Futakawa, H. Yoshikawa, S. Kim, A. Tsukamoto, Y. Shiota, T. Moriyama, and T. Ono, *Determination of Perpendicular Magnetic Anisotropy Based on the Magnetic Droplet Nucleation*, Jpn. J. Appl. Phys. **57**,

50308 (2018).

[53] L. Zhu, D. C. Ralph, and R. A. Buhrman, *Spin-Orbit Torques in Heavy-Metal--Ferromagnet Bilayers with Varying Strengths of Interfacial Spin-Orbit Coupling*, Phys. Rev. Lett. **122**, 77201 (2019).

[54] H. Xie, J. Yuan, Z. Luo, Y. Yang, and Y. Wu, *In-Situ Study of Oxygen Exposure Effect on Spin-Orbit Torque in Pt/Co Bilayers in Ultrahigh Vacuum*, Sci. Rep. **9**, 17254 (2019).

Chapter 4 Direct Spin Accumulation Quantification in Ferromagnetic Heterostructures using DC bias Harmonic Hall Measurement

Spin accumulation has been a subject of continued pursuit to understand spin-orbit torque switching mechanisms for spintronics device applications. Effective methods to precisely characterize spin accumulation in a ferromagnet are yet to be demonstrated. In this chapter, I establish an all-electrical novel quantification of spin accumulation in the ferromagnetic layer using DC-bias harmonic Hall measurements. The inclusion of the DC bias results in an anomalous resistance due to spin accumulation, quantifiable via the first harmonic Hall resistance. This newly introduced technique provides an all-electrical alternative to determine spin accumulation by utilizing the easily accessible harmonic Hall characterization technique. Part of this chapter has been published in *Physical Review B* [1].

4.1 Introduction

The Spin Hall Effect (SHE), an essential phenomenon in the domain of spintronics, involves the transformation of a charge current traversing a metallic material into a spin current. This mechanism occurs due to spin-dependent scattering events that are influenced by spin-orbit coupling within the materials [2–4]. As a result of such scattering, spins accumulate along the periphery of the metallic layer, a process referred to as spin accumulation. When a heavy metal (HM) layer is employed and interfaced with a ferromagnetic (FM) layer, diffusion of the accumulated spins occurs from the HM layer into the FM layer. The transferred spins, in turn, engage in an exchange of angular momentum with the local magnetization within the FM layer [4–10]. This exchange process engenders the phenomenon known as spin-orbit torque (SOT).

The quantification of this spin accumulation within the FM layer is crucial, given that it directly impacts the magnitude of the SOT. Prior studies have employed the longitudinal MOKE technique for characterizing spin accumulation in HM layers [4–8], but comprehensive quantification of the net spins diffused from the HM to the FM layer, specifically for FM/HM bilayer structures, presents a complex challenge. This complexity arises from factors such as spin backflow (SBF), where the spins are reflected back into the HM layer, thereby reducing

the net spin accumulation within the FM layer [15], and spin memory loss (SML), which describes the process where spins flip beyond the spin diffusion length [16,17]. Another significant challenge lies in the detection of the optical signal generated by spin accumulation. Since this signal is typically small, spatial imaging is quite challenging, with the resolution often being restricted by the optical diffraction limit [18]. While x-ray magnetic circular dichroism (XMCD) has been utilized for directly quantifying spin accumulation in the FM layer in HM/FM structures [9–11], the need for a synchrotron facility, which is not easily accessible, makes this approach less widespread. Therefore, a reliable, accessible, and accurate characterization technique capable of directly quantifying spin accumulation in the FM layer has been a subject of continued pursuit in the effort of understanding the SOT mechanism. Such a method is highly desired as it will significantly advance our understanding of the underlying mechanics of SOT, thereby providing important insights for the development of future spintronic devices.

In this work, I demonstrate direct electrical detection of spin accumulation in the Co layer in a Si/SiO_2/Ta/Co/Pt structure with in-plane magnetic anisotropy (IMA) using harmonic Hall measurement technique with a direct current (DC) bias. The inclusion of the DC bias results in an anomalous resistance originating from spin accumulation induced by the spin Hall effect. The sign of this anomalous resistance is dependent on the accumulated spins being parallel or antiparallel to the local magnetization. A correlation between the quantified spin accumulation and the damping-like term was determined in a Ta thickness-dependent study. Our electrical measurement approach opens up a new avenue for direct measurement of spin accumulation in a ferromagnetic layer, which can potentially be more sensitive and accurate as compared to MOKE microscopy, while being more accessible as compared to XMCD.

4.2 Experimental Model

The harmonic Hall measurement technique quantifies two mutually orthogonal components of the SOT: Damping-like field $\boldsymbol{H}_D = H_D\, \boldsymbol{m} \times \mathbf{p}$ and field-like field, $\boldsymbol{H}_F = H_F \mathbf{p}$, where $\mathbf{p}$ is the polarized spin orientation of electrons [12–19]. In this technique, sweeping field and alternating current are applied to induce the first and second harmonic Hall resistance, R_ω and $R_{2\omega}$ respectively. The R_ω provides information about the equilibrium magnetization direction, and the $R_{2\omega}$ provides information about the SOT-induced small tilting of magnetization from the equilibrium via the planar Hall effect (PHE) and anomalous Hall effect

(AHE) [17–21]. With the inclusion of a DC bias, the spin accumulation effect induced by SHE is expected to either enhance/dimmish the PHE, depending on the alignment of spin accumulation relative to the magnetization direction. This changed in the PHE allows the measurement of the net spin accumulation. The direction of the accumulated spin is dependent on the direction of the current flow and the sign of characteristic material spin Hall angle, θ_H. This relation can be described by $\hat{s} = (\hat{v} \times \hat{n}\,(\theta_H))$, where $\hat{s}$ is the direction of the accumulated spin, $\hat{v}$ is the direction of electron flow, and $\hat{n}$ is the surface normal. In the system where the current is injected in the $+\hat{x}$-direction, and structure with positive spin Hall angle, such as Pt, the electrons are scattered towards the top/bottom interface while being polarized in the $\pm\hat{y}$-direction. Therefore, I propose that the spin accumulation will manifest as a change in the planar Hall resistance in the $\hat{y}$-direction. The R_ω for an IMA structure can be expressed as $R_\omega = R_P \sin 2\phi$, where R_p is planar Hall resistance which is proportional to $m_x m_y$ and ϕ is the azimuthal angle as shown in Fig. 4.1(a). Due to the accumulation of spins in the $\hat{y}$ direction, the R_ω is given by:

$$R_\omega = r_p\left(m_x\,.\,(m_y + s)\right)\,\sin 2\phi, \tag{4.1}$$

$$R_\omega = (R_p + \Delta R_P)\sin 2\phi, \tag{4.2}$$

where r_p is the coefficient of planar Hall resistance, ΔR_P is the additional planar Hall resistance due to spin accumulation, and s is the spin accumulation. Spin accumulation was quantified using the harmonic Hall measurement technique with a DC bias, applying the DC simultaneously with the adiabatic AC along the Hall cross structure. The alignment of the magnetization in the $\hat{y}$-direction can be fixed by the external magnetic field, $\pm H_y$. The polarity of H_y will not affect ΔR_p since the polarity of accumulated spins is only dependent on the direction of current flow.

When $\pm H_y$ is applied, the magnitude of the of R_ω are expected to be different due to the direction of the accumulated spins. The ΔR_p is obtained by summing up these values of $R_\omega(\pm H_y)$, which can be defined as,

$$\Delta R_P = \frac{R_\omega(+H_y) + R_\omega(-H_y)}{2}, \tag{4.3}$$

The spin accumulation, ζ, is then determined by the ratio between ΔR_p and R_p.

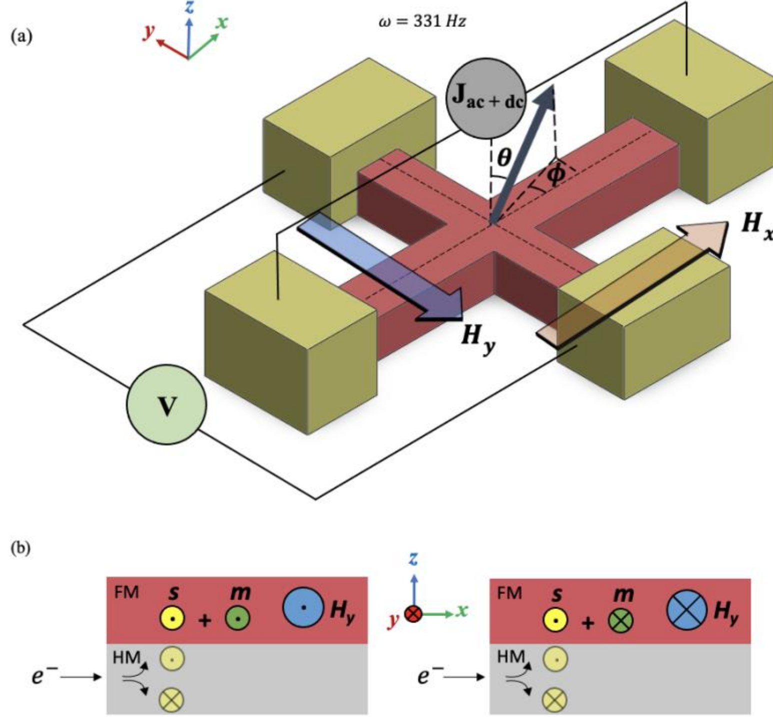

Fig. 4.1: (a) Schematic of DC bias harmonic Hall setup in the longitudinal configuration. (b) Schematic of the spin accumulation in the FM/HM structure with in-plane anisotropy. Spins are accumulated in the $+\hat{y}$ direction in the FM layer when the injected electron is in the $+\hat{x}$ direction. Local magnetization, $\boldsymbol{m}$ follows the direction of the external field, H_y. The amplitude of first Harmonics resistance, R_ω increases (decreases) when spin accumulations, ***s***, are parallel (antiparallel) to the local magnetization of the FM layer as described in (4.2).

The applied DC bias is substantial to induce the thermoelectric effect, V_{TE}, however, this effect is accounted for and found to be negligible. The sign V_{TE} is dependent on the magnetization ($\boldsymbol{m} \times \boldsymbol{\nabla T}$) where $\boldsymbol{\nabla T}$ is the temperature gradient due to Joule heating in the $\hat{x}$ and $\hat{z}$-directions [22,23]. Since the sweeping field is in $\hat{x}$-direction, the first harmonic Hall voltage due to V_{TE} will be cancelled out due to the opposite signs of m_y. Hence, the influence of V_{TE} will been eliminated in the quantification of the spin accumulation. Since the spin accumulation quantification in our model is dependent on ΔR_P, it is primarily applicable to IMA structures, where the spins and initial magnetization are parallel / anti-parallel to each other. For the case for PMA materials, the Hall voltage signal is dominated by the anomalous Hall effect, leaving negligible ΔR_P signal.

4.3 Experimental Details

Harmonic Hall measurements were carried out on Si/SiO_2/Ta(2 nm)/Co(2 nm)/Pt(5 nm) Hall cross structure to characterize the SOT efficiency. The thin film stack was deposited using DC magnetron sputtering and subsequently patterned into a 5×20 μm Hall cross structure using a combination of optical lithography and ion milling techniques. Vibrating sample magnetometer (VSM) measurement shows that the film stack has IMA with saturation magnetization, $M_s = 650 \pm 18$ emu/cc [24], as shown in Fig. 4.2.

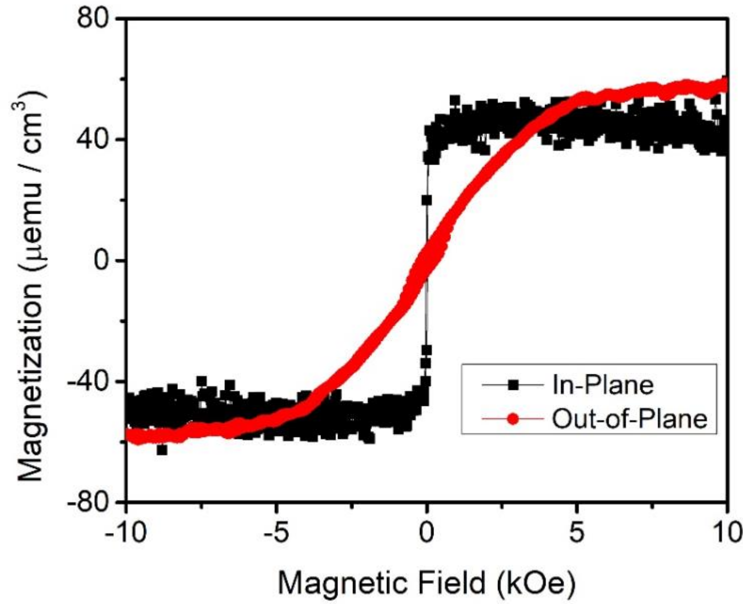

Fig. 4.2: Vibrating sample magnetometer results for Ta(2)/Co(2)/Pt(5) structure. The black and red plot represent the in-plane and out-of-plane sweeping, respectively.

The harmonic Hall technique was used to obtain the R_{ω} and $R_{2\omega}$ with respect to the azimuthal angle of magnetization $\phi = \arctan\frac{H_y}{H_x}$, where H_x is the fixed external magnetic field of 600 Oe, and H_y is the sweeping magnetic field ranging from –4000 Oe to 4000 Oe. Uniform AC densities, j_{ac} ranging from 1×10^{11} A/m² to 1.5×10^{11} A/m² were applied in the $\hat{x}$-direction to obtain the damping-like efficiency. H_D is determined from $R_{2\omega}$ using [25]:

$$R_{2\omega} = R_A \frac{H_D}{2H_s} X + R_p \frac{H_F}{H_{x_{ext}}} (2X^4 - X^2), \tag{4.4}$$

where $X = \cos\phi$ and H_s is the saturation field. H_D is plotted against the electric field, $\boldsymbol{E}$ as shown in Fig. 4.4(b), and the electric field can be obtained by $\boldsymbol{E} = \rho_{xx}\boldsymbol{j}$, where ρ_{xx} is the resistivity of the structure, and $\boldsymbol{j}$ is the uniform current density flowing into the structure. The dependence on an electric field is preferred over uniform current density because the different resistivities of the layer will result in different current densities within the constituents of the trilayer. The uniform current density flowing into the trilayer will be less than the current density in Pt, resulting in overestimating the SOT efficiency. In addition, there is more than one source generating SOT, it is experimentally impractical to isolate the individual SOT efficiency.

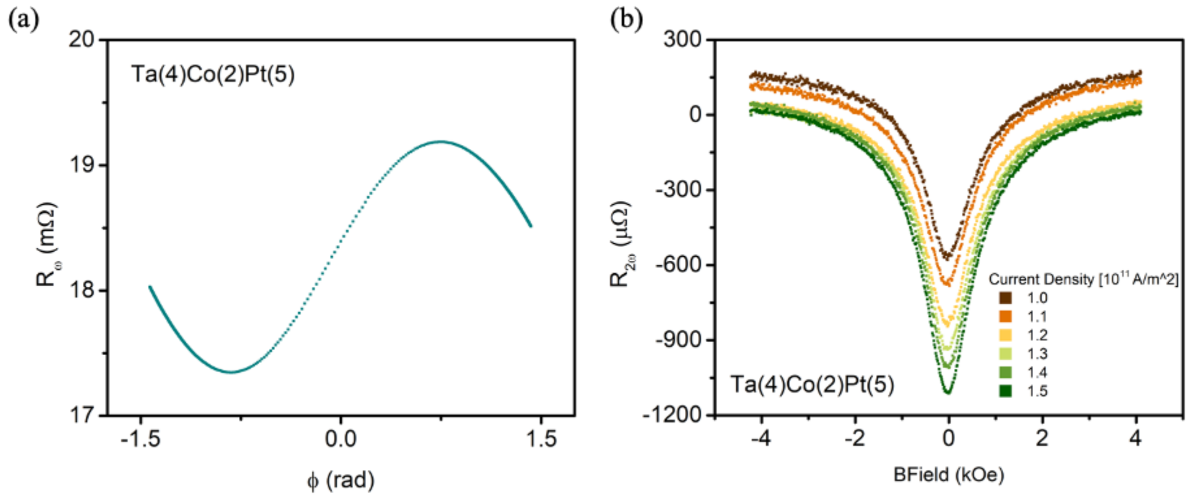

Fig. 4.3: The harmonic Hall measurement results for Ta(4)/Co(2)Pt(5) structure (a) First harmonic Hall resistance describing (4.2) (b) Second harmonic Hall resistance with various current density

4.4 Characterization of Spin-Orbit Torque Field in Ta/Co/Pt and Ti/Co/Pt

The SOT damping-like efficiency, ζ_{DL}^{E} can be calculated by $\zeta_{DL}^{E} = \frac{\mu_0 M_s t \boldsymbol{H_D}}{\boldsymbol{E}}$ [26], where μ_0 is the permeability of vacuum, and t is the thickness of the FM layer. The results for the $R_{2\omega}$ and ζ_{DL}^{E} for Si/SiO2/Ti/Co/Pt and Si/SiO2/Ta/Co/Pt are shown in Fig. 4.4(c). The ζ_{DL}^{E} increased from $(20.05 \pm 0.07) \times 10^5\ (\Omega\mathrm{m})^{-1}$ to $(35.99 \pm 2.07) \times 10^5\ (\Omega\mathrm{m})^{-1}$ when the thickness of Ta is increased from 2 nm to 10 nm. This is because increasing the thickness of Ta will increase the percentage content of β-phase Ta which had been reported for higher contribution of SOT [27–29]. The magnitude of these ζ_{DL}^{E} correspond to approximately the effective spin Hall angle of 0.138 to 0.276 ($\theta_H^{eff} = \frac{2eM_s t H_D}{\hbar j}$) under the assumption of uniform

current density injection through the trilayer structure which are comparable to various other reports [25,27,30–32]. The ζ_{DL}^{E} in Ti structure shown to be negligible and does not increase with Ti thickness. This results is expected as Ti is a weak SOC material and do not have high charge-to-spin conversion.

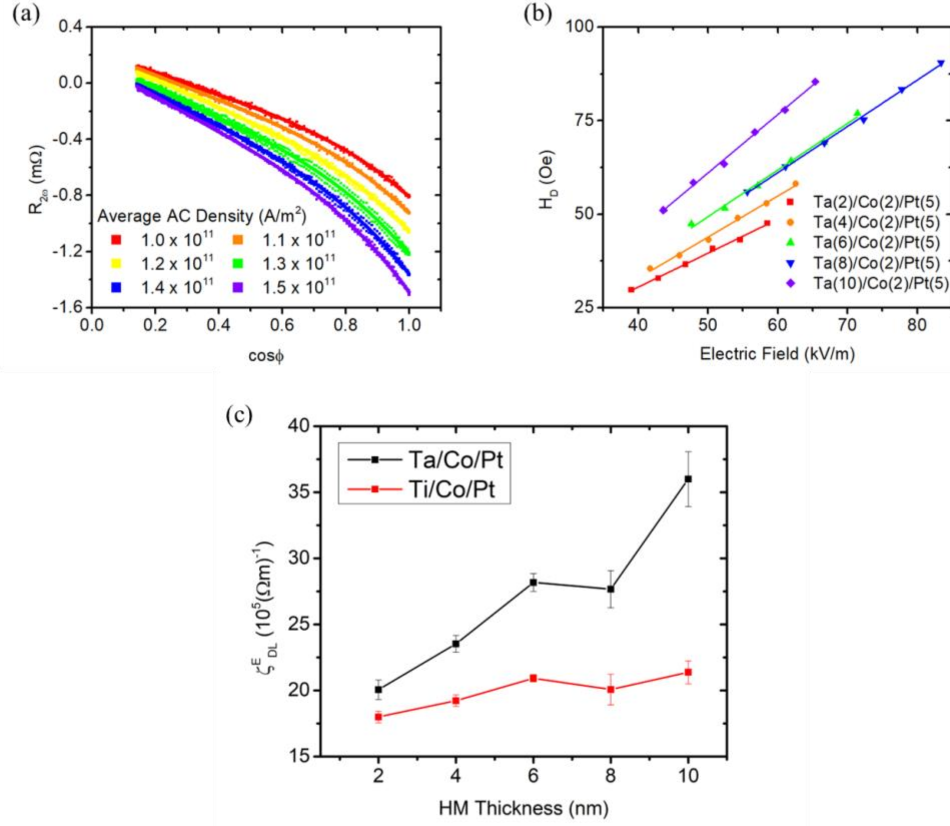

Fig. 4.4: (a) $R_{2\omega}$ as a function of $\cos\phi$, for average current density ranging from $1 - 1.5 \times 10^{10} A/m^2$. Graph of $AX + B(2X^4 - X^2)$ is fitted to the data. (b) H_D as a function of electric field for various Ta thicknesses ranging from 2 nm to 10 nm. (c) ζ_{DL}^{E} as a function of Ta (black) and Ti (red) thickness.

4.5 Quantification of Spin Accumulation

In order to quantify the spin accumulation in the FM layer, a uniform AC current density, $j_{ac} = 5.0 \times 10^{10}$ A/m² with a DC offset, $j_{dc} = 5.0 \times 10^{10}$ A/m² was injected through the trilayer structure in a longitudinal scheme with respect to the sweeping field. R_{ω} was measured under a sweeping magnetic field of $\pm$1000 Oe in the $\hat{x}$-direction and a fixed magnetic field of 600 Oe in the $\hat{y}$-direction. As seen in (4.2), the amplitude of R_{ω} determines the total planar Hall resistance, $(R_p + \Delta R_P)$. The experimental results show that R_P is measured to be $63.2\ m\Omega$ for zero DC bias. Therefore, I can conclude that the spin of the electrons are polarized in the $-\hat{y}$-direction in the FM layer. With the presence of DC bias, the

polarized spins are aligned parallel (antiparallel) to the localized magnetization of the FM, leading to an increase (decrease) in total magnetization, as illustrated in Fig. 4.1(b). Without an applied DC ($j_{DC} = 0$), there will be no net accumulated spin. Hence, the amplitude of the R_ω between $+H_y$ and $-H_y$ is expected to be the same. The ΔR_P is obtained by summing the amplitude of R_ω for $\pm H_y$. As shown in Fig. 4.5(a), the magnitude of ΔR_P are calculated from the difference in $R_\omega(\pm H_y)$, hence the effect of parasitic thermal effect is mitigated. A linear trend in ΔR_P is observed from the sweeping j_{DC} from 1×10^{10} A/m^2 to 5×10^{10} A/m^2, which also validate the absence of Joule heating. Thus, a linear fit is used to determine the rate of change of ΔR_p per electric field. From the gradient of the linear fit, the spin accumulation is calculated by $\boldsymbol{s} = \frac{1}{R_P}\frac{d\Delta R_p}{dE}$.

To both confirm that the SHE is the dominant source resulting in spin accumulation and an increase in spin accumulation would lead to a larger ΔR_P, measurements were performed on samples with Ta thickness ranging from 2 nm to 10 nm. The measurement results of spin accumulation in the Co layer with varying Ta thickness are shown in Fig. 4.5(b). Factoring in the M_s of the Hall structure, the obtained spin accumulation results are $1.19 \times 10^{17}\ \mu_B/cm^3$ per V/m and $2.05 \times 10^{17} \mu_B/cm^3$ per V/m, for Ta = 2 nm and Ta = 10 nm, respectively. In addition, a similar trend of spin accumulation and the ζ_{DL}^E with Ta thickness in Si/SiO_2/Ta/Co/Pt is observed, as shown in Fig. 4.5(b). The Rashba effect is an interfacial effect independent of the HM thickness, whereas SHE is a bulk effect dependent on the HM thickness. These results further affirm the dominance of the spin Hall effect in our stack structures, which is the cause of spin accumulation building up in the FM layer. To quantify the degree of influence in spin accumulation on the FM layer, the measured spin accumulation is normalized to the saturation magnetization of the FM layer, and a value of 0.29% per kV/m in Co for Si/SiO_2/Ta(10)/Co(2)/Pt(5) is obtained.

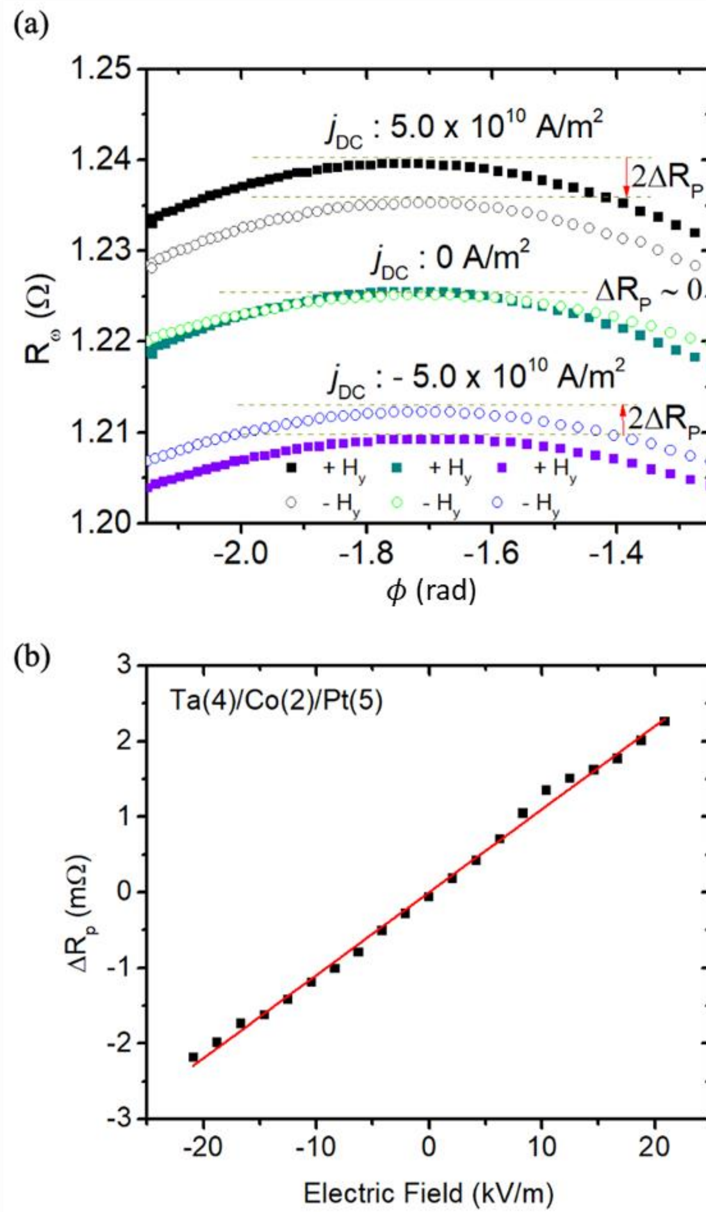

Fig. 4.5: (a) R_ω for $+H_y$ (solid square) and $-H_y$ (open circle). Offsets have been applied to the R_ω for better clarity. R_ω for $-H_y$ is flipped for a clearer comparison. Spin accumulation is parallel (antiparallel) to $+H_y$ ($-H_y$), leading to a higher amplitude in the $R_\omega$at the current density of $j_{DC} = 5.0 \times 10^{10}$ A/m^2. (b) Amplitude of ΔR_P with respect to the electric field. The slope of ΔR_P over electric field is $0.11\ m\Omega$ per kV/m.

The measurement was repeated on another IMA sample of Si/SiO_2/Ti(2)/Co(2)/Pt(5) with Ti ranging from 2 nm to 10 nm. Since Ti was reported to have a low damping-like term, it will be intriguing to determine how the spin accumulation changes with the damping-like efficiency. The results of the spin accumulation and damping-like efficiency are shown in Fig. 4.6. Spin accumulation of $2.09 \times 10^{16}\ \mu_B/cm^3$ per V/m was obtained for the

$Si/SiO_2/Ti(2)/Co(2)/Pt(5)$ sample. To align the unit of spin accumulation measurement to make a comparison with reported values, our measured spin accumulation in $Si/SiO_2/Ti/Co/Pt$ is in the range $1.55 \times 10^{-4} \sim 2.09 \times 10^{-4}$ μ_B/atom per 10^6 A/cm^2. This value is comparable to $\sim 1.75 \times 10^{-4}$ μ_B/atom per 10^6 A/cm^2, which is measured by XMCD in Co/Pt structure [10]. The measured spin accumulation from Ti, s_{Ti} is lower than spin accumulation from Ta, s_{Ta}. This further shows that spin accumulation is proportional to the damping-like efficiency.

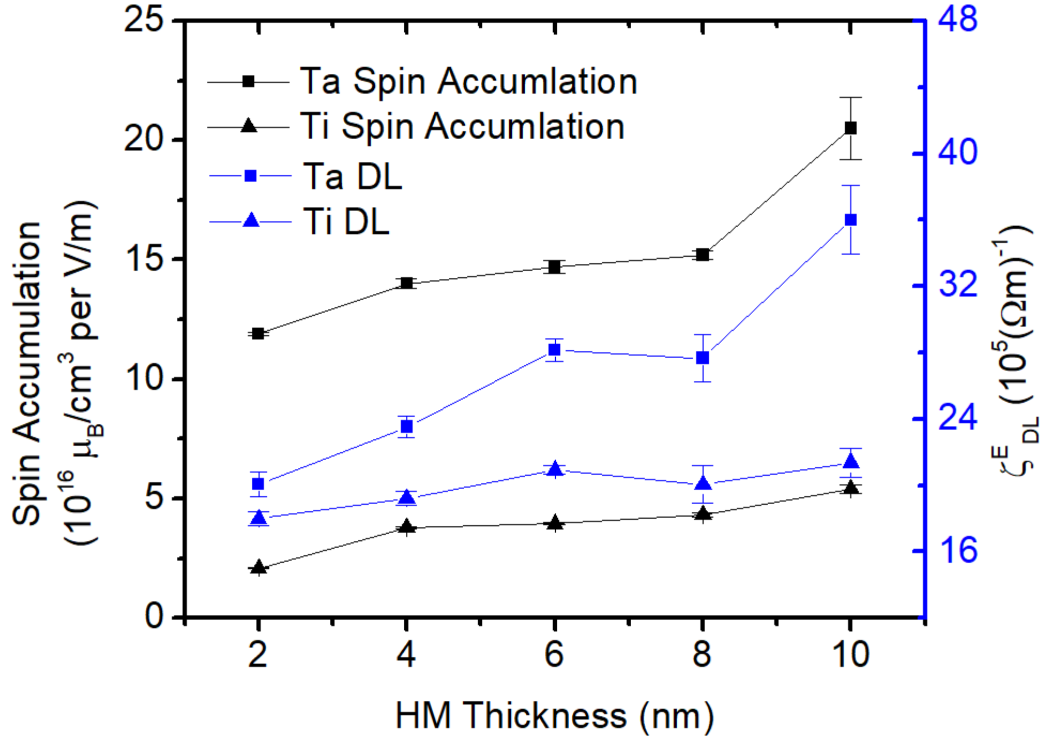

Fig. 4.6: Spin accumulation of Ta (black square) and Ti (black triangle), and DL efficiency of Ta (blue square) and Ti (black triangle) with various HM thicknesses ranging from 2 nm to 10 nm.

4.6 Conclusion

In conclusion, current-induced spin accumulation in $Si/SiO_2/Ta/Co/Pt$ and $Si/SiO_2/Ti/Co/Pt$ structures have been quantified using the harmonic Hall measurement technique with DC bias. This experiment shows that the spin accumulation is approximately 0.29% per kV/m of the local magnetization for 10 nm Ta. These results demonstrate that, besides the conventional SOT measurement, spin accumulation can also be quantified using the harmonic Hall technique. The ratio of the spin accumulation over the applied electric field shows a similar trend with damping-like efficiency as the thickness of HM increases. Hence,

the ratio can be used to evaluate the efficiency of an HM in converting electric current to spin current. This provides an all-electrical alternative to determine spin accumulation by utilizing the easily accessible harmonic Hall characterization technique.

References

[1] H. Y. Poh, C. C. I. Ang, W. L. Gan, G. J. Lim, and W. S. Lew, *Direct Spin Accumulation Quantification in Ferromagnetic Heterostructures Using DC Bias Harmonic Hall Measurement*, Phys. Rev. B **104**, 224416 (2021).

[2] J. Sinova, S. O. Valenzuela, J. Wunderlich, C. H. Back, and T. Jungwirth, *Spin Hall Effects*, Rev. Mod. Phys. **87**, 1213 (2015).

[3] S. Murakami and N. Nagaosa, *Spin Hall Effect*, Compr. Semicond. Sci. Technol. **1–6**, 222 (2011).

[4] C. Stamm, C. Murer, M. Berritta, J. Feng, M. Gabureac, P. M. Oppeneer, and P. Gambardella, *Magneto-Optical Detection of the Spin Hall Effect in Pt and W Thin Films*, Phys. Rev. Lett. **119**, 087203 (2017).

[5] F. Fohr, S. Kaltenborn, J. Hamrle, H. Schultheiß, A. A. Serga, H. C. Schneider, B. Hillebrands, Y. Fukuma, L. Wang, and Y. Otani, *Optical Detection of Spin Transport in Nonmagnetic Metals*, Phys. Rev. Lett. **106**, 3 (2011).

[6] G. M. Choi, *Magneto-Optical Kerr Effect Driven by Spin Accumulation on Cu, Au, and Pt*, Appl. Sci. **8**, (2018).

[7] V. Sih, R. C. Myers, Y. K. Kato, W. H. Lau, A. C. Gossard, and D. D. Awschalom, *Spatial Imaging of the Spin Hall Effect and Current-Induced Polarization in Two-Dimensional Electron Gases*, Nat. Phys. **1**, 31 (2005).

[8] P. Riego, S. Vélez, J. M. Gomez-Perez, J. A. Arregi, L. E. Hueso, F. Casanova, and A. Berger, *Absence of Detectable Current-Induced Magneto-Optical Kerr Effects in Pt, Ta, and W*, Appl. Phys. Lett. **109**, 172402 (2016).

[9] J. Ding, W. Zhang, M. B. Jungfleisch, J. E. Pearson, H. Ohldag, V. Novosad, and A. Hoffmann, *Direct Observation of Spin Accumulation in Cu Induced by Spin Pumping*, Phys. Rev. Res. **2**, 2 (2020).

[10] C. Stamm, C. Murer, Y. Acremann, M. Baumgartner, R. Gort, S. Däster, A. Kleibert, K. Garello, J. Feng, M. Gabureac, Z. Chen, J. Stöhr, and P. Gambardella, *X-Ray Spectroscopy of Current-Induced Spin-Orbit Torques and Spin Accumulation in Pt/3d - Transition-Metal Bilayers*, Phys. Rev. B **100**, 024426 (2019).

[11] R. Kukreja, S. Bonetti, Z. Chen, D. Backes, Y. Acremann, J. A. Katine, A. D. Kent, H. A. Dürr, H. Ohldag, and J. Stöhr, *X-Ray Detection of Transient Magnetic Moments Induced by a Spin Current in Cu*, Phys. Rev. Lett. **115**, 096601 (2015).

[12] I. M. Miron, G. Gaudin, S. Auffret, B. Rodmacq, A. Schuhl, S. Pizzini, J. Vogel, and P.

Gambardella, *Current-Driven Spin Torque Induced by the Rashba Effect in a Ferromagnetic Metal Layer*, Nat. Mater. **9**, 230 (2010).

[13] S. Emori, U. Bauer, S. M. Ahn, E. Martinez, and G. S. D. Beach, *Current-Driven Dynamics of Chiral Ferromagnetic Domain Walls*, Nat. Mater. **12**, 611 (2013).

[14] T. D. Skinner, K. Olejník, L. K. Cunningham, H. Kurebayashi, R. P. Campion, B. L. Gallagher, T. Jungwirth, and A. J. Ferguson, *Complementary Spin-Hall and Inverse Spin-Galvanic Effect Torques in a Ferromagnet/Semiconductor Bilayer*, Nat. Commun. **6**, 4 (2015).

[15] K. Garello, I. M. Miron, C. O. Avci, F. Freimuth, Y. Mokrousov, S. Blügel, S. Auffret, O. Boulle, G. Gaudin, and P. Gambardella, *Symmetry and Magnitude of Spin-Orbit Torques in Ferromagnetic Heterostructures*, Nat. Nanotechnol. **8**, 587 (2013).

[16] X. Wang and A. Manchon, *Diffusive Spin Dynamics in Ferromagnetic Thin Films with a Rashba Interaction*, Phys. Rev. Lett. **108**, 117201 (2012).

[17] J. Kim, J. Sinha, M. Hayashi, M. Yamanouchi, S. Fukami, T. Suzuki, S. Mitani, and H. Ohno, *Layer Thickness Dependence of the Current-Induced Effective Field Vector in Ta|CoFeB|MgO*, Nat. Mater. **12**, 240 (2013).

[18] M. Jamali, K. Narayanapillai, X. Qiu, L. M. Loong, A. Manchon, and H. Yang, *Spin-Orbit Torques in Co/Pd Multilayer Nanowires*, Phys. Rev. Lett. **111**, 246602 (2013).

[19] M. Hayashi, J. Kim, M. Yamanouchi, and H. Ohno, *Quantitative Characterization of the Spin-Orbit Torque Using Harmonic Hall Voltage Measurements*, Phys. Rev. B - Condens. Matter Mater. Phys. **89**, 1 (2014).

[20] P. P. J. Haazen, E. Murè, J. H. Franken, R. Lavrijsen, H. J. M. Swagten, and B. Koopmans, *Domain Wall Depinning Governed by the Spin Hall Effect*, Nat. Mater. **12**, 299 (2013).

[21] X. Qiu, W. Legrand, P. He, Y. Wu, J. Yu, R. Ramaswamy, A. Manchon, and H. Yang, *Enhanced Spin-Orbit Torque via Modulation of Spin Current Absorption*, Phys. Rev. Lett. **117**, 217206 (2016).

[22] E. S. Park, D. K. Lee, B. C. Min, and K. J. Lee, *Elimination of Thermoelectric Artifacts in the Harmonic Hall Measurement of Spin-Orbit Torque*, Phys. Rev. B **100**, 214438 (2019).

[23] H. Yang, H. Chen, M. Tang, S. Hu, and X. Qiu, *Characterization of Spin-Orbit Torque and Thermoelectric Effects via Coherent Magnetization Rotation*, Phys. Rev. B **102**, 24427 (2020).

[24] Q. Y. Wong, C. Murapaka, W. C. Law, W. L. Gan, G. J. Lim, and W. S. Lew, *Enhanced*

Spin-Orbit Torques in Rare-Earth Pt/ [Co/Ni] 2/Co/Tb Systems, Phys. Rev. Appl. **11**, 024057 (2019).

[25] F. Luo, S. Goolaup, W. C. Law, S. Li, F. Tan, C. Engel, T. Zhou, and W. S. Lew, *Simultaneous Determination of Effective Spin-Orbit Torque Fields in Magnetic Structures with in-Plane Anisotropy*, Phys. Rev. B **95**, 174415 (2017).

[26] L. Zhu, D. C. Ralph, and R. A. Buhrman, *Enhancement of Spin Transparency by Interfacial Alloying*, Phys. Rev. B **99**, 180404 (2019).

[27] S. Woo, M. Mann, A. J. Tan, L. Caretta, and G. S. D. Beach, *Enhanced Spin-Orbit Torques in Pt / Co / Ta Heterostructures Enhanced Spin-Orbit Torques in Pt / Co / Ta Heterostructures*, Appl. Phys. Lett. **105**, 212404 (2016).

[28] L. Liu, C. F. Pai, Y. Li, H. W. Tseng, D. C. Ralph, and R. A. Buhrman, *Spin-Torque Switching with the Giant Spin Hall Effect of Tantalum*, Science (80-.). **336**, 555 (2012).

[29] G. Allen, S. Manipatruni, D. E. Nikonov, M. Doczy, and I. A. Young, *Experimental Demonstration of the Coexistence of Spin Hall and Rashba Effects in β-Tantalum/Ferromagnet Bilayers*, Phys. Rev. B - Condens. Matter Mater. Phys. **91**, 144412 (2015).

[30] C. Hahn, G. De Loubens, O. Klein, M. Viret, V. V. Naletov, and J. Ben Youssef, *Comparative Measurements of Inverse Spin Hall Effects and Magnetoresistance in YIG/Pt and YIG/Ta*, Phys. Rev. B **87**, 174417 (2013).

[31] F. Luo, Q. Y. Wong, S. Li, F. Tan, G. J. Lim, X. Wang, and W. S. Lew, *Dependence of Spin-Orbit Torque Effective Fields on Magnetization Uniformity in Ta/Co/Pt Structure*, Sci. Rep. **9**, 0 (2019).

[32] S. Woo, M. Mann, A. Tan, L. Carreta, and G. Beach, *Characterization of Spin-Orbit Torques in Pt/Co/Ta Structures*, 2015 IEEE Int. Magn. Conf. 1 (2015).

Chapter 5 Crystallinity Control of Topological Insulator BiSb(012) *via* Interfacial Engineering for Spin-Orbit Torque Enhancement

Topological insulators demonstrate high charge-spin conversion efficiency due to their spin-momentum locking at the Dirac surface states. However, the surface states are sensitive to disruption caused by exchange coupling when interfaced with a ferromagnet. In this Chapter, I demonstrate the use of various non-magnetic insertion layer materials at the Co/BiSb(012) interface to preserve the topological surface state and promote spin-orbit torque efficiency through the crystallinity control of BiSb(012). I further explore the enhancement of BiSb(012) crystallinity with increasing BiSb thickness. Part of this chapter has been published in *Physical Review Applied* [1].

5.1 Introduction

The emergence of spin-orbit torque (SOT) has opened avenues for applied spintronic devices by exploiting electrical and spin manipulation to achieve fast magnetization switching and low-power consumption [2–4]. Typically, heavy metals such as Pt, Ta, and W are commonly used as spin sources in ferromagnet-heavy metal (FM-HM) heterostructure. The strong spin-orbit coupling in these materials allows the generation of spin currents via the spin Hall effect [5–8]. However, the relatively small spin Hall angle (< 1) poses a bottleneck to the further advancement of SOT devices [5–9]. Meanwhile, topological insulators (TIs) exhibit remarkable spintronic properties due to their unique spin-momentum locking and topologically protected surface states, as depicted in Fig. 5.1(a) [10–15]. These properties have gained significant interest in the field and have been proposed as potential alternatives to heavy metals for SOT generation.

Recent works have reported large spin Hall angle, θ_{SH} in several TIs, such as $\theta_{SH} = 3.5$ in Bi_2Se_3, $\theta_{SH} = 18.6$ in Bi_xSe_{1-x}, and $\theta_{SH} \sim 52$ in BiSb/MnGa [15–17]. However, these significant results typically necessitate the formation of epitaxial single-crystal structures, which are often achieved through molecular beam epitaxy growth techniques. Therefore, this requirement can present challenges for large-scale and cost-effective device fabrication.

Additionally, complications arise when a topological insulator is in directly adjacent with a ferromagnet. The difference in work function between the TI and the ferromagnet results in a shift of the topological surface state below the Fermi energy level. The hybridization of these surface states with metal bands will hence destroy the helical spin structure, hence the spin momentum locking will not be preserved [12,18–20]. Therefore, insertion layers such as Ru, Au, Cu, and Ag have been previously used to decouple the direct exchange coupling between the TI-FM interface [21–24]. Besides exchange decoupling, the insertion layer also plays a critical role in influencing the crystallinity of the TIs and consequently affects the SOT performance. Theoretical prediction and ARPES measurements have shown that the BiSb(012) topological surface state has three Dirac cones at the $\bar{\Gamma}, \bar{\mathrm{X}}$, and $\bar{M}$ points, which are crucial in obtaining strong SOT [15,25,26]. Hence, an insertion layer that promotes a strong BiSb(012) phase is highly desirable.

In this work, I investigate the crystallinity control of BiSb(012) in the magnetic multilayer structure, Ti(1 nm)/Co(5)/[Ti(1 nm),Cu(1 nm),Pt(1 nm)]/BiSb(20 nm)/Ti(1 nm), as shown in Fig. 5.1(b), to promote the SOT by utilizing different insertion layers (Ti, Cu, Pt) at the TI-FM interface. The SOT efficiency of these device structures was characterized using the harmonic Hall technique, and crystallinity was determined using x-ray diffractometry. I also extended this work to explore the SOT performance dependence on BiSb thickness from 10 to 100 nm, which revealed further improvement in SOT efficiency that closely correlates to BiSb(012) crystallinity.

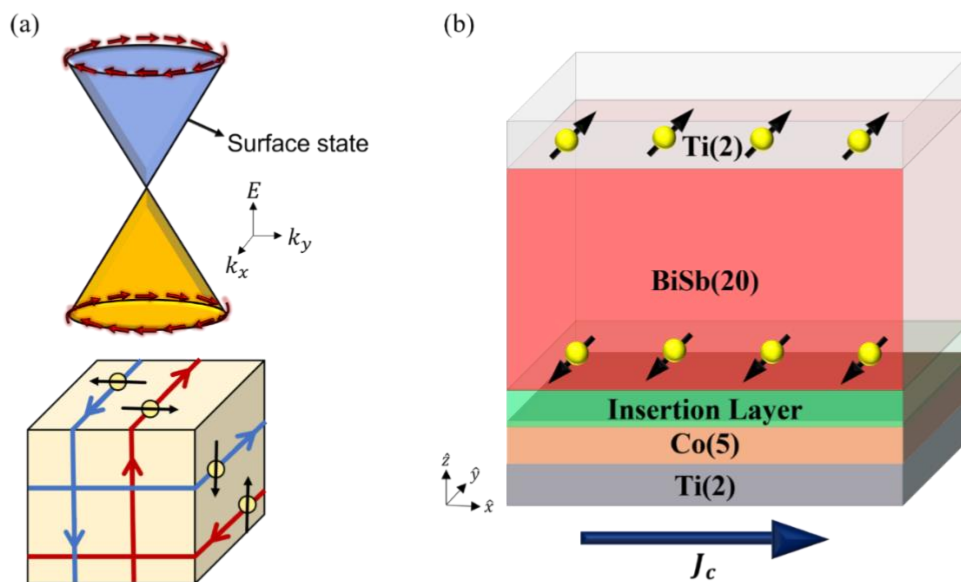

Fig. 5.1: **The electronic band structure of a topological insulator and sample structure**. (a) The Dirac-like cone of the dispersion at the surface of a topological insulator and real-space interpretation of the surface state of a topological insulator. (b) Schematic structure of Ti/Co/[Ti, Cu, Pt]/BiSb/Ti, where the elements in the square bracket are the different insertion layers

5.2 Experimental Details

The thin film stacks, comprising of Ti(1 nm)/Co(5 nm)/ [Cu (1 nm), Ti (1 nm), Pt (1 nm)]/$Bi_{0.85}Sb_{0.15}$(20 nm)/Ti(1 nm), where the square bracket indicates different insertion layer, were deposited on SiO2 substrate using DC/RF magnetron sputtering at room temperature. To improve the quality of the BiSb layer, the BiSb was sputtered at a low sputtering rate of 0.059 nm/s using RF magnetron sputtering of 30 W with a base pressure of $\sim 7 \times 10^{-8}$ Torr, and sputtering pressure of 3×10^{-8} Torr. Upon deposition, the thin films were then patterned into a Hall-cross configuration of 5 μm × 20 μm dimension, achieved through a combination of optical lithography and lift-off technique as discussed in Chapter 3. Spin-orbit torque efficiency was characterized using the second harmonic Hall technique on the resulting Hall-cross devices. In the harmonic Hall measurement, the first harmonic Hall resistance, R_{ω} and second harmonic Hall resistance, $R_{2\omega}$ were obtained with respect to the applied magnetic field. Here a static magnetic field, H_x, of 600 Oe was applied simultaneously with a sweeping magnetic field, H_y, ranging from -4200 Oe to 4200 Oe. Average AC density, J_{ac} ranging from 2×10^{10} A/m^2 to 3×10^{10} A/m^2 was applied in the $\hat{x}$-direction to determine the damping-like field, H_{DL} which can be extracted from $R_{2\omega}$ [27,28],

$$R_{2\omega} = \left(\frac{R_A H_D}{2H_S} + R_{\nabla T}\right)X + \frac{R_P H_F}{H_x}(2X^4 - X^2), \tag{5.1}$$

where R_A is the anomalous Hall resistance, R_P is the planar Hall resistance, $R_{\nabla T}$ is the resistance due to thermal effect, X = cos ϕ, where ϕ is the azimuthal angle given by, $\phi = \arctan\frac{H_y}{H_x}$, and H_s is the saturation field.

The sheet resistance of the BiSb was measured using the four-probe resistivity measurement. The conductivity of the corresponding thickness is therefore calculated as shown in the **Table 5.1** below,

Table 5.1: Conductivity of BiSb

Thickness [nm]	σ $[\Omega^{-1}\mathrm{m}^{-1}]$
BiSb (10)	1.02×10^5
BiSb (15)	9.52×10^4
BiSb (20)	7.69×10^4
BiSb (25)	7.14×10^4
BiSb (30)	6.25×10^4
BiSb (50)	5.67×10^4
BiSb (100)	6.23×10^4

The numbers in the round-bracket represent the thickness of the BiSb in nm. As shown in **Table 5.1**, unlike other metals, the conductivity of topological insulator (TI) BiSb decreases with increasing thickness. The conductivity of TI's can be defined as [29–31],

$$\sigma = \frac{\sigma_S t_S}{t} + \sigma_B$$

where σ_S and σ_B is the conductivity of the surface states and bulk states of TI, respectively. t_S and t is the thickness of the surface and the film. Here, we can observe that as $t \to \infty$, σ will approach σ_B where the bulk state is dominant. Whereas, when $t \to 0$, the surface conduction will be significant, hence $\sigma > \sigma_B$. As such, the conductivity of TI decreases with the increment of TI's thickness.

5.3 Parasitic Thermal Measurement

I performed angular dependence harmonic Hall measurement on the sample, Ti/Co/Cu/BiSb/Ti, to support the validity of neglecting these parasitic thermal effects in this work. The second harmonic Hall resistance is defined as,

$$R_{2\omega} = \left(\frac{R_A B_{AD}}{B_{ext}} + R_{\nabla T}\right)\cos\phi + 2R_P(2\,(\cos^3\phi - \cos\phi)\,\frac{B_{FL}+B_{Oe}}{B_{ext}}\ , \quad (5.2)$$

where R_A is the anomalous Hall resistance, B_{AD} is the damping-like field, B_{ext} is the applied external field, $R_{\nabla T}$ is the thermal resistance due to the parasitic effect, R_P is the planar Hall resistance, B_{FL} is the field-like field, and B_{Oe} is the Oersted field.

In this measurement, a static magnetic field of 0.14 to 0.83 T was applied at an azimuthal angle of 0 to 360 degrees with respect to the applied current density of $1\ \times 10^{10}$ A/m^2. The 2nd harmonic Hall resistance, $R_{2\omega}$ was obtained as shown in Fig. 5.2 (Top panel) below. The field-like field is subsequently obtained by subtracting the cosine fitting from the raw data which is shown in Fig. 5.2 (Bottom panel).

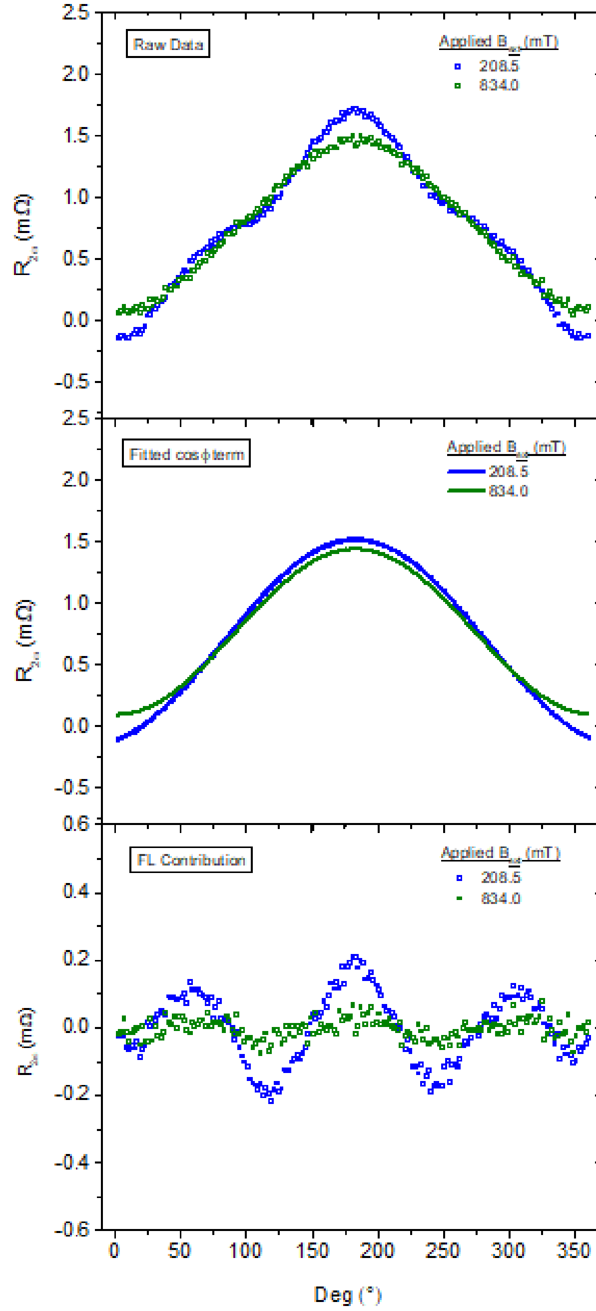

Fig. 5.2: (Top panel) Experimental data for $R_{2\omega}$ as a function of the azimuthal angle, ϕ at different applied external field. (Middle panel) Cosine fit for the experimental data. (Bottom panel) Field-like contribution after subtracting the cosine fitting from experimental data.

Figure 5.3 shows the relation between the damping-like field with the inverse of the static and demagnetization fields. From the angular dependence measurement, the parasitic terms are calculated to be 0.34 $m\Omega$, and the spin Hall angle is 7.83, which is ≈ 2.4% less than the original value of 8.02. Therefore, I assumed that the parasitic effect is neglected in the

measurement. In additional, the focus of the work is on the crystallinity control of BiSb(012) *via* interfacial engineering, hence further investigation on the parasitic effect is not conducted.

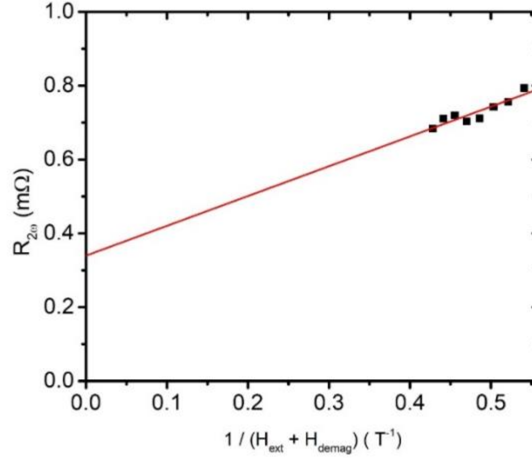

Fig. 5.3: $R_{2\omega}$ as a function of the inverse of the static fields and demagnetization field.

5.4 Results and Discussion

Figure 5.4(a) shows the second harmonic Hall resistance, $R_{2\omega}$, with respect to the in-plane sweeping magnetic field across different ranges of current density, in a Ti/Co/Cu/BiSb/Ti heterostructure. The damping-like field, H_D, is extracted using (5.1), and the relations between H_D and current density in BiSb, J_{BiSb}, are plotted as shown in Fig. 5.2(b), where J_{BiSb} is calculated using the parallel resistor model across the Hall-cross structure. The parasitic term, $R_{\nabla T}$, is found to be negligible from the angular dependence second harmonic measurement (Refer to Section 5.3). The spin Hall angle, θ_{SH} is defined as [32–34],

$$\theta_{SH} = \frac{2eM_s t}{\hbar} \frac{H_D}{J_{BiSb}}, \tag{5.3}$$

where e is the elementary charge, M_s is the saturation magnetization of the heterostructure, t is the thickness of the ferromagnetic layer, and $\hbar$ is the reduced Planck's constant. Since the focus of this work lies in the influence of BiSb crystallinity on the SOT efficiency, I only account for the current density from the BiSb layer, J_{BiSb}. The θ_{SH} for Pt, Ti, and Cu insertion layers are 8.93, 7.11, and 8.02, respectively. On the contrary, no SOT was observed when the TI is directly adjacent to the ferromagnetic layer and sharing a common interface, as similarly

reported in other TI-FM interface studies [22,35]. This observation further verifies the theoretical prediction that the difference in the work function between the TI and FM prompt perturbations in the Dirac cone. This effect will cause a shift in the topological surface state below the Fermi energy. The hybridization of these surface states with the metal band destroys the TI's helical spin structure [36–38].

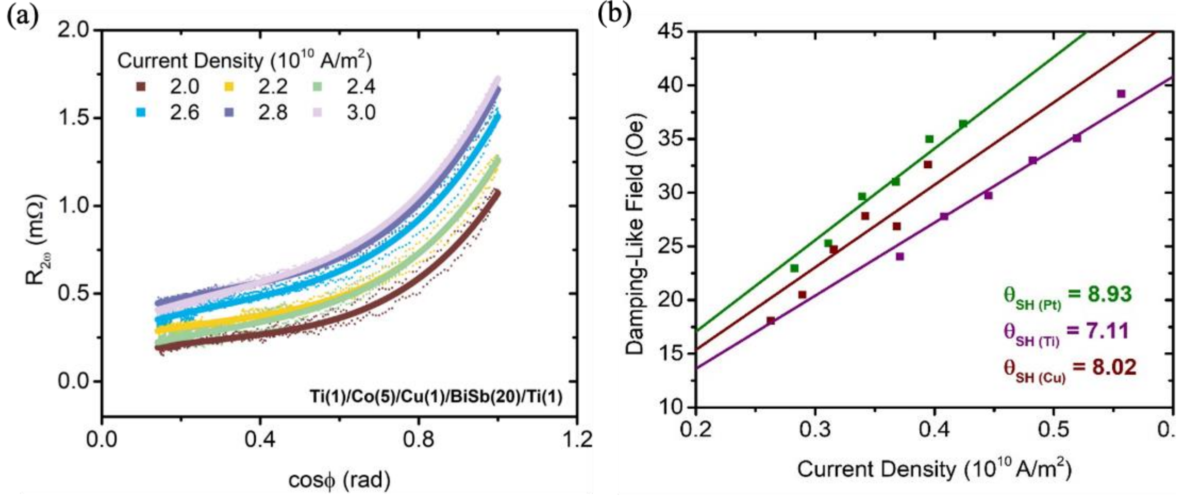

Fig. 5.4: **Damping-like term characterization by harmonic Hall technique** (a) $R_{2\omega}$ as a function of $\cos\phi$, for average current density ranging from 2 to 3×10^{10} A/m2. (b) Damping-like field as a function of current density in BiSb for different insertion layer.

The difference in magnitude of θ_{SH} for different insertion layers (Pt, Ti, Cu) can be explained by the crystallinity of BiSb(012) grown above it. Due to different crystal structures and lattice parameters of the various insertion layers, they will promote/impede the growth of BiSb(012) phase depending on the lattice mismatch between the insertion and BiSb layers. The crystal orientation is crucial, as theoretical prediction and ARPES measurements have shown that BiSb(012) has a topological surface state with three Dirac cones at the $\bar{\Gamma}, \bar{X}$, and $\bar{M}$ point [15,25,26], which is beneficial for charge-spin conversion. These Dirac cones on the TI surface are Berry flux monopoles with the same chirality, hence the numbers of Dirac cones are proportional to the total Berry flux which will lead to higher surface spin Hall conductivity [39].

Figure 5.5(a) shows the X-ray diffraction (XRD) spectra for heterostructures with various insertion layers. The XRD results reveal that at $2\theta = 27.2°$, the peak intensity of BiSb(012) is strongest with Pt insertion layer, followed by Cu insertion layer, and Ti insertion layer. Using the XRD spectra full-width half maximum (FWHM) at $2\theta = 27.2°$, the crystalline

size can be determined by using the Scherrer equation: $L = \frac{K\lambda}{\beta \cos\theta}$, where L is the crystalline size, K is the Scherrer constant, λ is the wavelength of the x-ray source, and β is the FHWM in radians. The crystalline sizes of BiSb, L, were calculated to be $L = 18.7$, 15.5, and 15.3 nm for Pt, Cu, and Ti insertion layers, respectively, as shown in Fig. 5.3(b). In addition, all the insertion layers diminished the BiSb(003) peak while improving the BiSb(012) phase. The differences in the crystalline size for different insertion layers may be due to the crystal stress and mismatch at the BiSb and insertion layer interface, as Pt, Cu, and Ti have different crystal structures and dominant phases. Although these insertion layers intermixed with the BiSb to form an amorphous layer, the short-range order of these three different intermixed layers still defers, resulting in different lattice mismatches hence affecting the crystallinity of the BiSb(012) orientation. The trend in the crystalline size for different insertion layers obtained from the XRD measurement correlates well with the SOT efficiency, further supporting the relation between the crystallinity of BiSb(012) and SOT efficiency.

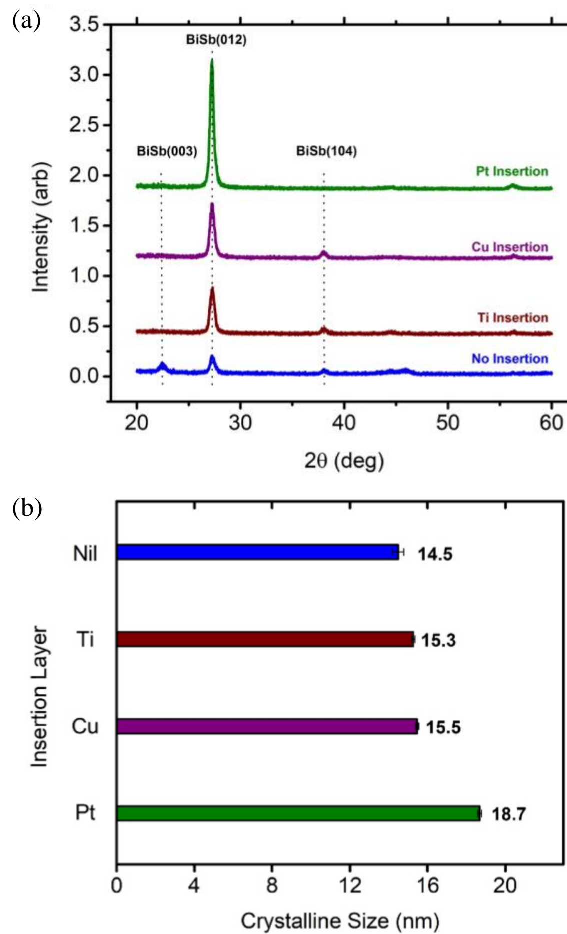

Fig. 5.5: **X-ray diffraction results and crystalline size calculations** (a) XRD $\theta - 2\theta$ spectra for BiSb heterostructure with different insertion layers grown on SiO2 substrate at $2\theta = 20 -$

60°. The peak for Si has been remove for better clarity. (b) Crystalline size calculated using Scherrer equation for different insertion layers

To have a definitive view on the crystalline structure, high-resolution transmission electron microscopy (HR-TEM) was performed on the Ti/Co/ Pt/BiSb/Ti structure. Fig. 5.6(a) shows the HR-TEM image of the Ti/Co/Pt/BiSb/Ti heterostructure, where highly crystalline BiSb is observed. Due to the ultrathin layer of Pt, intermixing occurs between the Pt insertion and BiSb layer, which can be seen between the BiSb and Co layer. The sharp interface between the intermixing of Pt insertion and BiSb, and BiSb layers similarly exhibit good crystalline texture. Using the fast-Fourier transform (FTT), I observed the corresponding electron diffraction pattern as shown in Fig. 5.6(b). The interplane spacing is determined from the distance from the centre spots, corresponding to the crystal orientation of BiSb(012). This HR-TEM image is thus in good agreement with the XRD results discussed earlier. Among the three insertion layers investigated in this work, relatively, Pt has shown to have the highest crystallinity due to its lowest surface energy of 1.48 J/m^2 , comparing to the surface energy of Cu and Ti of 1.79 J/m^2 and 4.95 J/m^2, respectively [40–44]. However, due to the only 1 nm thick Pt, it is unable to form a highly crystalline layer, and instead it intermixed with BiSb layers, as shown in Fig. 5.6(a). . Therefore, the thin Cu and Ti insertion layers would expect to intermix with BiSb layers, but form a less ordered amorphous layer compared to the Pt insertion. Although all intermixed layers (Pt/BiSB, Cu/BiSb, Ti/BiSB) are amorphous, the influence of these short-range order on BiSb(012) crystallinity differ as revealed in the XRD results. Therefore, different degrees of lattice mismatch and crystallinity of BiSb(012) orientation are obtained. . The crystalline size of the BiSb(012) is calculated to be 18.6 nm, 15.4 nm and 15.2 nm for the Pt, Cu and Ti, respectively. This order of results matches with the surface energy as described earlier. In addition, apart from better crystallinity in the BiSb(012) in Pt insertion, we can observe that the peak at the BiSb(104) ($2\theta \approx 37°$) vanished, while a small peak is observed in the Cu and Ti insertion. This further show that the degree of lattice mismatch in the intermixed BiSb/Pt and BiSb is low, thus promoting the growth of BiSb(012).

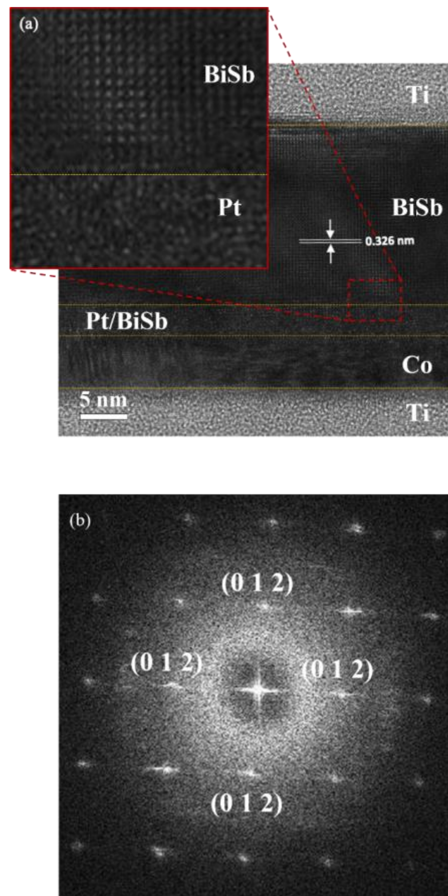

Fig. 5.6: **High-resolution transmission electron microscopy (HR-TEM) of Ti/Co/Pt/BiSb/Ti structure**. (a) Cross-sectional TEM images of Ti/Co/Pt/BiSb/Ti (b) Electronics diffraction pattern using Fast-Fourier Transform.

The crystal structure of sputter-deposited materials also improves with film thickness. As such, BiSb thickness dependence study ranging from 10 nm to 100 nm was conducted. Hall-cross devices of Ti(1 nm)/Co(5 nm)/Pt (1 nm) /BiSb(tBiSb = 10 to100 nm)/Ti(1 nm) were fabricated, and SOT efficiency was characterized using the harmonic Hall technique. The relation between θ_{SH} and BiSb thickness are shown in Fig. 5.7(a), where θ_{SH} showed a similar sharp increase with BiSb thickness and gradually saturates above BiSb = 30 nm. The corresponding XRD results show a strong BiSb(012) crystallinity with peak intensity increasing significantly with the increase in BiSb thickness, as shown in Fig. 5.7(b). The crystalline size of BiSb(012) was evaluated using the Scherrer equation and plotted in Fig. 5.7(a), a rapid increase in the crystalline size from $t_{BiSb} = 10\ nm$ to $t_{BiSb} = 50\ nm$, and gradual saturation at $t_{BiSb} > 50\ nm$ was observed. As the BiSb thickness increases, the crystal grain tends to become larger and coalesce, leading to the formation of larger grains/domains, which leads to improvement the BiSb crystallinity [45]. The alignment in the trend of

crystalline size and SOT with BiSb thickness is evident, further supporting the strong SOT being attributed to BiSb(012) crystallinity.

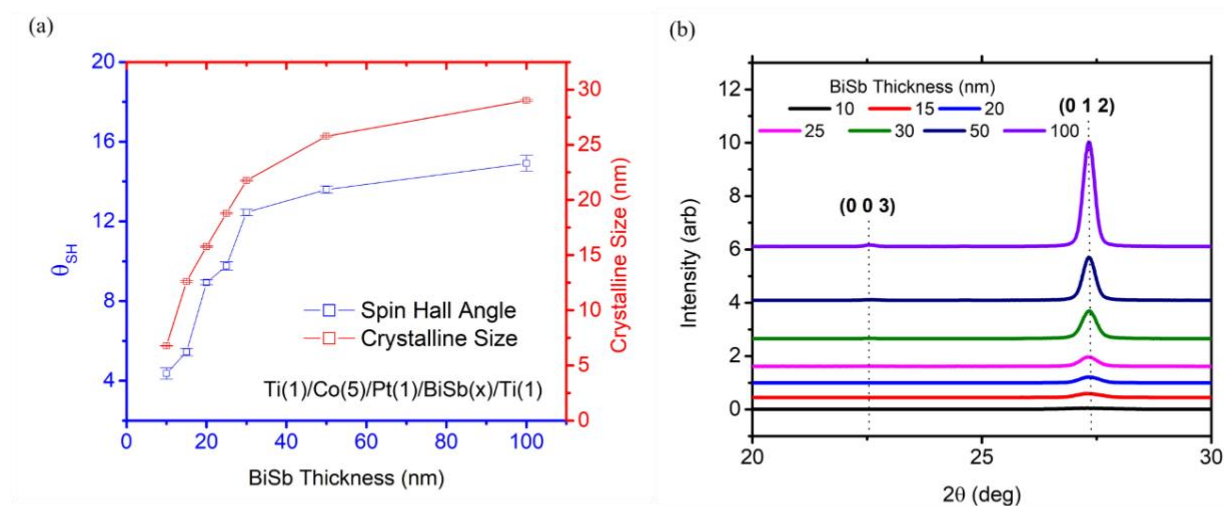

Fig. 5.7: **XRD and spin Hall angle results for varying BiSb thickness** (a) Relation of spin Hall angle and crystalline size as a function of BiSb thickness. (b) XRD $\theta - 2\theta$ spectra for BiSb heterostructure with various BiSb thickness at $2\theta = 20 - 30°$.

5.5 Conclusion

In conclusion, I showed that an insertion layer is critical for BiSb SOT generation and the SOT performance lies on the BiSb(012) crystallinity promoted by the insertion layer, with Pt being the optimal material in this study and achieving θ_SH of 8.93 compared to Cu and Ti. The crystallinity of BiSb(012) was further improved by increasing BiSb thicknesses, resulting in the increment of θ_SH up to 14.91. A clear correlation between the spin-orbit torque efficiency and the BiSb(012) crystalline size was observed, hence providing the experimental verification for the BiSb(012) crystalline orientation being the crucial contributor to spin-orbit torque generation in BiSb.

Reference

[1] H. Y. Poh, C. C. I. Ang, G. J. Lim, T. L. Jin, S. H. Lee, E. K. Koh, F. Poh, and W. S. Lew, *Crystallinity Control of the Topological-Insulator Surface Bi85Sb15 (012) via Interfacial Engineering for Enhanced Spin-Orbit Torque*, Phys. Rev. Appl. **19**, 1 (2023).

[2] X. Fan, H. Celik, J. Wu, C. Ni, K.-J. Lee, V. O. Lorenz, and J. Q. Xiao, *Quantifying Interface and Bulk Contributions to Spin–Orbit Torque in Magnetic Bilayers*, Nat. Commun. **5**, 3042 (2014).

[3] S. Woo, M. Mann, A. Tan, L. Carreta, and G. Beach, *Characterization of Spin-Orbit Torques in Pt/Co/Ta Structures*, 2015 IEEE Int. Magn. Conf. 1 (2015).

[4] S. Fukami, C. Zhang, S. DuttaGupta, A. Kurenkov, and H. Ohno, *Magnetization Switching by Spin–Orbit Torque in an Antiferromagnet–Ferromagnet Bilayer System*, Nat. Mater. **15**, 535 (2016).

[5] H. Y. Poh, C. C. I. Ang, T. L. Jin, F. N. Tan, G. J. Lim, S. Wu, F. Poh, and W. S. Lew, *Continuous Film Spin-Orbit Torque Characterization via Four Probe Measurement*, Appl. Phys. Lett. **121**, 12405 (2022).

[6] M. Akyol, B. Kıvrak, K. U. Tümen, and A. Ekicibil, *Effect of Ta Insertion between Pt and CoFeB on Interfacial Magnetic Anisotropy in Pt/CoFeB/MgO Multilayer Thin-Film Stack*, J. Mater. Sci. Mater. Electron. **31**, 23037 (2020).

[7] J. Han and L. Liu, *Topological Insulators for Efficient Spin-Orbit Torques*, APL Mater. **9**, 60901 (2021).

[8] C.-F. Pai, M. Mann, A. J. Tan, and G. S. D. Beach, *Determination of Spin Torque Efficiencies in Heterostructures with Perpendicular Magnetic Anisotropy*, Phys. Rev. B **93**, 144409 (2016).

[9] I. M. Miron, G. Gaudin, S. Auffret, B. Rodmacq, A. Schuhl, S. Pizzini, J. Vogel, and P. Gambardella, *Current-Driven Spin Torque Induced by the Rashba Effect in a Ferromagnetic Metal Layer*, Nat. Mater. **9**, 230 (2010).

[10] L. Fu, C. L. Kane, and E. J. Mele, *Topological Insulators in Three Dimensions*, Phys. Rev. Lett. **98**, 106803 (2007).

[11] H. Zhang, C. X. Liu, X. L. Qi, X. Dai, Z. Fang, and S. C. Zhang, *Topological Insulators in Bi2Se3, Bi2Te3 and Sb2Te3 with a Single Dirac Cone on the Surface*, Nat. Phys. **5**, 438 (2009).

[12] N. Roschewsky, E. S. Walker, P. Gowtham, S. Muschinske, F. Hellman, S. R. Bank, and S. Salahuddin, *Spin-Orbit Torque and Nernst Effect in Bi-Sb/Co Heterostructures*,

Phys. Rev. B **99**, 195103 (2019).

[13] J. Sasaki, H. H. Huy, N. H. D. Khang, P. N. Hai, Q. Le, B. York, X. Liu, S. Le, C. Hwang, M. Ho, and H. Takano, *Improvement of the Effective Spin Hall Angle by Inserting an Interfacial Layer in Sputtered BiSb Topological Insulator (Bottom)/Ferromagnet With In-Plane Magnetization*, IEEE Trans. Magn. **58**, 1 (2022).

[14] S. O. Valenzuela and M. Tinkham, *Direct Electronic Measurement of the Spin Hall Effect*, Nature **442**, 176 (2006).

[15] N. H. D. Khang, Y. Ueda, and P. N. Hai, *A Conductive Topological Insulator with Large Spin Hall Effect for Ultralow Power Spin–Orbit Torque Switching*, Nat. Mater. **17**, 808 (2018).

[16] M. Dc, R. Grassi, J. Y. Chen, M. Jamali, D. Reifsnyder Hickey, D. Zhang, Z. Zhao, H. Li, P. Quarterman, Y. Lv, M. Li, A. Manchon, K. A. Mkhoyan, T. Low, and J. P. Wang, *Room-Temperature High Spin–Orbit Torque Due to Quantum Confinement in Sputtered BixSe(1–x) Films*, Nat. Mater. **17**, 800 (2018).

[17] A. R. Mellnik, J. S. Lee, A. Richardella, J. L. Grab, P. J. Mintun, M. H. Fischer, A. Vaezi, A. Manchon, E. A. Kim, N. Samarth, and D. C. Ralph, *Spin-Transfer Torque Generated by a Topological Insulator*, Nature **511**, 449 (2014).

[18] J. Zhang, J. P. Velev, X. Dang, and E. Y. Tsymbal, *Band Structure and Spin Texture of Bi2Se3 3d Ferromagnetic Metal Interface*, Phys. Rev. B **94**, 014435 (2016).

[19] J. C. Rojas-Sánchez, S. Oyarzún, Y. Fu, A. Marty, C. Vergnaud, S. Gambarelli, L. Vila, M. Jamet, Y. Ohtsubo, A. Taleb-Ibrahimi, P. Le Fèvre, F. Bertran, N. Reyren, J. M. George, and A. Fert, *Spin to Charge Conversion at Room Temperature by Spin Pumping into a New Type of Topological Insulator: α -Sn Films*, Phys. Rev. Lett. **116**, 96602 (2016).

[20] P. Noel, C. Thomas, Y. Fu, L. Vila, B. Haas, P. H. Jouneau, S. Gambarelli, T. Meunier, P. Ballet, and J. P. Attané, *Highly Efficient Spin-to-Charge Current Conversion in Strained HgTe Surface States Protected by a HgCdTe Layer*, Phys. Rev. Lett. **120**, 167201 (2018).

[21] H. He, L. Tai, D. Wu, H. Wu, A. Razavi, K. Wong, Y. Liu, and K. L. Wang, *Enhancement of Spin-to-Charge Conversion Efficiency in Topological Insulators by Interface Engineering*, APL Mater. **9**, 71104 (2021).

[22] E. Longo, M. Belli, M. Alia, M. Rimoldi, R. Cecchini, M. Longo, C. Wiemer, L. Locatelli, P. Tsipas, A. Dimoulas, G. Gubbiotti, M. Fanciulli, and R. Mantovan, *Large Spin-to-Charge Conversion at Room Temperature in Extended Epitaxial Sb2Te3*

Topological Insulator Chemically Grown on Silicon, Adv. Funct. Mater. **32**, 2109361 (2022).

[23] S. Shi, A. Wang, Y. Wang, R. Ramaswamy, L. Shen, J. Moon, D. Zhu, J. Yu, S. Oh, Y. Feng, and H. Yang, *Efficient Charge-Spin Conversion and Magnetization Switching through the Rashba Effect at Topological-Insulator/Ag Interfaces*, Phys. Rev. B **97**, 41115 (2018).

[24] K. T. Yamamoto, Y. Shiomi, K. Segawa, Y. Ando, and E. Saitoh, *Universal Scaling for the Spin-Electricity Conversion on Surface States of Topological Insulators*, Phys. Rev. B **94**, 24404 (2016).

[25] J. C. Y. Teo, L. Fu, and C. L. Kane, *Surface States and Topological Invariants in Three-Dimensional Topological Insulators: Application to Bi1-x Sbx*, Phys. Rev. B **78**, 45426 (2008).

[26] X. G. Zhu, M. Stensgaard, L. Barreto, W. S. E. Silva, S. Ulstrup, M. Michiardi, M. Bianchi, M. Dendzik, and P. Hofmann, *Three Dirac Points on the (110) Surface of the Topological Insulator Bi1-XSbx*, New J. Phys. **15**, 0 (2013).

[27] H. Y. Poh, C. C. I. Ang, W. L. Gan, G. J. Lim, and W. S. Lew, *Direct Spin Accumulation Quantification in Ferromagnetic Heterostructures Using DC Bias Harmonic Hall Measurement*, Phys. Rev. B **104**, 224416 (2021).

[28] F. Luo, S. Goolaup, W. C. Law, S. Li, F. Tan, C. Engel, T. Zhou, and W. S. Lew, *Simultaneous Determination of Effective Spin-Orbit Torque Fields in Magnetic Structures with in-Plane Anisotropy*, Phys. Rev. B **95**, 174415 (2017).

[29] S. Xiao, D. Wei, and X. Jin, *Bi(111) Thin Film with Insulating Interior but Metallic Surfaces*, Phys. Rev. Lett. **109**, 1 (2012).

[30] K. Yao, N. H. D. Khang, and P. N. Hai, *Influence of Crystal Orientation and Surface Termination on the Growth of BiSb Thin Films on GaAs Substrates*, J. Cryst. Growth **511**, 99 (2019).

[31] T. Fan, M. Tobah, T. Shirokura, N. Huynh Duy Khang, N. Huynh Duy Khang, P. Nam Hai, P. Nam Hai, and P. Nam Hai, *Crystal Growth and Characterization of Topological Insulator BiSb Thin Films by Sputtering Deposition on Sapphire Substrates*, Jpn. J. Appl. Phys. **59**, 0 (2020).

[32] C. Engel, S. Goolaup, F. Luo, and W. S. Lew, *Quantitative Characterization of Spin-Orbit Torques in Pt/Co/Pt/Co/Ta/BTO Heterostructures Due to the Magnetization Azimuthal Angle Dependence*, Phys. Rev. B **96**, 054407 (2017).

[33] T. Jin, G. J. Lim, H. Y. Poh, S. Wu, F. Tan, and W. S. Lew, *Spin Reflection-Induced*

Field-Free Magnetization Switching in Perpendicularly Magnetized MgO/Pt/Co Heterostructures, ACS Appl. Mater. Interfaces **14**, 9781 (2022).

[34] T. Jin, W. C. Law, D. Kumar, F. Luo, Q. Y. Wong, G. J. Lim, X. Wang, W. S. Lew, and S. N. Piramanayagam, *Enhanced Spin–Orbit Torque Efficiency in Pt/Co/Ho Heterostructures via Inserting Ho Layer*, APL Mater. **8**, 111111 (2020).

[35] E. Longo, L. Locatelli, M. Belli, M. Alia, A. Kumar, M. Longo, M. Fanciulli, and R. Mantovan, *Spin-Charge Conversion in Fe/Au/Sb2Te3 Heterostructures as Probed By Spin Pumping Ferromagnetic Resonance*, Adv. Mater. Interfaces **8**, 2101244 (2021).

[36] J. Zhang, J. P. Velev, X. Dang, and E. Y. Tsymbal, *Band Structure and Spin Texture of ${\mathrm{Bi}}_{2}{\mathrm{Se}}_{3} 3d$ Ferromagnetic Metal Interface*, Phys. Rev. B **94**, 14435 (2016).

[37] P. B. Ndiaye, C. A. Akosa, M. H. Fischer, A. Vaezi, E. A. Kim, and A. Manchon, *Dirac Spin-Orbit Torques and Charge Pumping at the Surface of Topological Insulators*, Phys. Rev. B **96**, 014408 (2017).

[38] Y. T. Hsu, K. Park, and E. A. Kim, *Hybridization-Induced Interface States in a Topological-Insulator-Ferromagnetic-Metal Heterostructure*, Phys. Rev. B **96**, 235433 (2017).

[39] T. Shirokura, K. Yao, Y. Ueda, and P. N. Hai, *Origin of the Giant Spin Hall Effect in BiSb Topological Insulator*, ArXiv:1810.10840 2 (2018).

[40] J. S. Kim, D. Seol, and B. J. Lee, *Critical Assessment of Pt Surface Energy – An Atomistic Study*, Surf. Sci. **670**, 8 (2018).

[41] N. Itagaki, Y. Nakamura, R. Narishige, K. Takeda, K. Kamataki, K. Koga, M. Hori, and M. Shiratani, *Growth of Single Crystalline Films on Lattice-Mismatched Substrates through 3D to 2D Mode Transition*, Sci. Rep. **10**, 1 (2020).

[42] Y. Han, K. C. Lai, A. Lii-Rosales, M. C. Tringides, J. W. Evans, and P. A. Thiel, *Surface Energies, Adhesion Energies, and Exfoliation Energies Relevant to Copper-Graphene and Copper-Graphite Systems*, Surf. Sci. **685**, 48 (2019).

[43] L. Kamrani Moghaddam, S. Ramezani Paschepari, M. A. Zaimy, A. Abdalaian, and A. Jebali, *The Inhibition of Epidermal Growth Factor Receptor Signaling by Hexagonal Selenium Nanoparticles Modified by SiRNA*, Cancer Gene Ther. **23**, 321 (2016).

[44] B. Feng, J. Weng, B. C. Yang, S. X. Qu, and X. D. Zhang, *Characterization of Surface Oxide Films on Titanium and Bioactivity*, Biomaterials **24**, 4663 (2003).

[45] D. Sadek, R. Daubriac, C. Durand, R. Monflier, Q. Gravelier, A. Proietti, F. Cristiano, A. Arnoult, and S. R. Plissard, *Structural and Electrical Characterizations of BiSb*

Topological Insulator Layers Epitaxially Integrated on GaAs, Cryst. Growth Des. **22**, 5081 (2022).

Chapter 6 Influence of Magnetic Moments on the Topological Surface State in Topological Insulator/Ferromagnet Interface

In this Chapter, I will explore the influence of magnetic moments on spin-orbit torque that is generated by the topological insulator surface state in a topological insulator – ferromagnet heterostructure. I first investigate on the relation between the strength of out-of-plane magnetic moment and the SOT efficiency. I further verify these experimental results by constructing a theoretical model to simulate the surface states of $Bi_{1-x}Sb_x$ and provide theoretical evidence for the impact of perpendicular magnetic anisotropy on spin-orbit torque.

6.1 Introduction

The emergence of spin-orbit torque (SOT) has provided an efficient technique in the magnetization manipulation in spintronics devices [1–3]. Topological insulator has an insulating bulk with a two-dimensional conducting surface. The surface state has a linearly dispersion relations where it will remain gapless when the time-reversal symmetry (TRS) is preserved [4–6]. As such, TIs has gained numerous attentions in spintronics application as it has large charge-to-spin conversion due to its spin-momentum locking [7]. This magnitude of charge-to-spin conversion in TIs has reported to be several order larger than the conventional heavy metal such as Pt, Ta, and W [7–13]. However, this spin-momentum locking at the topological surface state (TSS) is prone to disturbance such as adjacent a topological insulator with a ferromagnet material. Previous theoretical studies reported that the SOT generated from the TIs vanished when it is coupled with a ferromagnet with in-plane magnetic anisotropy (IMA) [14,15]. On the contrary, other studies have shown that SOT can be generated even when it is coupled with a ferromagnet with in-plane magnetization [6]. Meanwhile, ferromagnet with perpendicular magnetic anisotropy (PMA) allows the opening of gap at the Dirac point, causing the Dirac fermions to be massive [14,15]. These discrepancies in the TI/FM interface are yet to be fully understood. Furthermore, there are many theoretical prediction on varying influences of these magnetic moments on the SOT induced by TIs, but the reported experimental verifications are very limited [14–17].

In this work, I experimentally demonstrate the influence of spin-orbit torque generated by the topological surface state when coupled with an adjacent ferromagnetic material with in-plane and perpendicular magnetic anisotropy. I also extend my work to explore the relation between the magnitude of the magnetic moment in the ferromagnetic layer, and the strength of SOT generated by the topological surface state. A constructed theoretical model was also constructed to simulate the surface states of $Bi_{1-x}Sb_x$ which provides theoretical evidence for the impact of perpendicular magnetic anisotropy on spin-orbit torque. Our results reveal that increasing the perpendicular magnetic anisotropy disrupts the surface states of $Bi_{1-x}Sb_x$ thus inducing a band gap. This widening of bandgap decreases the magnitude of SOT which validate our experimental results.

6.2 Theoretical Modelling

$Bi_{1-x}Sb_x$ is a 3D topological insulator where the surface states have a Dirac-like dispersion and are spin-momentum locked, which makes them interesting for potential applications in spintronics and quantum computing. The properties of $Bi_{1-x}Sb_x$ depend on the composition of x. For instance, as the value of x increases, the bulk band gap of the material decreases, and the Fermi level moves closer to the bulk conduction band. This results in a changed in the electronic properties of the material, such as a decrease in the surface state energy and an increase in the carrier density. Theoretical and angle-resolved photoemission spectroscopy (ARPES) experiments have revealed that $Bi_{1-x}Sb_x$, with a composition range of $0.07 \leq x \leq 0.21$, exhibits the characteristics of a three-dimensional topological insulator [18,19]. Due to its topologically protected surface states and distinctive properties, $Bi_{1-x}Sb_x$ has been extensively studied and attracted considerable research interest.

The broken inversion symmetry of $Bi_{1-x}Sb_x$ occurs at the surface, where it leads to a built-in electric field that directly couples with the spin of the relativistically moving electrons, creating the Rashba spin-orbit interaction. The resulting time-reversal invariant Dirac Hamiltonian represents the locking of spin and momentum degrees of freedom, as illustrated in Fig. 6.1(a). This locking leads to a near-linear, spin-split surface state dispersion. The Rashba spin-orbit coupling essentially creates a spin-polarized surface state with a Dirac-like energy-momentum relationship. The strong spin-momentum locking results in a significant spin-charge conversion efficiency, as well as large SOT that enable the control of adjacent magnetic layers. [7] Since $Bi_{1-x}Sb_x$ is an alloy with random substitutional disorder, its electronic

structures and dispersion relations defined within the mean field or the coherent potential approximation. The surface states are exceptionally complex, featuring as many as five or possibly more dispersion branches [20]. Considering the cricual role of Dirac-topological surface states in spin-orbit torque, our study exclusively concentrates on the theoretical model for the $Bi_{1-x}Sb_x(111)$ surface states [15]. In this study, I construct a phenomenological $k.p$ Hamiltonian by incorporating data from angle-resolved photoemission spectroscopy (ARPES) experiments on the topological surface states of $Bi_{1-x}Sb_x$ [18]. These observations can be accurately described by a Hamiltonian formulated with all terms up to the third order, ensuring its consistency with the time-reversal symmetry of the topological surface state and the crystal symmetry [18],

$$H(k) = \frac{k^2}{2m^*} + v_0(1+\alpha k^2)\left(k_x\sigma_y - k_y\sigma_x\right) + \Delta m_z\sigma_z, \quad (6.1)$$

The terms include the linear, isotropic Rashba Hamiltonian, $\mathcal{H}_D \propto v_0\,(k_x\sigma_y - k_y\sigma_x)$; $v(k) = v_0(1+\alpha k^2)$ is the correction of the Dirac velocity; $\mathcal{H}_m = k^2/2m^*$ represents a mass term, introducing particle-hole anisotropy around the Dirac point, lastly, a Zeeman effect term, $\mathcal{H}_M = \Delta m_z\sigma_z$, which comes from the perpendicular magnetic anisotropy and breaks time-reversal symmetry.

To illustrate a schematic band structure in Fig. 6.1, I have set Dirac Velocity term $v_0 =$ 1 eV and Rashba parameter $\alpha = 0.3$ eV. Due to the presence of perpendicular magnetic anisotropy, the time-reversal symmetry of the $Bi_{1-x}Sb_x$ surface is broken, leading to the opening of a gap, 2Δ, at the Dirac points of the surface states. The magnitude of this gap Δ increases linearly with the strength of the perpendicular magnetic anisotropy m_z, as shown in Fig. 6.1(c-d). The perpendicular magnetic anisotropy here is introduced by adjacent magnetic layers, and the strength of magnetism shows a linear increase with the thickness of adjacent magnetic layers, as shown in Fig. 6.1(b).

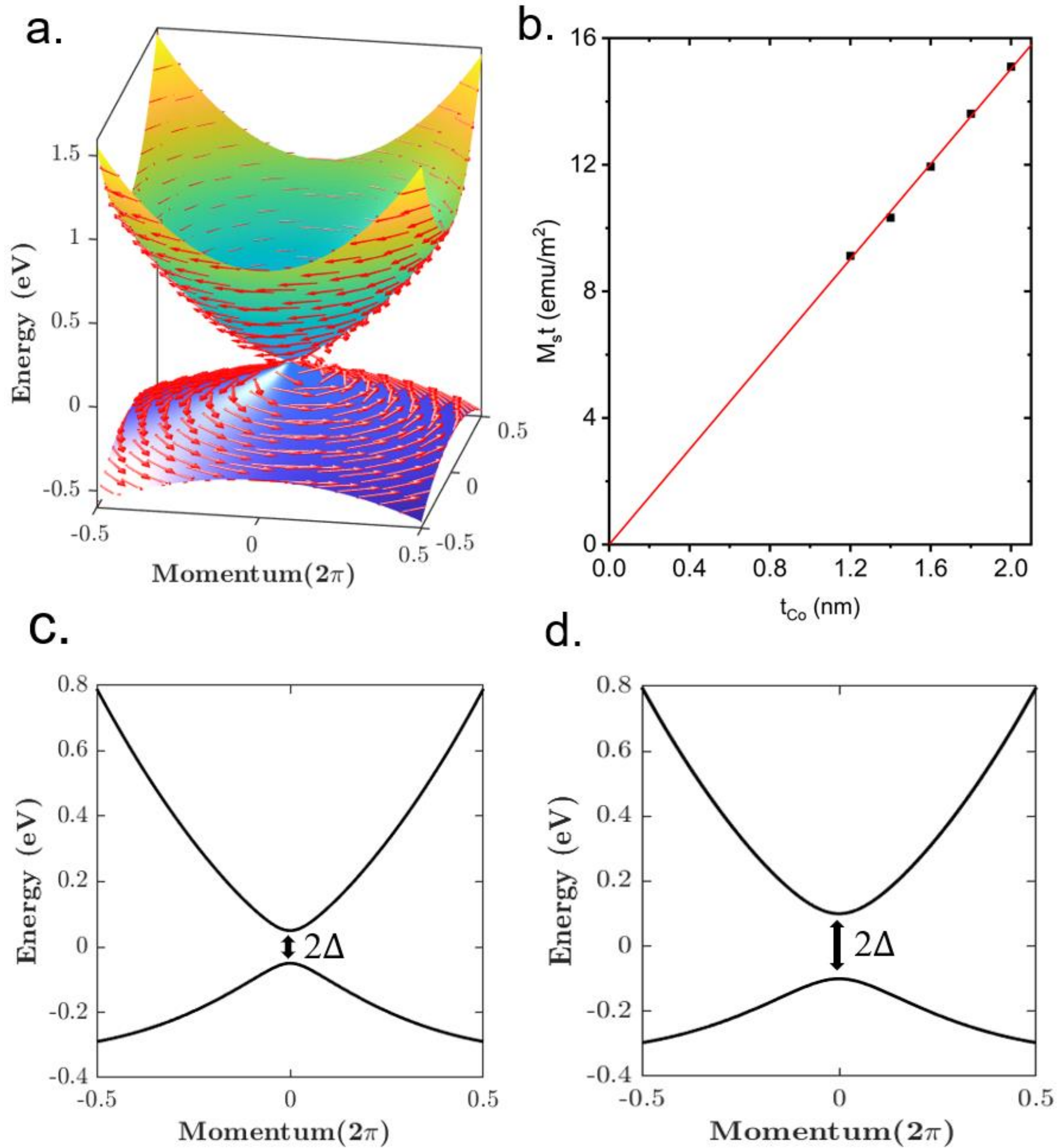

Fig. 6.1: Phenomenological band modelling of BiSb. (a), Spin texture band of BiSb (111) surface without magnetic anisotropy which present a the shape of a Dirac cone. (b), The relation between strength of magnetic anisotropy M (emu/m^2) and the thickness d (nm) of Co. (c-d) Gapped surface states of BiSb (111) under a perpendicular magnetic anisotropy, with strengths of 0.05 (c) and 0.1(d). The size of the surface-states band gap Δ increases linearly with the strength of perpendicular magnetic anisotropy.

In other words, the topological surface state band gap of $Bi_{1-x}Sb_x$ will also increase with the thickness of adjacent magnetic layers. The relationship between the topological surface state

band gap Δ opened by magnetism and damping-like Dirac spin-orbit torque has been studied based on linear-response theory [15]

$$\tau_{DL} = -\frac{2\beta^2\epsilon_F}{\hbar\bar{v}\pi}\frac{1+\beta^2 m_z^2}{(1+3\beta^2 m_z^2)^2} m_z \boldsymbol{m} \times e\boldsymbol{E}, \qquad (6.2)$$

As shown in (6.2), $\beta = \Delta/\varepsilon_F$ and ε_F is the Fermi energy of the system. From (6.2) we can directly deduce that as the thickness of the magnetic material increases, the band gap Δ of the topological surface state enlarges, and the spin-orbit torque will decrease accordingly. In the Dirac model, the flowing electrons experience only the out-of-plane magnetization, as such, the electrons precession only mixed with the S_x and S_y component. Unlike the damping-like torque which arises from spin Hall effect (SHE) in a HM, the torque shown in (6.2) is even in magnetization reversal and independent of scattering. This torque also vanishes when the magnetization lies in-plane ($m_z = 0$).

6.3 Experimental Details

The thin film stacks of Ti(1 nm)/ Pt(3)/ Co(x) / BiSb(20 nm)/ Ti(1 nm), where x = [1.2, 1.4, 1.6, 1.8, 2.0, 5.0 nm], was deposited using DC/RF magnetron sputtering, and subsequently patterned into a 5×20 µm Hall cross structure using a combination of optical lithography and ion milling techniques. The heterostructure has been characterized by vibrating sample magnetometer (VSM) as shown in Fig. 6.2(b). The VSM results revealed that the Co layer has perpendicular magnetic anisotropy (PMA) when x =1.2 – 2.0 nm, and in-plane magnetic anisotropy (IMA) at x = 5.0 nm. Second harmonics Hall technique was adopted on the Hall-cross devices to quantify the SOT efficiency. In the harmonic Hall measurement, uniform AC densities, j_{ac} ranging from 2×10^{10} A/m^2 to 3×10^{11} A/m^2 were applied in the $\hat{x}$-direction, along with longitudinal a sweeping magnetic field range from -1000 Oe to 1000 Oe. From the first harmonic voltage, V_ω and second harmonic voltage, $V_{2\omega}$, the damping-like field, H_{DL} is then be extracted using [19–22],

$$H_{DL} = -2\left(\frac{dV_{2\omega}}{dH_x}\right) / \left(\frac{d^2V_\omega}{dH_x^2}\right), \qquad (6.3)$$

The H_{DL} terms were then subsequently fitted linearly with the ranging current density to obtain the SOT efficiency. Here, the SOT efficiency was considered rather than spin Hall angle as the

focus of this work lies on the influence of the SOT strength with varying magnetic moments, and should be independent on the thickness of FM layer.

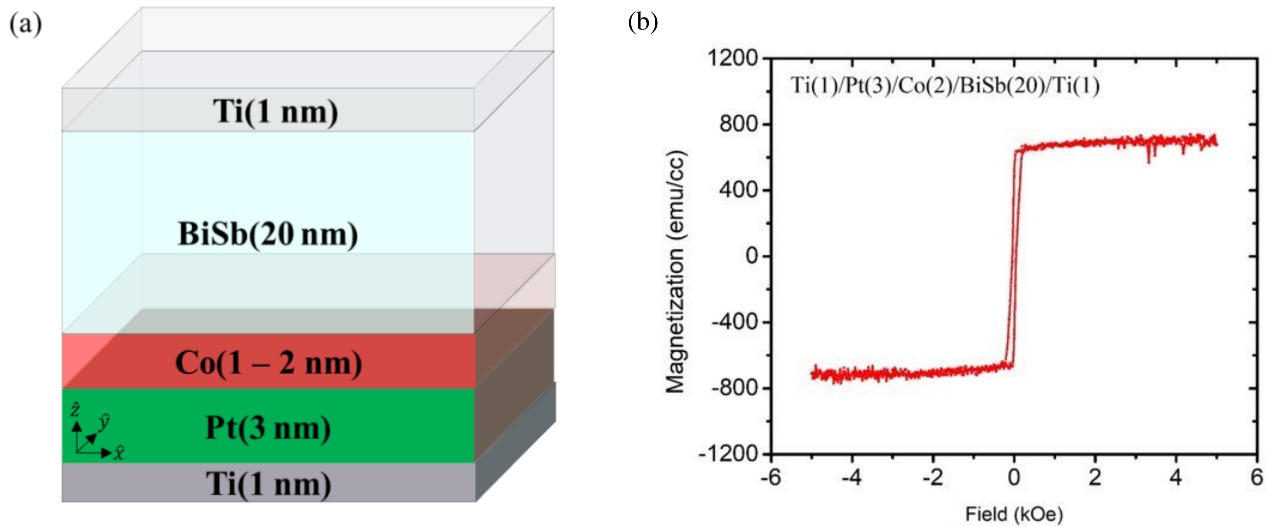

Fig. 6.2: (a) Schematic of the heterostructure with varying Co thickness (b) VSM results showing the structure with perpendicular magnetic anisotropy properties

6.4 Quantification of spin-orbit torque under varying out-of-plane magnet moment

The magnetization of the Ti(1 nm)/ Pt(3)/ Co(1.2 – 2.0 nm) / BiSb(20 nm)/ Ti(1 nm) heterostructure was obtained from VSM as shown in Fig. 6.2(b). The saturation magnetization is determined to be 760 emu/cc for all Co thicknesses, indicating that the diffusion into the BiSb from Co layers is consistent. The total magnetic moments in the Hall-cross device can be determined based on the dimensions of the device's structure by utilizing the saturation magnetization. When the TI is adjacent to these out-of-plane magnetic moments from the ferromagnet layer, it breaks both time-reversal and inversion symmetries at the TI interface. This causes a gap in the energy band at the surface of the topological insulator, and the electrons acquire a net magnetic moment due to the short-range exchange interactions [23]. As discussed in the earlier section, the damping-like torque vanished when the magnetization lies in-plane due to the shifting in the Dirac cone. Our experimental results align with the theoretical model where no SOT was obtained from the harmonic Hall measurement when the ferromagnetic layer has an in-plane magnetic anisotropy. This observation verifies the theoretical prediction that the perturbation in the Dirac cone due to the difference in work function between TI and FM will cause a shift in the topological surface state down below the Fermi energy where the

hybridization of these surface states with the metal band destroys the TI's helical spin structure [24–26]. On the other hand, high damping-like efficiency of up to H_{DL} 8.3 Oe per 10^{10} A/m^2, was observed when the ferromagnetic layer has a perpendicular magnetic anisotropy. Unlike the in-plane magnetization, the out-of-plane magnetization will cause a gap opening in the TI spectrum via $\Delta m_z \hat{\sigma}_z$, providing the mass of Dirac fermions, which was discussed in the earlier section.

I further explore the correlation between the damping-like efficiency with the strength of the magnetic moments from a thickness dependent study in the ferromagnet layer (t_{co} = 1.2 – 2.0 nm). The H_{DL} is extracted using (6.3), and the relation between the H_{DL} and current density is plotted as shown in Fig. 6.3(a). The SOT efficiency, ζ, is therefore quantified based on the gradient obtained from Fig. 6.3(a). As shown in Fig. 6.3(b), the results reveal that the SOT efficiency decreases with the increment of the ferromagnetic layer. This experimental result verifies the theoretical model discussed earlier, where the magnetization will cause the reduction in the SOT terms, the red line in Fig. 6.3(b) is qualitatively simulated using (6.2), and its trend is consistent with the experimental results. In these results, we observe that the increase in Co thickness enhances the out-of-plane magnetic moment, leading to a larger Δ, and consequently, a wider energy gap in the topological insulator spectrum. This increase in the energy gap elevates the parameter β, which is inversely proportional to the SOT efficiency as shown in (6.2). Hence, a decrease in SOT efficiency with increasing Co thickness is expected and observed, aligning the experimental results with the simulation, as illustrated in Fig. 6.3(b). This correlation underscores a qualitative agreement between the theoretical predictions and the experimental results.

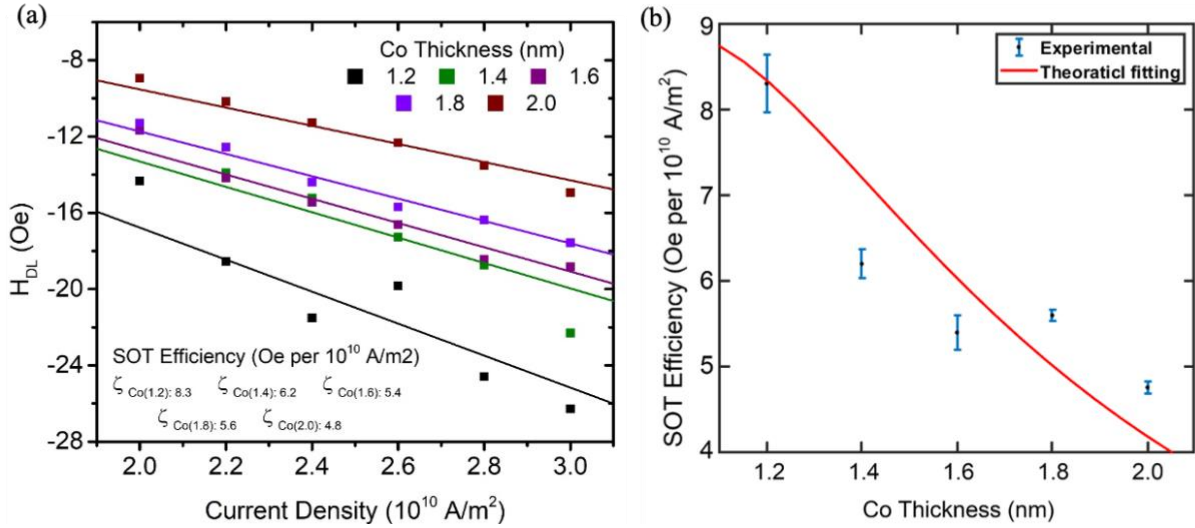

Fig. 6.3: **Damping-like term characterization by harmonic Hall technique** (a) Damping-like field as a function of average current density ranging from 2 to 3 $\times$ 10^{10} A/m^2. (b) Relation of SOT efficiency as a function of Co thickness.

The high SOT efficiency obtained in our work can be explained by the crystallinity of the BiSb(012) crystal orientation. Studies have shown that BiSb(012) topological surface state yields high SOT due to having three Dirac cones at the $\bar{\Gamma}, \bar{\mathrm{X}}$, and $\bar{M}$ points [7,27–29]. Figure 6.4(a) illustrates the X-ray diffraction (XRD) spectra for Ti(1 nm)/ Pt(3)/ Co(2.0 nm) / BiSb(20 nm)/ Ti(1 nm). This XRD result reveals that indeed, BiSb(012) is the dominating phase ($2\theta = 27.2°$), which is crucial for achieving high SOT efficiency.

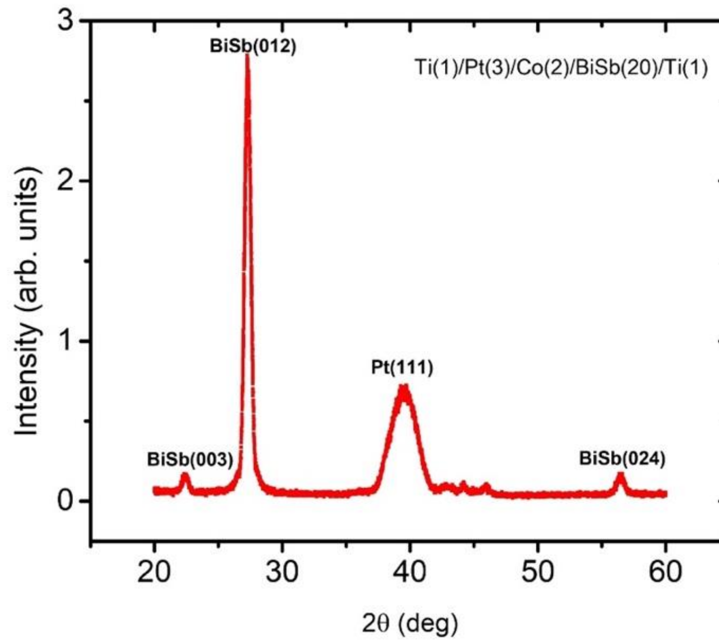

Fig. 6.4: XRD θ-2θ spectra for Ti/Pt/Co/BiSb/Ti structure where BiSb(012) is the dominating phase.

6.5 Conclusion

In conclusion, I show that in Pt(3)/Co(1.2 – 2)/BiSb(20)/Ti(2) structure, the adjacent magnetization from the Co ferromagnetic layer influences the SOT efficiency which is generated from the BiSb topological insulator layer. By increasing the magnetic moments in the ferromagnetic layer, a decreasing relation in SOT efficiency was observed. A *k-p* model was constructed to simulate the surface states of the $Bi_{1-x}Sb_x$, which show that the ferromagnetic layer opens the band gap of the topological surface states in the $Bi_{1-x}Sb_x$. The increase in magnetization from having more ferromagnetic layer results in a larger band gap in the topological surface states of the $Bi_{1-x}Sb_x$. This increment in the band gap decreases the SOT efficiency, hence the outcome modelling confirms our experimental results.

Reference

[1] A. Manchon and S. Zhang, *Theory of Spin Torque Due to Spin-Orbit Coupling*, Phys. Rev. B **79**, 94422 (2009).

[2] C. Song, R. Zhang, L. Liao, Y. Zhou, X. Zhou, R. Chen, Y. You, X. Chen, and F. Pan, *Spin-Orbit Torques: Materials, Mechanisms, Performances, and Potential Applications*, Prog. Mater. Sci. **118**, 100761 (2021).

[3] H. Wu, S. A. Razavi, Q. Shao, X. Li, K. L. Wong, Y. Liu, G. Yin, and K. L. Wang, *Spin-Orbit Torque from a Ferromagnetic Metal*, Phys. Rev. B **99**, 1 (2019).

[4] J. Liu and T. Hesjedal, *Magnetic Topological Insulator Heterostructures: A Review*, Adv. Mater. **2102427**, (2021).

[5] H. Lohani, P. Mishra, A. Banerjee, K. Majhi, R. Ganesan, U. Manju, D. Topwal, P. S. Anil Kumar, and B. R. Sekhar, *Band Structure of Topological Insulator BiSbTe1.25Se1.75*, Sci. Rep. **7**, 1 (2017).

[6] J. Y. Li, R. Q. Wang, M. X. Deng, and M. Yang, *In-Plane Magnetization Effect on Current-Induced Spin-Orbit Torque in a Ferromagnet/Topological Insulator Bilayer with Hexagonal Warping*, Phys. Rev. B **99**, 1 (2019).

[7] N. H. D. Khang, Y. Ueda, and P. N. Hai, *A Conductive Topological Insulator with Large Spin Hall Effect for Ultralow Power Spin–Orbit Torque Switching*, Nat. Mater. **17**, 808 (2018).

[8] L. Fu, C. L. Kane, and E. J. Mele, *Topological Insulators in Three Dimensions*, Phys. Rev. Lett. **98**, 106803 (2007).

[9] P. Noel, C. Thomas, Y. Fu, L. Vila, B. Haas, P.-H. Jouneau, S. Gambarelli, T. Meunier, P. Ballet, and J. P. Attané, *Highly Efficient Spin-to-Charge Current Conversion in Strained HgTe Surface States Protected by a HgCdTe Layer*, Phys. Rev. Lett. **120**, 167201 (2018).

[10] J. Han and L. Liu, *Topological Insulators for Efficient Spin–Orbit Torques*, APL Mater. **9**, 60901 (2021).

[11] H. Y. Poh, C. C. I. Ang, T. L. Jin, F. N. Tan, G. J. Lim, S. Wu, F. Poh, and W. S. Lew, *Continuous Film Spin–Orbit Torque Characterization via Four Probe Measurement*, Appl. Phys. Lett. **121**, 12405 (2022).

[12] Q. Lu, P. Li, Z. Guo, G. Dong, B. Peng, X. Zha, T. Min, Z. Zhou, and M. Liu, *Giant Tunable Spin Hall Angle in Sputtered Bi2Se3 Controlled by an Electric Field*, Nat. Commun. **13**, 1 (2022).

[13] J. Ding, C. Liu, Y. Zhang, V. Kalappattil, R. Yu, U. Erugu, J. Tang, H. Ding, H. Chen, and M. Wu, *Large Damping Enhancement in Dirac-Semimetal–Ferromagnetic-Metal Layered Structures Caused by Topological Surface States*, Adv. Funct. Mater. **31**, 1 (2021).

[14] Y. T. Hsu, K. Park, and E. A. Kim, *Hybridization-Induced Interface States in a Topological-Insulator-Ferromagnetic-Metal Heterostructure*, Phys. Rev. B **96**, 235433 (2017).

[15] P. B. Ndiaye, C. A. Akosa, M. H. Fischer, A. Vaezi, E. A. Kim, and A. Manchon, *Dirac Spin-Orbit Torques and Charge Pumping at the Surface of Topological Insulators*, Phys. Rev. B **96**, 014408 (2017).

[16] Q. Liu, C. X. Liu, C. Xu, X. L. Qi, and S. C. Zhang, *Magnetic Impurities on the Surface of a Topological Insulator*, Phys. Rev. Lett. **102**, 1 (2009).

[17] A. Kosma, P. Rüßmann, S. Blügel, and P. Mavropoulos, *Strong Spin-Orbit Torque Effect on Magnetic Defects Due to Topological Surface State Electrons in ${\mathrm{Bi}}_{2}{\mathrm{Te}}_{3}$*, Phys. Rev. B **102**, 144424 (2020).

[18] L. Fu, *Hexagonal Warping Effects in the Surface States of the Topological Insulator ${\mathrm{Bi}}_{2}{\mathrm{Te}}_{3}$*, Phys. Rev. Lett. **103**, 266801 (2009).

[19] M. Hayashi, J. Kim, M. Yamanouchi, and H. Ohno, *Quantitative Characterization of the Spin-Orbit Torque Using Harmonic Hall Voltage Measurements*, Phys. Rev. B - Condens. Matter Mater. Phys. **89**, 144425 (2014).

[20] T. Jin, G. J. Lim, H. Y. Poh, S. Wu, F. Tan, and W. S. Lew, *Spin Reflection-Induced Field-Free Magnetization Switching in Perpendicularly Magnetized MgO/Pt/Co Heterostructures*, ACS Appl. Mater. Interfaces **14**, 9781 (2022).

[21] H. Yang, H. Chen, M. Tang, S. Hu, and X. Qiu, *Characterization of Spin-Orbit Torque and Thermoelectric Effects via Coherent Magnetization Rotation*, Phys. Rev. B **102**, 24427 (2020).

[22] L. Neumann and M. Meinert, *Influence of the Hall-Bar Geometry on Harmonic Hall Voltage Measurements of Spin-Orbit Torques*, AIP Adv. **8**, 95320 (2018).

[23] Y. Okuyama, R. Ishikawa, S. Kuroda, and T. Hirahara, *Role of Hybridization and Magnetic Effects in Massive Dirac Cones: Magnetic Topological Heterostructures with Controlled Film Thickness*, Appl. Phys. Lett. **114**, (2019).

[24] J. C. Rojas-Sánchez, S. Oyarzún, Y. Fu, A. Marty, C. Vergnaud, S. Gambarelli, L. Vila, M. Jamet, Y. Ohtsubo, A. Taleb-Ibrahimi, P. Le Fèvre, F. Bertran, N. Reyren, J. M. George, and A. Fert, *Spin to Charge Conversion at Room Temperature by Spin Pumping*

into a New Type of Topological Insulator: α -Sn Films, Phys. Rev. Lett. **116**, 96602 (2016).

[25] J. Zhang, J. P. Velev, X. Dang, and E. Y. Tsymbal, *Band Structure and Spin Texture of ${\mathrm{Bi}}_{2}{\mathrm{Se}}_{3} 3d$ Ferromagnetic Metal Interface*, Phys. Rev. B **94**, 14435 (2016).

[26] P. Noel, C. Thomas, Y. Fu, L. Vila, B. Haas, P. H. Jouneau, S. Gambarelli, T. Meunier, P. Ballet, and J. P. Attané, *Highly Efficient Spin-to-Charge Current Conversion in Strained HgTe Surface States Protected by a HgCdTe Layer*, Phys. Rev. Lett. **120**, 167201 (2018).

[27] H. Y. Poh, C. C. I. Ang, G. J. Lim, T. L. Jin, S. H. Lee, E. K. Koh, F. Poh, and W. S. Lew, *Crystallinity Control of the Topological-Insulator Surface Bi85Sb15 (012) via Interfacial Engineering for Enhanced Spin-Orbit Torque*, Phys. Rev. Appl. **19**, 1 (2023).

[28] J. C. Y. Teo, L. Fu, and C. L. Kane, *Surface States and Topological Invariants in Three-Dimensional Topological Insulators: Application to* $Bi_{1-x}Sb_x$, Phys. Rev. B **78**, 45426 (2008).

[29] X. G. Zhu, M. Stensgaard, L. Barreto, W. S. E. Silva, S. Ulstrup, M. Michiardi, M. Bianchi, M. Dendzik, and P. Hofmann, *Three Dirac Points on the (110) Surface of the Topological Insulator Bi1-XSbx*, New J. Phys. **15**, (2013).

Chapter 7

Conclusion and Future Work

7.1 Summary of thesis

This thesis presented four main works in the field of spin-orbit torque (SOT): (i) Direct quantification of SOT without any lithography process, covered in Chapter 3. (ii) Quantification of spin accumulation, covered in Chapter 4. (iii) Crystallinity control of topological insulator for SOT enhancement, covered in Chapter 5. (iv) The influence of out-of-plane magnetic moments on spin-orbit torque generated by topological surface state is covered in Chapter 6.

In Chapter 3, I have shown a measurement technique using a four-probe to directly determine the SOT of the heterostructure without lithography processes which costs additional resources and time. The H_{DL} of the continuous films were successfully characterized using the harmonic Hall technique by accounting for the divergent current distribution using a constant scaling factor. This correction factor of 62 is experimentally quantified by taking the ratio of the H_{DL} between continuous films and Hall devices. The proposed technique is a cost-effective characterization of SOT efficiency, which is akin to the current in-plane technique that is currently widely used in the industry for obtaining tunneling magnetoresistance from thin-film stacks without any lithography steps.

In Chapter 4, current-induced spin accumulation in Si/SiO2/Ta/Co/Pt and Si/SiO2/Ti/Co/Pt structures have been quantified using the harmonic Hall measurement technique with DC bias. Our experiments show that the spin accumulation is approximately 0.29% per kV/m of the local magnetization for 10 nm Ta. Our results demonstrate that, besides the conventional SOT measurement, spin accumulation can also be quantified using the harmonic Hall technique. The ratio of the spin accumulation over the applied electric field shows a similar trend with damping-like efficiency as the thickness of HM increases. Hence, the ratio can be used to evaluate the efficiency of an HM in converting electric current to spin current. This provides an all-electrical alternative to determine spin accumulation by utilizing the easily accessible harmonic Hall characterization technique.

In Chapter 5, I showed that an insertion layer is critical for BiSb SOT generation, and the SOT performance lies on the BiSb(012) crystallinity promoted by the insertion layer, with Pt being the optimal material in this study and achieving θ_{SH} of 8.93 compared to Cu and Ti. The crystallinity of BiSb(012) was further improved by increasing BiSb thicknesses, resulting in the increment of θ_{SH} up to 14.91. A clear correlation between the spin-orbit torque efficiency and the BiSb(012) crystalline size was observed, hence providing the experimental verification for the BiSb(012) crystalline orientation being the crucial contributor to spin-orbit torque generation in BiSb.

In Chapter 7, I experimentally demonstrate the influence of spin-orbit torque generated from the topological surface state under varying out-of-plane magnetic moments. Our results reveal that the strength of spin-orbit torque decreases with the increment of out-of-plane magnetic moments. I further verify these experimental results by constructing a theoretical model to simulate the surface states of Bi1-xSbx and provide theoretical evidence for the impact of perpendicular magnetic anisotropy on spin-orbit torque. This model shows that the magnetic moment will induce a band gap, hence, decreasing the strength of the spin-orbit torque, validating our experimental results. Our work provides insights in the correlation between the magnetic moment and spin-orbit torque generated by the topological insulator, which are beneficial for spintronics applications.

7.2 Future Work

In this section, two future works that extend from the work presented in this thesis are proposed. These proposed works involve the enhancement of spin-orbit torque using topological insulator-based materials, which are crucial for spintronics applications.

7.2.1 Fermi Level Tuning in Topological Insulator with Voltage Control Magnetic Anisotropy Heterostructure

In Chapter 6, I discussed the influence of magnetic moment on spin-orbit torque generated by the topological insulator. One proposed future work involves the manipulation of spin-orbit torque by applying gate voltage. The introduction of voltage results in a shift in Fermi level, thereby modulating the spin-orbit torque [1,2]. Ki Hyuk Han, *et. al*, has shown that the gate electric field modulates the position of the Fermi level in sputtered Bi_2Se_3. The strength of damping-like torque has noticeably changed by the gate voltage. Meanwhile,

numerous studies have shown the assisted voltage control magnetic anisotropy (VCMA) SOT magnetization switching [3–6]. When an electric field is applied to a ferromagnetic material, it changes the distribution of electron charge density. This perturbation affects the spin-orbit interaction between the spin magnetic moment of an electron and its orbital motion, which results in the assisting of SOT magnetization switching.

Here, I propose a hybrid structure that integrates topological insulators with VCMA heterostructures. In this configuration, the injection of a gate voltage serves multiple purposes. Firstly, it allows the tuning of the Fermi level in the topological insulator, facilitating optimal control over its conductive properties. Concurrently, it alters the magnetic anisotropy of the interfaced ferromagnetic layer, a factor crucial in controlling the magnetization dynamics. The combination of these effects could notably enhance the efficiency of SOT switching, thus presenting promising avenues for developing next-generation spintronic.

7.2.2 Magnetic Topological Insulator

In Chapter 5, I examined the role of controlling crystallinity in enhancing spin-orbit torque (SOT) in topological insulator (TIs) materials. In the pursuit of further enhancing the characteristics of topological insulators, I propose inducing magnetic order within these materials to yield magnetic topological insulators (MTIs). The magnetic ordering of topological materials has been shown to unlock the potential of topological phases with enhanced robustness to topological properties [7–10]. Specifically, incorporating this magnetic ordering into topological insulators (TIs) can lead to the development of a quantum anomalous Hall insulator that exhibits chiral 1D edges, which are protected by the inverted bandgap, making them highly robust to backscattering.

This proposed work aims to investigate the potential use of MTI in generating large spin-orbit torques, a crucial factor in energy-efficient and ultrafast spin-based computing and communication technologies. There are two potential methods for fabricating MTI structures: (i) using magnetically doped TIs, and (ii) utilizing the interface between a magnetic material (MM) and a TI. In the former method, a 3d-transition metal ion is doped into the topological insulator crystal, such as BiSb-Mn and BiSb-Fe, resulting in the long-range magnetic ordering through mechanisms such as the Ruderman-Kittel-Kasuya-Yosida (RKKY) interaction. The latter method involves engineering a heterostructure of a TI and an MM (ferromagnet metal,

ferromagnet insulator, antiferromagnet, ferrimagnetic) to induce a magnetic proximity effect in the TIs. Examples of such heterostructures include BiSb(Te)/in-plane or out-of-plane ferromagnetic layer, BiSb(Te)/antiferromagnetic layer, and BiSb(Te)/canted antiferromagnetic. The proposed MTI heterostructures will undergo optimization to improve their magnetic properties and gain a deeper understanding of their behavior. This optimization will involve analytical and numerical calculations, such as density functional theory calculations of the electronic band structure, wavefunction analysis, and Berry curvature mapping. These calculations will not only aid in optimizing the fabrication of MTI heterostructures but will also help verify existing or proposed models and deepen our understanding of magnetization dynamics, QAHE, and spin-orbit torque based on experimental results.

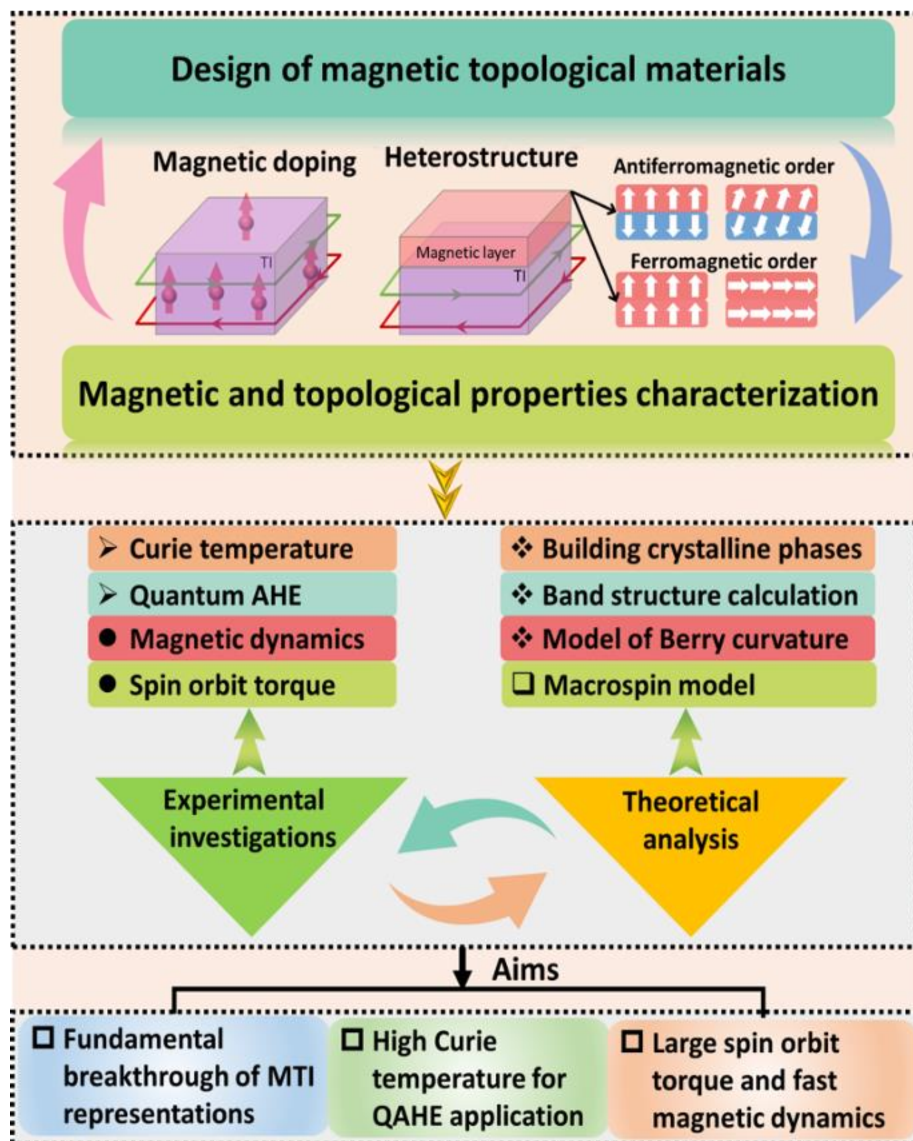

Fig. 7.1: Overview of the proposed work

Reference

[1] K. H. Han, Y. H. Park, J. U. Ahn, S. B. Kim, K.-W. Kim, T.-E. Park, O. Lee, B.-C. Min, and H. C. Koo, *Gate Control of Spin–Orbit Torque in a Sputtered Bi2Se3/Ni81Fe19 Device*, ACS Appl. Electron. Mater. **5**, 2725 (2023).

[2] E. Uesugi, T. Uchiyama, H. Goto, H. Ota, T. Ueno, H. Fujiwara, K. Terashima, T. Yokoya, F. Matsui, J. Akimitsu, K. Kobayashi, and Y. Kubozono, *Fermi Level Tuning of Ag-Doped Bi2Se3 Topological Insulator*, Sci. Rep. **9**, 5376 (2019).

[3] H. Wu, J. Zhang, B. Cui, S. A. Razavi, X. Che, Q. Pan, D. Wu, G. Yu, X. Han, and K. L. Wang, *Field-Free Approaches for Deterministic Spin–Orbit Torque Switching of the Perpendicular Magnet*, Mater. Futur. **1**, 22201 (2022).

[4] S. Li and Y. Jiang, *Field-Free Switching Model of Spin–Orbit Torque (SOT)-MTJ Device with Thermal Effect Based on Voltage-Controlled Magnetic Anisotropy (VCMA)*, AIP Adv. **13**, 25030 (2023).

[5] S. Alla, V. K. Joshi, and S. Bhat, *Voltage-Gated Spin-Orbit Torque Magnetic Tunnel Junction Model Analysis*, in *2022 International Conference on Distributed Computing, VLSI, Electrical Circuits and Robotics (DISCOVER)* (2022), pp. 96–101.

[6] W. Li, S. Peng, J. Lu, H. Wu, X. Li, D. Xiong, Y. Zhang, Y. Zhang, K. L. Wang, and W. Zhao, *Experimental Demonstration of Voltage-Gated Spin-Orbit Torque Switching in an Antiferromagnet/Ferromagnet Structure*, Phys. Rev. B **103**, 94436 (2021).

[7] N. J. Steinke, S. L. Zhang, P. J. Baker, L. B. Duffy, F. Kronast, J. Krieger, Z. Salman, T. Prokscha, A. Suter, S. Langridge, G. Van Der Laan, and T. Hesjedal, *Magnetic Correlations in the Magnetic Topological Insulator (Cr,Sb)2Te3*, Phys. Rev. B **106**, 1 (2022).

[8] P. Wang, J. Ge, J. Li, Y. Liu, Y. Xu, and J. Wang, *Intrinsic Magnetic Topological Insulators*, Innov. **2**, 100098 (2021).

[9] Q. Liu, C. X. Liu, C. Xu, X. L. Qi, and S. C. Zhang, *Magnetic Impurities on the Surface of a Topological Insulator*, Phys. Rev. Lett. **102**, 1 (2009).

[10] Y. Fan, P. Upadhyaya, X. Kou, M. Lang, S. Takei, Z. Wang, J. Tang, L. He, L. Te Chang, M. Montazeri, G. Yu, W. Jiang, T. Nie, R. N. Schwartz, Y. Tserkovnyak, and K. L. Wang, *Magnetization Switching through Giant Spin-Orbit Torque in a Magnetically Doped Topological Insulator Heterostructure*, Nat. Mater. **13**, 699 (2014).

List of Publication

1. **Han Yin Poh**, Calvin Ching Ian Ang, Gerard Joseph Lim, Tianli Jin, Shu Hui Lee, Eng Kang Koh, Francis Poh, and Wen Sang Lew. Crystallinity control of topological insulator BiSb(012) via interfacial engineering for spin orbit torque enhancement, Physical Review Applied, 19, 034012 (2023); doi.org/10.1103/PhysRevApplied.19.034012

2. **Han Yin Poh**, Calvin Ching Ian Ang, Tianli Jin, Funan Tan, Gerard Joseph Lim, and Wen Siang Lew. Continuous film characterisation of Spin Orbit Torque using Four Probe Measurement, Applied Physics Letters, 121, 012405 (2022); doi.org/10.1063/5.0092471

3. **Han Yin Poh**, Calvin Ching Ian Ang, Wei Liang. Gan, Gerard Joseph Lim, and Wen Siang Lew. Direct spin accumulation quantification in ferromagnetic heterostructures using DC bias harmonic Hall measurement, Physical Review B, 104, 224416 (2021); doi.org/10.1103/PhysRevB.00.004400

4. **Han Yin Poh**, Tao Hou, Wei Jie Chan, Yee Sin Ang, Wen Siang Lew. Influence of magnetic moments on the topological surface state in topological Insulator/ferromagnet interface. Submitted

5. Birte Coester, Gerard Lim, Funan Tan, **Han Yin Poh**, and Wen Siang Lew. Investigation of spin-orbit torque performance with W/Cu-multilayers as spin current source, Journal of Applied Physics, 133, 223904 (2023); doi.org/10.1063/5.0139212

6. Shou Wu, Tianli Jin, Funan Tan, Calvin Ching Ian Ang, **Han Yin Poh**, Gerard Joseph Lim, and Wen Siang Lew. Enhancement of spin-orbit torque in Pt/Co/HfOx heterostructures with voltage-controlled oxygen ion migration; Applied Physics Letters, 122, 122403(2023);doi.org/10.1063/5.0139443

7. Tianli Jin, Gerard Joseph Lim, **Han Yin Poh**, Shuo Wu, Funan Tan, and Wen Siang Lew. Spin reflection induced field-free magnetization switching in perpendicularly magnetized MgO/Pt/Co heterostructures, ACS Applied Materials & Interfaces, 14, 7, 9781 (2022) ; 10.1021/acsami.1c22061

8. Calvin Lee, Putu Andhita Dananjaya, Mun Yin Chee, **Han Yin Poh**, Funan Tan, Jia Rui Thong, Lingli Liu, Gerard Joseph Lim, Yuanmin Du, Juan Boon Tan, Wen Siang Lew. **Influence of Co-Cu Electrode Composition on the Galvanic-induced Resistive Switching Behaviour of Ta_2O_5-based CBRAM**, Applied Physics Letters. Revision

9. Eng Kang Koh, Putu Andhita Dananjaya, **Han Yin Poh**, Lingli Liu, Calvin Xiu Xian Lee, Jia Rui Thong, and Wen Siang Lew. **Abrupt and gradual switching response in a single 1T-1R Ta_2O_5-based resistive memory device for storage-class memory and synaptic tuning applications.** Submitted

10. Lingli Liu, Putu Andhita Dananjaya, Calvin Ching Ian Ang, Eng Kang Koh, Gerard Joseph Lim, **Han Yin Poh**, Mun Yin Chee*,* Calvin Xiu Xian Lee, Wen Siang Lew. **Bi-functional Three-Terminal Memristor Applicable as Artificial Synapse and Neurons**. Submitted.

List of Conference

1. **Han Yin Poh**, Calvin Ching Ian Ang, Gerard Joseph Lim, Wen Sang Lew. Topological Insulator Spin Orbit-torque Enhancement Via Insertion Layer and Crystallinity Control of Bisb(012). *International Conference on Materials for Advanced Technologies 2023, Singapore*

2. **Han Yin Poh**, Wei Siang Lew. **Influence of magnetic moments on spin-orbit torque efficiency from topological surface state in TI/FM interface**, *INTERMAG 2023, Sendai, Japan*

3. **Han Yin Poh**, *Calvin Ching Ian Ang,* Gerard Joseph Lim, Wen Sang Lew. **Quantification of Spin Accumulation in Ferromagnetic Heterostructure using DC Bias Harmonic.** *INTERMAG 2023, Sendai, Japan*

4. **Han Yin Poh**, Tianli Jin, Wen Sang Lew. Tuning Spin-Orbit Torque Generation Via Seed/Heavy Metal Interface Modification. *INTERMAG 2023, Sendai, Japan*

5. **Han Yin Poh**, Calvin Ching Ian Ang**, Shu Hui Lee,** Gerard Joseph Lim, Tianli Jin, Wen Siang Lew. **BiSb(012) Crystallinity and Strong Spin Orbit-Torque Enhancement Using Insertion Layer**. *2022 MRS Fall Meeting & Exhibit, Boston, Massachusetts, USA*

6. **Han Yin Poh**, *Calvin Ching Ian Ang,* **Shu Hui Lee,** Gerard Joseph Lim, Tianli Jin, Wen Siang Lew. Topological Insulator Spin Orbit-Torque Enhancement via Insertion Layer and Crystallinity Control of BiSb(012). *2022 Annual Conference on Magnetism and Magnetic Materials (MMM 2022), Minneapolis, USA.*

7. **Han Yin Poh**, *Calvin Ching Ian Ang, Wei Liang Gan, Gerard Joseph Lim, Wen Siang Lew. Quantification of Spin Accumulation Magnetoresistance in Ferromagnetic heterostructure using DC Bias Harmonic Hall Measurement. Joint European Magnetic Symposia (JEMS 2022), Warsaw, Poland.*

8. **Han Yin Poh**, *Calvin Ching Ian Ang, Wei Liang Gan, Gerard Joseph Lim, Wen Siang Lew. Quantification of spin accumulation magnetoresistance using DC bias harmonic Hall measurement. IEEE Magnetics Symposium 2021, IEEE Magnetics Society, Singapore.*

9. Jia Rui Thong, Yu Min Du, Eng Kang Koh, Xiu Xian Lee, **Han Yin Poh**, Wei Siang Lew. Enhancement of Resistive Switching In HfO_2-Based Devices Through Oxygen Plasma Treatment. *International Conference on Materials for Advanced Technologies 2023, Singapore*

10. Tianli Jin, Funan Tan, Shu Hui Lee, **Han Yin Poh**, Shuo Wu, Gerard Joseph Lim, Wen Siang. All-electrical Manipulation of Multiple Magnetization States via Modifying Magnetic Anisotropy for Emulating Synaptic Devices. *2022 Annual Conference on Magnetism and Magnetic Materials (MMM 2022), Minneapolis, USA.*

11. Calvin Lee, Putu Andhita Dananjaya, Mun Yin Chee, **Han Yin Poh**, Funan Tan, Jia Rui Thong, Lingli Liu, Gerard Joseph Lim, Yuanmin Du, Wen Siang Lew. Resistive Switching Improvement of TaOx-based CBRAM with Co-Cu alloy electrode. *2nd International Conference on Materials for Humanity (MH 2022), Singapore*

12. Shuo Wu, Tianli Jin, Funan Tan, Calvin Ching Ian Ang, **Han Yin Poh**, Gerard Joseph Lim, Wen Siang Lew. Enhancement of spin-orbit torque in Pt/Co/HfOx heterostructures with voltage-controlled oxygen ion migration. *2nd International Conference on Materials for Humanity (MH 2022), Singapore*

13. Tianli Jin, Gerard Joseph Lim, **Han Yin Poh**, Shou Wu, Funan Tan, Wen Siang Lew. Spin reflection induced field-free magnetization switching in perpendicularly magnetized MgO/Pt/Co heterostructures. *IEEE Magnetics Symposium 2021, IEEE Magnetics Society, Singapore.*